N° d'ordre: 4321

THÈSE

Présentée à

L'UNIVERSITÉ DE BORDEAUX I

ÉCOLE DOCTORALE DES SCIENCES PHYSIQUES ET DE L'INGÉNIEUR

Par **Riad YAHIAOUI**

Pour obtenir le grade de

DOCTEUR

Spécialité : Lasers, Matières et Nanosciences

Caractérisation de Métamatériaux pour Applications Millimétriques et Submillimétriques

---

Soutenue le 29 Septembre 2011
Après avis de :

- M. F. FALCONE	Professeur, Universidad Pública de Navarra (Spain)	Rapporteur
- M. K. MAHDJOUBI	Professeur, Université de Rennes 1	Rapporteur

Devant la commission d'examen formée de :

- M. J. P. PARNEIX	Professeur, ENSCBP	Président
- M. F. FALCONE	Professeur, Universidad Pública de Navarra (Spain)	Rapporteur
- M. K. MAHDJOUBI	Professeur, Université de Rennes 1	Rapporteur
- M. E. LHEURETTE	Professeur, Université de Lille 1	Examinateur
- M. P. MOUNAIX	Directeur de recherche, Université de Bordeaux 1	Directeur de thèse
- Mme. V. VIGNERAS-LEFEBVRE	Professeur, ENSCBP	Directrice de thèse
- M. S. N. BUROKUR	Maitre de conférences, Université Paris 10	Membre invité
- M. H. NEMEC	Chercheur, Institut of Physics of Prague (Czech Republic)	Membre invité

To my dear parents Mohamed and Naïma who have always preoccupied themselves for my education, my success and who stimulate me continuously to seek knowledge.

Acknowledgements

This work would not have been possible without the support of my parents over the years, thank you Dad and Mom.

I would like to thank my advisors Dr. Patrick Mounaix and Prof. Valérie Vigneras for giving me the opportunity to work with them, for providing me sufficent guidance for successful research, and for allowing me enough freedom to pursue my own ideas. Their advice and encouragement have been a great inspiration over the years.

I would like to thank my doctoral comittee members for having evaluated my work: Prof. Jean Paul Parneix, Prof. Francisco Falcone, Prof. Kouroch Mahdjoubi, Prof. Eric Lheurette, Dr. Shah Nawaz Burokur and Dr. Hynek Němec.

I would like to thank my collaborators without whom some of my work would not have been possible. Especially Prof. Peter Kuzěl for the welcome in his research group at the Institute of Physics of Prague, and for providing all necessary needs during my stay in the Czech Republic. Thanks also to my colleagues Dr. Filip Kadelec, Dr. Christelle Kadelec and Vladimir Skoromet. I would also like to thank Dr. Shah Nawaz Burokur, my former co-supervisor during my Master's internship, and now one of my collaborators, for having accepted the invitation to participate in my defence.

I would like to thank Dr. Gilles Ruffié and Dr. Laurent Oyenhart for their help in the microwave experimental setups, and Dr. Jean-Christophe Delagne for optimizing the terahertz spectroscopy experiment. I would also like to thank Eddie Maillard and Sandra Bosio for fabricating the holes-array metamaterials with the LOMA facilities, Dr. U-Chan Chung for fabricating the TiO_2-microparticles-based metamaterials by chemical synthesis with the ICMCB facilities. Thanks also to Philippe Maire for fabricating the experimental prototypes using the standard lithography and for fruitful discussions.

I would also like to acknowledge the financial support I have received from the GIS-AMA-SAMM project. Thanks to Dr. Ashod Aradian, the coordinator of this project and to Dr. Olivier Fouassier for managing my travels and conferences.

I would like to thank the administrative and the computer science staff, especially: Laurette Geneste, Isabelle Guillaume, Richard Perrier and Hassen Akrache. Special thanks to my colleagues and friends from LOMA, IMS, CRPP and CELIA laboratories (including former members): Prof. Lionel Canioni, Prof. Mario Maglione, Dr. Bruno Bousquet, Dr. Arnaud Royon, Dr. Inka Manek-Hönninger, Dr. Grégoire Travaillé, Dr. Edwin Nguema, Dr Mathieu Bellec, Dr. Guillaume Lunet, Dr. Hussein Kassem, Sylvain Lannebère, Romain Royon, Aicha Younus, Amina Ismaël, Mohamed El Ketara, Josette El Haddad, Gautier Papon, Romain Catoor and Michaël Mounaix. Finally, special thanks to my dear sisters Sonia (and his daughter Melia) and Siham, thanks also to my uncle M'hamed and his wife Sabah, my cousins Lila, Dalya, Ilyes, and all my family.

Table of Contents

2 Non-Destructive Measurements: Free Space Microwave Setup and Terahertz Time Domain Spectroscopy

3 Investigations of Metamaterials at Microwave Frequencies

List of Figures

Figure

List of Tables

Table

Chapter 1

Introduction to Metamaterials

1.1 Introduction

In 1915, William Laurence Bragg proposed the first Photonic Crystal, which consisted of an alternating sequence of transparent plane layers of different refractive indices that can reflect 99.5% of the incident light. The light (incident wave) is partially reflected and transmitted at each interface between two layers and supposed to be close to the normal incidence, as illustrated in figure 1.1(a). In 1987, Photonic Crystals underwent a new birth with the pioneering works of Eli Yablonovitch, trying to reduce the spontaneous emission of light in lasers and semiconductors (Yablonovitch, 1987). He proposed to extend the concept of Bragg Mirrors at microwave frequencies for any incident angles by a design in two and three dimensions. In 1991, he proposed an artificial photonic band gap material called "Yablonovite" (Yablonovitch, 1990, Yablonovitch, 1993) at the operating frequency of about 14 GHz (figure 1.1(b)). This structure is made of a bloc of Plexiglas that has been machined in three dimensions in order to reproduce the crystal structure of diamond, which is considered as the best natural structure in term of reflection. Professor Yablonovitch has demonstrated theoretically and experimentally that the periodic structures have the ability to inhibit the propagation of modes in certain frequency bands. The photonic bandgap materials have been designed first for applications in optics such as: semiconductors light-emitting, high reflectivity mirrors, microcavities and filters. Photonic band gap materials working at centimeter and millimeter wavelengths, which are much easier to fabricate have also attracted the interest of researcher, particularly in the field of antennas in order to suppress surface waves.

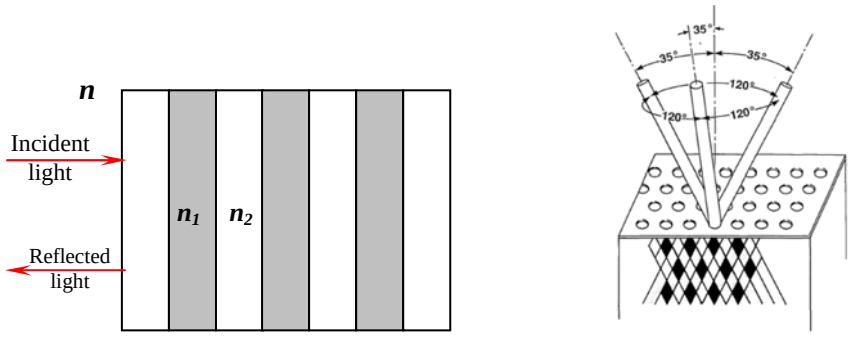

(a) (b)

Figure 1.1: (a) Principle of Bragg mirror, (b) "the Yablonovite", the artificial photonic band gap material proposed by Eli Yablonovitch (Yablonovitch, 1990, Yablonovitch, 1993).

In a photonic crystal, the propagation of photons is hampered by electrons giving rise to allowed and forbidden frequency bands for photons. By analogy to photonic bandgap materials, researchers have introduced a new terminology: Electromagnetic Bang Gap (EBG) structures to designate a new class of artificial materials, which inhibit the propagation of waves at certain incidence angles and certain frequency bands in the microwave regime. The equation of electromagnetic waves propagation

in these structures, governed by Maxwell's equations is similar to Schrödinger equation that describes the wave function of an electron in a solid crystal. Due to their periodicity, these structures have the ability to control electromagnetic waves and to act as a frequency and spatial filters. In the recent few years, a new category of materials commonly called "metamaterials", have revolutionized the world of physics with their unusual properties that do not exist in nature such as: high impedance medium, in-phase reflection, negative permittivity, negative permeability, negative refractive index, and so on. Since the pioneering works of V. Veselago (Veselago 1968), J. B. Pendry et al (Pendry, 1998, Pendry, 1999), and R. A. Shelby et al (Shelby, 2001), a large number of researchers have contributed to the development and the growth of this new generation of materials, which offer possibilities to manipulate electromagnetic waves in an extraordinary way (Fang, 2005, Schurig, 2006). The purpose of our work, which has been performed within the framework of the project: GIS-AMA-SAMM (Groupement d'intérêt Scientifique – Advanced Materials in Aquitaine – Self Assembled Metamaterials) is to develop metamaterials at microwave and terahertz frequency ranges with the aim to provide improved functionalities and performances for millimeter and sub-millimeter applications. This dissertation deals with the achievements of the project and is organized into five chapters:

In the first chapter of this dissertation, fundamental properties of negative refractive index metamaterials are reminded. We will see that a metamaterial can be represented as an effective medium characterized by constitutive and propagative effective parameters. A retrieval method used to extract these effective parameters is described and discussed. A general presentation of different categories of metamaterials is given and finally, a superlens, which is a promising application of metamaterials is discussed.

The second chapter begins with a brief overview about the most common numerical calculation methods, widely used for predicting and analyzing the behavior of metamaterials. Subsequently, we will focus on different elements constituting experimental setups that have been used in our research. Both Vector Network Analyzer (VNA) with horn antennas and Terahertz Time Domain Spectroscopy (THz-TDS) have been used at microwave and terahertz frequency range, respectively in order to carry out experiments on our fabricated prototypes.

The third chapter of this dissertation is dedicated to the study of metamaterials at microwave frequencies. Different structures have been designed, fabricated and experimentally characterized, such as: Frequency Selective Surfaces and negative refractive index metamaterials, so called ″fishnet metamaterials″. Both standard optical lithography and mechanical machining technique have been used in order to fabricate our experimental prototypes. Simulations and measurements have been performed using the full wave 3D simulator HFSS, based on the finite element method and a network vector analyzer and horn antennas setup, respectively. The potential application of the FSS as a Partially Reflecting Surface (PRS) reflector Fabry–Pérot (FP) cavity is proposed and evaluated in

order to enhance the directivity of printed patch antennas. Finally the negative refractive index exhibited by our proposed metamaterials is demonstrated numerically and experimentally.

In the fourth chapter of this dissertation, we present metamaterials studied in the teraherz frequency range. Both All Dielectric (AD) metamaterials and fishnet metamaterials have been investigated. Experimental prototypes have been fabricated and measured using THz-TDS in order to demonstrate the theoretical predictions. The last chapter of this dissertation summarizes the work performed and gives some potential perspectives to inspire further experimental and theoretical investigations and perhaps some technological applications as well.

1.2 Fundamental Properties of Negative Refractive Index (NRI) Metamaterials

In this section, we will discuss about the fundamental electromagnetic properties and the propagation of an electromagnetic wave in a medium, where both permittivity and permeability are simultaneously negative.

1.2.1 Propagation of Electromagnetic Waves in a Medium Characterized by μ and ε Simultaneously Negative

Taking into account Maxwell's equations governing the propagation of a monochromatic plane wave in a linear, homogeneous, isotropic, free from sources, and non-dispersive media characterized by a dielectric permittivity **ε** and a magnetic permeability $\boldsymbol{\mu}$, one can write the following expressions:

$$\vec{k} \times \vec{E} = \omega \mu \vec{H}, \tag{1.1}$$

$$\vec{k} \times \vec{H} = -\omega \varepsilon \vec{E}, \tag{1.2}$$

For positive values of μ and ε, the triplet of vectors $\boldsymbol{E}$, $\boldsymbol{H}$, $\boldsymbol{k}$ is direct and is given by the right hand rule (see figure 1.2(a)), however for values of μ and ε simultaneously negative, the wave vector triplet is indirect and is given by the left hand rule as illustrated in figure 1.2(b). This rule confers to negative refractive index materials the terminology "Left Handed Materials".

RHM LHM

Figure 1.2: Triplet of vectors E, H, k in a Right Handed Material (RHM) and Left Handed Material (LHM), respectively.

The modulus of wave vector can be written as follow:

$$\left|\vec{k}\right| = \omega\sqrt{\mu\varepsilon}, \tag{1.3}$$

For values of $\boldsymbol{\mu}$ and $\boldsymbol{\varepsilon}$ located in the second (II) and the forth (IV) quadrant of figure 1.3, the wavevector $\boldsymbol{k}$ is purely imaginary, giving rise to an evanescent waves regime. When $\boldsymbol{\mu}$ and $\boldsymbol{\varepsilon}$, are located in the first (I) and the third (III) quadrant, $\boldsymbol{k}$ is purely real and the medium allows the propagation of electromagnetic waves. Note that the propagation in the first quadrant is very different from the propagation in the third quadrant. The flow of energy carried by the wave is given by the Poynting vector $\vec{S}$:

$$\vec{S} = \frac{1}{2}\vec{E}\times\vec{H}^{*}, \tag{1.4}$$

In the third quadrant, $\boldsymbol{S}$ is anti- parallel to $\boldsymbol{k}$, and the propagation is accompanied by a negative phase velocity $\boldsymbol{v_\varphi}$ and a positive group velocity $\boldsymbol{v_g}$, thus the resulting front waves are moving towards the source rather then away from the source (veselago, 1986)

$$v_\varphi = \frac{\omega}{k} < 0, \tag{1.5}$$

$$v_g = \frac{\partial\omega}{\partial k} > 0, \tag{1.6}$$

Further physical phenomena are reversed in the presence of negative refractive index materials such as: Snell's law, Doppler Effect and Cherenkov radiation (veselago, 1986).

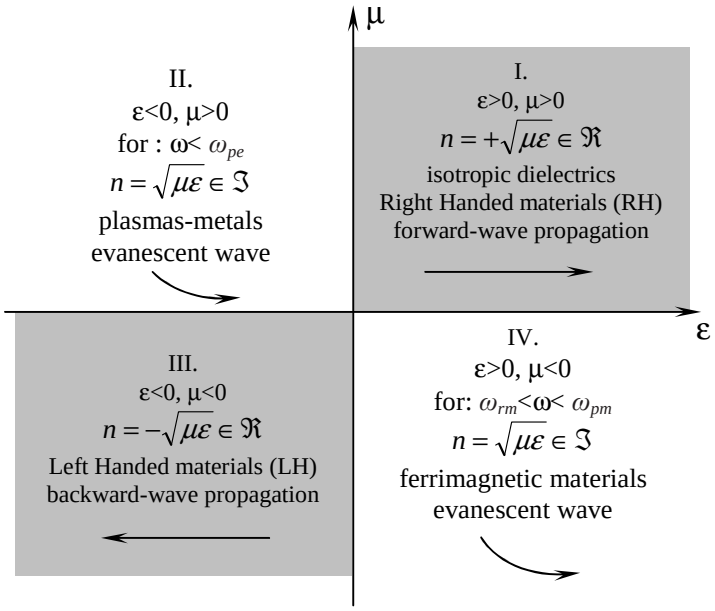

Figure 1.3: Nature of electromagnetic waves interacting with a medium for different signs of the couple (ε_{eff}, μ_{eff}). The angular frequencies ω_{pe} and ω_{pm} represent the electric and magnetic plasma frequencies, respectively and ω_{rm} is the magnetic resonant frequency.

Most of isotropic dielectric materials belong to the first quadrant (μ> 0 and ε>0), the second quadrant (μ>0 and ε<0), is occupied by solid and gas state plasmas (veselago, 1986) and till now, no natural material belongs to the third quadrant (μ< 0 and ε<0). The last quadrant (μ<0 and ε>0) corresponds to the domain of magnetic materials such as ferrites, which are widely used in the fabrication of a large panel of non-reciprocal microwave systems such as isolators, circulators and phase shifters, taking advantage of the negativity of some elements of the tensor [μ]. Two main constraints related to the principle of causality and the electromagnetic energy conservation law should be taken into account for a Double NeGative (DNG, ε<0 and μ<0) metamaterial: spectral dispersion and absorption (*entropy conditions in dispersive media*). Indeed, the propagation of electromagnetic waves in DNG is neccessarily accompanied by frequency dispersion, according to the following expression of the total energy W (Veselago, 1968):

$$W = \frac{1}{2}\frac{\partial(\omega\varepsilon(\omega))}{\partial\omega}|E|^2 + \frac{1}{2}\frac{\partial(\omega\mu(\omega))}{\partial\omega}|H|^2, \tag{1.7}$$

If the external supply of electromagnetic energy to the structure is cut off, absorption ultimately converts the energy W entirely into heat. By the *law of entropy*, specifying that the entropy of a system is an ever increasing quantity, there must be evolution and not absorption of heat (Landau, 1984). We therefore must have W>0, which leads in the general (dispersive) case to the following conditions:

$$\frac{\partial(\omega\varepsilon(\omega))}{\partial\omega} > 0, \tag{1.8}$$

$$\frac{\partial(\omega\mu(\omega))}{\partial\omega} > 0, \tag{1.9}$$

These inequalities do not in general mean that ε and μ cannot be simultaneously negative, but for them to hold it is necessary that ε and μ depend on the frequency (Veselago, 1968).

1.2.2 Boundary Conditions

The mathematical expressions that translate the boundary conditions (BCs) for electromagnetic fields at the interface between two media, which are directly derived from Maxwell equations, are given below:

$$\hat{n}\cdot\left(\overline{D}_2 - \overline{D}_1\right) = \rho_{es}, \tag{1.10}$$

$$\hat{n}\cdot\left(\overline{B}_2 - \overline{B}_1\right) = \rho_{ms}, \tag{1.11}$$

$$\hat{n}\times\left(\overline{E}_2 - \overline{E}_1\right) = -\overline{M}_s, \tag{1.12}$$

$$\hat{n}\times\left(\overline{H}_2 - \overline{H}_1\right) = -\overline{J}_s, \tag{1.13}$$

Where ρ_{es} and ρ_{ms} are electric and magnetic (virtual) surface charge densities on the interface, respectively. n is a unit vector normal to the interface pointing from medium 1 to medium 2.

Equations (1.10) and (1.11) state that in the absence of charges ($\rho_{es} = \rho_{ms} = 0$) at the interface, the normal components of $\boldsymbol{D}$ and $\boldsymbol{B}$ are continuous, whereas equations (1.12) and (1.13) state that in the absence of sources ($\boldsymbol{M}_s = \boldsymbol{J}_s = 0$) at the interface, the tangential and normal components of $\boldsymbol{E}$ and $\boldsymbol{H}$ are continuous as follow:

$$E_{1t} = E_{2t}, \tag{1.14}$$

$$H_{1t} = H_{2t}, \tag{1.15}$$

$$D_{1n} = D_{2n}, \tag{1.16}$$

$$B_{1n} = B_{2n}, \tag{1.17}$$

If we consider now the specific case of an interface between a right hand and a left hand media, as depicted in figure 1.4 (medium 1: RH, medium 2 : LH) the relations (1.14) to (1.17) given above reveal the following.

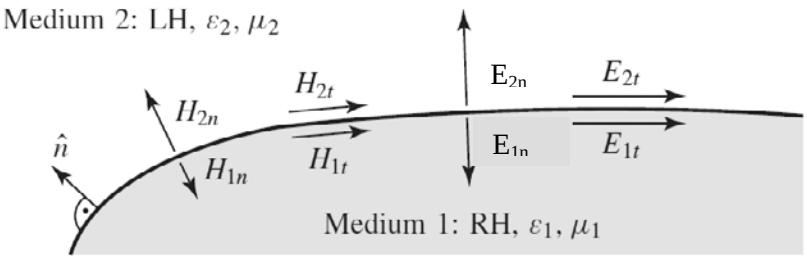

Figure 1.4: Boundary conditions at the interface between a RH medium and a LH medium as reported by (Caloz, 2006).

The boundary conditions on the tangential components of $\boldsymbol{E}$ and $\boldsymbol{H}$ are unaffected at this interface, since the relations on the tangential components do not depend on $\boldsymbol{\varepsilon}$ and $\boldsymbol{\mu}$. In contrast, the BCs on the normal components are necessarily changed since they involve $\boldsymbol{\varepsilon}$ and $\boldsymbol{\mu}$ with changes in signs. Assuming that the LH medium is weakly dispersive and that the constitutive relations $\boldsymbol{D} = \boldsymbol{\varepsilon E}$ and $\boldsymbol{B} = \boldsymbol{\mu H}$ are approximately valid (Caloz, 2006), we obtain the following boundary conditions at a RH/LH interface:

$$E_{1n} = -\frac{\varepsilon_2}{|\varepsilon_1|} E_{2n}, \tag{1.18}$$

$$H_{1n} = -\frac{\mu_2}{|\mu_1|} H_{2n}, \tag{1.19}$$

$$E_{1t} = E_{2t}, \tag{1.20}$$

$$H_{1t} = H_{2t}, \tag{1.21}$$

Finally, we can conclude and say that the tangential components of $\boldsymbol{E}$ and $\boldsymbol{H}$ fields remain continuous, while the normal components are discontinuous and change their signs.

1.3 Homogenization of Metamaterials

The main purpose of the theory of homogenization is to describe in a simple and macroscopic way the microscopic complexity of the response of objects to an incident electromagnetic radiation. Indeed, the idea is to replace the composite system by an equivalent homogeneous system having the same electromagnetic responses. The combination of materials with different natures such as: metallic inclusions in a dielectric matrix give rise to a composite material with new electromagnetic properties, related to different physical characteristics:

- High heterogeneities due to the dielectric contrast between metallic inclusions and dielectric matrix.
- Currents induced by an exciting electromagnetic wave in metallic patterns, these currents can oscillate dependent or independent of the incident wave giving rise to dynamic or static resonances.

Heterogeneous composite materials can scatter the electromagnetic radiation in two different ways. When the subset (heterogeneities) of the composite material are small and separated by subwavelength distances, fields scattered by each particle interfere constructively and remain globally focused in the specular directions (i.e. in the directions of transmission and reflexion), this composite can be considered and replaced by a homogeneous material (figure 1.5(a)). Indeed, in the case of metamaterials, the key to describe these structures as effective homogeneous media is that the structures possess features much less than the operating wavelength, typically ($\leq\lambda/10$).

The second possibility for a heterogeneous material is to scatter the incident electromagnetic radiation in multiple directions, as illustrated in figure 1.5(b). In this case, the composite can not be considered as a homogeneous material.

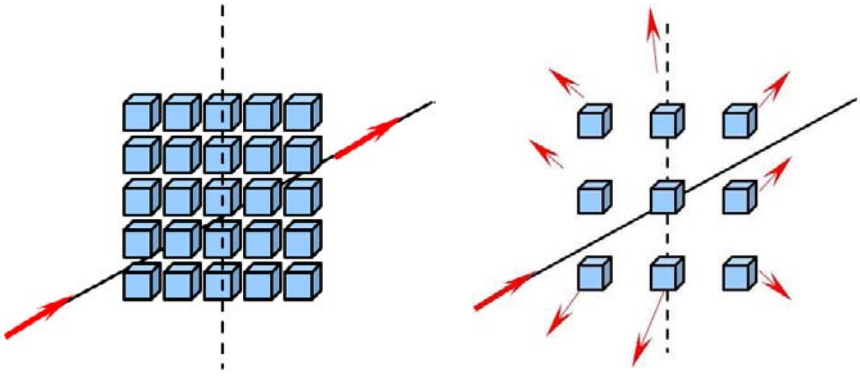

(a) (b)

Figure 1.5: (a) Scattering of the incident electromagnetic radiation in the specular directions for a homogeneous composite (a) and in multiple directions for a non-homogeneous composite (b).

1.4 Retrieval Method of Effective Parameters

The Nicholson-Ross-Wier (NRW) method (Nicolson, 1970, Wier, 1974) used in our research in order to retrieve the effective parameters of our investigated metamaterials is easy to implement and is widely used and discussed in scientific literature (Smith, 2002, Chen, 2004, Smith, 2005, Simovski, 2007). This method is based on the inversion of the complex reflection ***r*** and transmission ***t*** coefficients determined for a slab of compound material (see figure 1.6(a)). Initially proposed for normal incidence on the isotropic metamaterial (Smith, 2002, Chen, 2004) the procedure was modified for oblique incidence (Menzel, 2008), bianisotropic (Chen, 2005, Li, 2009) and chiral metamaterials (Menzel, 2008, Kwon, 2008, Plum, 2009). At first, the wave impedance and the refractive index are calculated; effective permittivity and effective permeability are then deduced. The wave impedance is given by the following expression:

$$Z = \pm\sqrt{\frac{(1+r)^2 - t'^2\, e^{-2jk_0 d}}{(1-r)^2 - t'^2\, e^{-2jk_0 d}}} = 0, \tag{1.22}$$

where $t' = t\,exp(jkd)$ is the normalized transmission, **d** is the thickness of the material, $k_0 = 2\pi/\lambda_0$ is the wavevector and λ_0 the wavelength in free space. The choice of sign in equation (1.22) is fixed by the requirement that Re(**z**)>0 for a passive material, this criterion is demonstrated in section 1.5.2. The expression of the refractive index is given below:

$$\cos(nkd) = \frac{1}{2t'}\left[1-\left(r^2 - t'^2\right)\right] = 0, \tag{1.23}$$

$$\mathrm{Im}(n) = \pm\,\mathrm{Im}\left(\frac{\cos^{-1}\left(\frac{1}{2t'}\left[1-\left(r^2 - t'^2\right)\right]\right)}{kd}\right), \tag{1.24}$$

$$\mathrm{Re}(n) = \pm\,\mathrm{Re}\left(\frac{\cos^{-1}\left(\frac{1}{2t'}\left[1-\left(r^2 - t'^2\right)\right]\right)}{kd}\right) + \frac{2\pi m}{kd}, \tag{1.25}$$

When we solve the right-hand side of equation (1.24), we select which of the two roots yields a positive solution for Im(***n***), as we will demonstrate in section 1.5.1. The real part of the refractive index ***Re***(***n***) is complicated by the branches of the arccosine function, where ***m*** is an integer. When ***d*** is large, these branches can lie arbitrarily close to one another, making the selection of the correct branch difficult in the case of dispersive materials. For this reason best results are obtained for the smallest possible thickness of sample, as has commonly been known in the analysis of continuous materials. Even with a small sample, more than one thickness must be measured to identify the correct branches

of the solution which yields consistently the same values for $\boldsymbol{n}$ (Smith, 2002). The electric permittivity and the magnetic permeability can be expresses as follows:

$$\varepsilon = n / z, \tag{1.26}$$

$$\mu = n \cdot z, \tag{1.27}$$

Further solutions have been proposed in the scientific literature in order to overcome the ambiguity related to the determination of Re ($\boldsymbol{n}$) (Queffélec, 2000, Ziolkowski, 2003, Chen, 2004).

D. K. Ghodgaonkar et al (Ghodgaonkar, 1990) proposed a solution to solve the ambiguity related to the multiform nature of the effective dielectric and magnetic functions. Indeed, the authors started writing the expressions of the complex permittivity $\boldsymbol{\varepsilon^*}$ and permeability $\boldsymbol{\mu^*}$ as follows:

$$\varepsilon^* = \frac{\gamma}{\gamma_0}\left(\frac{1-\Gamma}{1+\Gamma}\right), \tag{1.28}$$

$$\mu^* = \frac{\gamma}{\gamma_0}\left(\frac{1+\Gamma}{1-\Gamma}\right), \tag{1.29}$$

where ε* and μ* are defined as $\varepsilon^* = \varepsilon' - j\varepsilon'' = \varepsilon'(1 - j\tan(\delta_\varepsilon))$, and $\mu^* = \mu' - j\mu'' = \mu'(1 - j\tan(\delta_\mu))$, the propagation constant of the sample $\boldsymbol{\gamma}$ = log[(1/$\boldsymbol{T}$)]/$\boldsymbol{d}$, $\boldsymbol{\Gamma}$ is a complex function depending on the reflexion coefficient $\boldsymbol{S_{11}}$ of the air-sample interface and the transmission coefficient $\boldsymbol{S_{21}}$ through the sample, as illustrated in figure 1.6(a). $\boldsymbol{d}$ and $\boldsymbol{\gamma_0}$ = ($\boldsymbol{j}2\pi/\boldsymbol{\lambda_0}$) are the thickness of the sample and the propagation constant of free space, respectively.

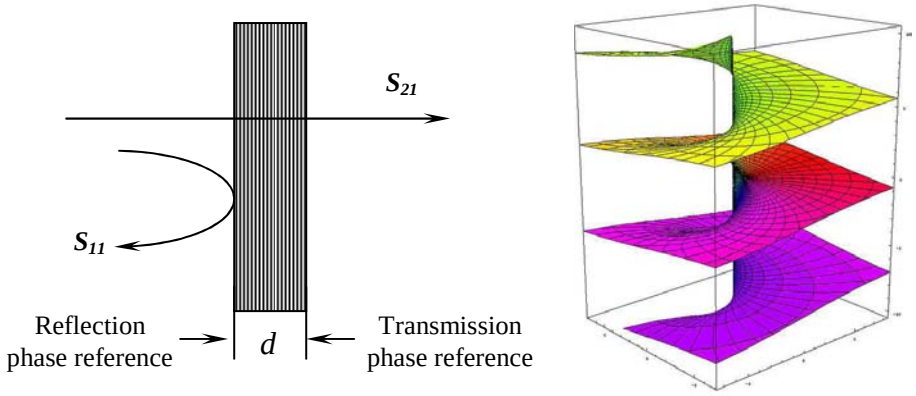

Figure 1.6: (a) Illustration of transmission and reflection coefficients through a planar sample with thickness $\boldsymbol{d}$, reference planes are defined for both transmission and reflection phases. (b) Visualization of the Riemann surface of the complex logarithm function $\boldsymbol{\log x}$, the domains of the branches were glued. The final result is a connected surface that can be viewed as a spiralling parking garage with infinitely many levels extending both upward and downward. This is the Riemann surface $\boldsymbol{R}$ associated to $\boldsymbol{\log x}$.

Since the parameter $\boldsymbol{T}$ in the expression of $\boldsymbol{\gamma}$is a complex number, there are multiple values for $\boldsymbol{\gamma}$. If $\boldsymbol{T}$ is defined as $\boldsymbol{T} = |\boldsymbol{T}|\boldsymbol{e^{j\varphi}}$, then $\boldsymbol{\gamma}$is given by:

$$\gamma = \left[\log\left(1/|T|\right)\right]/d + j\left[\frac{2\pi k - \varphi}{d}\right], \tag{1.30}$$

where k = 0, ±1, ±2, …, the real part of γ is unique and single valued, but the imaginary part of γ has multiple values, So equations (1.28) and (1.29) will give multiples values of ε^* and μ^*. In mathematics, particularly in complex analysis, the multiform functions (for each antecedent k, corresponds multiple images) are considered as the origin of Riemann Surfaces, as depicted in figure 1.6(b), which illustrates the Riemann surface of the complex logarithm function. The phase constant β is defined as:

$$\beta = (2\pi/\lambda_m) = \text{imaginary part of } (\gamma), \tag{1.31}$$

where $\lambda_m = \lambda_0/\sqrt{\varepsilon_r}$ is the wavelength in the material sample, λ_0 corresponds to the operating wavelength in free space and ε_r the relative permittivity of the dielectric substrate, from equations (1.30) and (1.31), d/λ_m can be expressed as follows:

$$d/\lambda_m = k - \frac{\phi}{2\pi}, \tag{1.32}$$

For k = 0, and $-2\pi < \phi < 0$, (d/λ_m) is between 0 and 1. If the sample thickness d is chosen such that it is less then λ_m, equations (1.28) and (1.29) will give unique values of ε^* and μ^* which corresponds to k = 0. Thus, the ambiguity related to ε^* and μ^* can be resolved. See appendix A, for the description in details of this method.

Another criterion that can contribute in the choice of the right branch, thus helping to leave the ambiguity related to the multiple values of effective parameters is related to the value of the real part of effective permeability μ^*. Indeed, this later must be equal to unity far away the magnetic resonant frequency, in the low-frequency-side (quasi-static mode) if all elements constituting the investigated metamaterial possess permeabilities equal to unity, as reminded by (Lagarkov, 2009). A more intuitive explanation is that the artificial magnetic effective permeability (resonant behavior, magnetic activity) is generated by induced currents that can exist only if the incident magnetic field varies in time, according to Lorentz law.

1.5 Physical Meaning and Appropriate Signs of Effective Parameters in Metamaterials

In this section, we will discuss about physical criteria that have been used in order to allow us to choose appropriate signs of complex effective parameters of our investigated metamaterials.

1.5.1 Complex Refractive Index (n)

The complex refractive index ***n*** provides information about the propagation of an incident electromagnetic wave within a medium. If the absolute value of the real part of the refractive index is larger than its imaginary part, the medium allows the propagation of waves. The refractive index of a double negative metamaterial (μ<0 and ε<0) can be defined as follows:

$$n(\omega) = \pm\sqrt{\varepsilon(\omega)\mu(\omega)}, \tag{1.33}$$

In order to demonstrate that for a material with both μ and ε negative, the refractive index ***n*** is negative, we will study in this material, the radiating properties of a current sheet (current density localized to the position $\mathbf{x_0}$) located at $x = x_0$ (Smith, 2000), as depicted in figure 1.7.

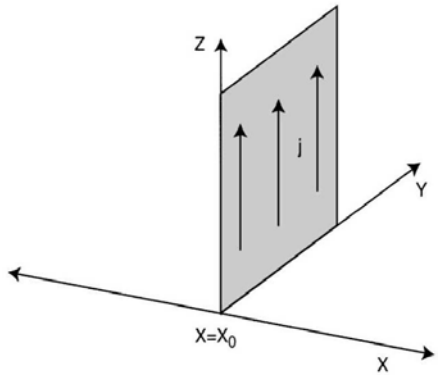

Figure 1.7: Current sheet at $x = x_0$ radiating into a medium with μ<0 and ε<0, the sheet is considered uniform and infinite along *y* and *z* axes, according to (Smith, 2000).

The wave equation in the medium can be written as follow:

$$\frac{\partial^2}{\partial x^2}E(x) + \frac{\omega^2}{c^2}\mu\varepsilon E(x) = -\frac{4\pi j\omega}{c^2}\mu j_0\delta(x - x_0)z, \tag{1.34}$$

where $E(x)$ is the component of the electric field along ***x*** direction, $j_0\,\delta(x-x_0)\,z$ is the magnitude of the current density oriented along the ***z*** axis. Equation (1.34) has a solution of the form:

$$E(x,t) = -2\pi\frac{Z}{c}\,j_0\exp\left(j\left(nk|x - x_0| - \omega t\right)\right), \tag{1.35}$$

where $Z = \mu/n$, is the wave impedance, when the product $\mu\varepsilon$ is real and positive, there are two types of solutions, corresponding to the sign of ***n*** being positive or negative. When ***n***<0, it means that wave fronts of an incident plane wave propagate toward the source rather than propagate away from the source. We employ a general method that will distinguish the physical solution of equation (1.35) without presuming the sign of the refractive index. The average power supplied by the current J_0 to the volume ***V*** is given by the following expression (Smith, 2000):

$$P = \omega W = -\frac{1}{2}\int_V E(x,\omega)J^*dx = \pi\frac{\mu}{cn}\,j_0^2, \tag{1.36}$$

To identify the physical solution, we require that the source on average do positive work on the fields or that the quantity ***P*** given above be greater than zero. Equation (1.36) represents the work done by the source. Since ***P*** is always positive, this implies that the ratio μ / n should be positive. If μ is negative, ***n*** is also negative. Note that the medium is a "propagative medium" and the solution of the wave equation satisfies the condition of backward waves. The sign of the imaginary part of the refractive index is restricted by a stability condition related to the propagation of electric and magnetic fields. Indeed, if we consider a medium with refractive index $n = n' - j\,n''$ and the convention of time dependence in $\exp(+j\omega t)$, the expression of the electric field can be written as follows:

$$\vec{E}(\vec{r},t) = \left|\vec{E}(\vec{r})\right| \exp\left(-\vec{k}_0 \cdot \vec{r} n''\right) \times \exp\left(j\left(\omega t - \vec{k}_0 \cdot \vec{r} n'\right)\right)\vec{U}_E, \tag{1.37}$$

where k_0 is the wavevector in free space, U_E is the unit vector in the direction of the electric field. In order to have a stability in the propagation of the electric field, it is necessary that the amplitude of $\vec{E}(\vec{r},t)$ decreases with time, implying that $\vec{k}_0 \cdot \vec{r} n''$ must be positive:

$$\vec{k}_0 \cdot \vec{r} n'' > 0 \Rightarrow n'' > 0, \tag{1.38}$$

The imaginary part of the refractive index n'' is positive, independently from its real part. We can also show that $n'' > 0$, for the time convention $\exp(-j\omega t)$ and $n = n' + j\,n''$.

1.5.2 Complex Wave Impedance (z)

The concept of impedance initially applied to electrical circuits, has been extended to electromagnetic waves. The analogy between the impedance exhibited by a medium illuminated by an incident plane wave and the impedance exhibited by a transmission line is discussed by (Stratton, 1944). The notion of complex impedance wave is related to the flux of energy within the investigated medium. The values of the wave impedance are restricted by a fundamental physical limit related to the passivity of the medium.

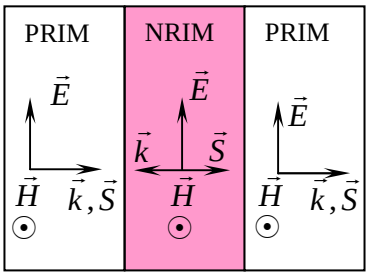

Figure 1.8: Orientation of vectors ***E***, ***H***, ***k*** and ***S*** during an interaction of a plane wave with a PRI and a NRI materials.

Indeed, in the absence of activity within the structure, the real part of the wave impedance ***z*** must be positive, we propose in this section to demonstrate that this restriction can be applied to any

refractive index material.The passivity or the absence of activity in a medium implies that for an incident propagating plane wave, the average flux of the electromagnetic energy should be oriented inside the medium, in which the propagation of the wave occurs (Wohlers, 1971).The orientation of vectors (***E***, ***H***, and ***k***) and the energy flux ***S*** for a propagating plane wave, interacting with a PRI (Positive Refractive Index) material and a NRI (Negative Refractive Index) material is depicted above in figure 1.8. The wave impedance is defined as the ration of the electric field to the magnetic field in the plane of propagation, the real part of ***z*** can be expressed as follow:

$$\mathrm{Re}[Z(\omega)] = \mathrm{Re}\left[\frac{\overline{E}(\omega)}{\overline{H}(\omega)}\right] = \frac{\left|\overline{E}(\omega)\right|}{\left|\overline{H}(\omega)\right|}\cos(\varphi_H - \varphi_E), \tag{1.39}$$

where:

$$\overline{E}(\omega) = \left|E(\omega)\right|\exp(-j\varphi_E), \text{ and } \overline{H}(\omega) = \left|H(\omega)\right|\exp(-j\varphi_H)$$

The sign of ***Re***[***Z***(***ω***)] depends only on the sign of cos(***φ***$_H$ - ***φ***$_E$), the average Poynting vector ***S***$_{av}$ can be expressed as follow:

$$\vec{S}_{av} = \frac{1}{2}\mathrm{Re}\left[\vec{E}(\vec{r},\omega)\times\vec{H}^{*}(\vec{r},\omega)\right] = \frac{1}{2}\left|\vec{E}(\vec{r},\omega)\right|\left|\vec{H}(\vec{r},\omega)\right|\cos(\varphi_H - \varphi_E)\vec{U}_S, \tag{1.40}$$

with:

$$\vec{E}(r,\omega) = \left|\vec{E}(\vec{r},\omega)\right|\exp(-j\varphi_E) \text{ and } \vec{H}(\vec{r},\omega) = \left|\vec{H}(r,\omega)\right|\exp(-j\varphi_H),$$

U$_S$ is the unit vector in the direction of the pointing vector. By definition, equation (1.40) is satisfied for both PRI and NRI materials, taking into the count the passivity of the medium, the Poynting vector should be oriented inside the medium (i.e. ***S***$_{av}$ (***r***,***ω***)>0), the expression cos(***φ***$_H$ - ***φ***$_E$) is then always positive for both PRI and NRI materials. If we apply this restriction to equation (1.39), we obtain the condition:

$$\mathrm{Re}[Z(\omega)] > 0, \tag{1.41}$$

The real part of the wave impedance is positive for any refractive index value and for any time convention [***exp***(-***jωt***) or ***exp***(+***jωt***)]. This condition allows us to define physical solutions, during the calculation of effective parameters. The imaginary part of wave impedance gives us further information about the propagation. Indeed, when ***Im***(***z***)>***Re***(***z***) (i.e. absence of propagation). The sign of ***Im***(***z***) allows to know which component of the electromagnetic wave (***E*** or ***H*** field) is inhibited. If we consider that ***Im***(***z***)>0 for the convention ***exp***(+***jωt***) [or ***Im***(***z***)<0 for the convention ***exp***(-***jωt***)], the medium is inductive in nature, a static magnetic field is available within the medium, the electric field ***E*** is inhibited and the electromagnetic wave can not propagate. The same reasoning can be done for a capacitive medium characterized by ***Im***(***z***)<0 for the time convention ***exp***(+***jωt***).

1.5.3 Complex Permittivity (ε) and Permeability (μ)

The complex permittivity ε is considered as the response of the medium to an incident electric field. The real part of ε is representative of the alignment of electric dipoles with respect to an incident electric field E. A positive value of $Re(\varepsilon)$ means that the electric dipoles are parallel to the electric field, while a negative value of $Re(\varepsilon)$ means an anti-parallel alignment. The imaginary part of ε allows to quantify the dissipated energy due to the interaction of the electric field with the medium. The complex magnetic permeability μ is the analogous of the permittivity, applied to the magnetic field. The imaginary parts of the permittivity ε'' and permeability μ'' of any linear, homogeneous, passive (in thermodynamic equilibrium), dielectric-magnetic material are always positive, independent of the signs of their real parts, thus assuming a time dependence of the form: $exp(-j\omega t)$, where $j = \sqrt{-1}$, ω is the angular frequency and t denotes the time. The complex electric permittivity and the complex magnetic permeability are defined as: $\varepsilon(\omega) = \varepsilon'(\omega) + j\varepsilon''(\omega)$ and $\mu(\omega) = \mu'(\omega) + j\mu''(\omega)$, respectively. This criterion constitutes one of the most important theorems in the macroscopic electrodynamics as reported by (Depine, 2004, Efros, 2004). It has been demonstrated in several ways, by Callen et al using the theorem of fluctuation-dissipation (Callen, 1951), for any linear and dissipative systems, and by Landau et al (Landau, 1984) for electromagnetic waves. Indeed, uing maxwell's equations, the dissipated energy W at the frequency domain can be expressed as follows (Landau, 1984):

$$W = \frac{1}{4\pi}\int d\omega \cdot \omega\left(\varepsilon''(\omega)\left|\vec{E}(\vec{r},\omega)\right|^2 + \mu''\left|\vec{H}(\vec{r},\omega)\right|^2 \right), \tag{1.55}$$

Here, W is the dissipated energy, $E(\omega)$ and $H(\omega)$ are the electric and the magnetic fields, while $\varepsilon''(\omega)$ and $\mu''(\omega)$ are the imaginary parts of the relative permittivity and relative permeability, respectively. This dissipated energy is written as a function of $\varepsilon''(\omega)$ and $\mu''(\omega)$. The terms of right side of equation (1.55) are electric and magnetic losses, respectively. Taking into acount the law of increase of entropy, the sign of these losses is determinate: the dissipation of energy is necessarily accompanied by the evolution of heat, which implies that $W>0$. It therefore follows that imaginary parts of ε and μ are always positive for all substances and at all frequencies (Landau, 1984), as follows:

$$\varepsilon''(\omega)>0 \text{ and } \mu''(\omega) >0, \tag{1.57}$$

It should be noted that the expression of Maxwell's equations and the Poynting theorem remain valid and unchanged for a NRI material (Veselago, 1969). Indeed, only the direction of the wavevector k is changed in a NRI material, leading to the product: $S.k < 0$. The expressions of the average Poynting vector in a dispersive medium excited by a superposition of two monochromatic waves of angular frequencies ω_1 and ω_2, respectively is given below (Pacheco-Jr, 2002):

$$< \vec{S}(\bar{r},t) >= \frac{|E|^2}{2}\left(\frac{\vec{k}(\omega_1)}{\omega_1 \mu(\omega_1)} + \frac{\vec{k}(\omega_2)}{\omega_2 \mu(\omega_2)} \right), \tag{1.58}$$

This equation shows the relationship between the direction of the Poynting vector *S* and the wavevector ***k***. The direction of the Poynting vector ***S*** is independent from the sign of the refractive index for any propagative medium (i.e. ***k*** is real) we obtain a ratio $\boldsymbol{k}/\boldsymbol{\mu} > 0$, if ***k*** is negative $\boldsymbol{\mu}$ is also negative. Finally, the criterion of equation (1.57) is valid for continuous NRI material. It should be noted that a NRI material is necessarily dispersive and it can be excited by a non-monochromatic incident wave. Note that for a temporal convention of the form: $\boldsymbol{exp}(+\boldsymbol{j\omega t})$, the dispersive parameters are written in terms of their complex conjugate [i.e. $\boldsymbol{\varepsilon}(\boldsymbol{\omega}) = \boldsymbol{\varepsilon}'(\boldsymbol{\omega}) - \boldsymbol{j\varepsilon}''(\boldsymbol{\omega})$ and $\boldsymbol{\mu}(\boldsymbol{\omega}) = \boldsymbol{\mu}'(\boldsymbol{\omega}) - \boldsymbol{j\mu}''(\boldsymbol{\omega})$], and the imaginary parts of $\boldsymbol{\varepsilon}$ and $\boldsymbol{\mu}$ are then negative. Finally, we can summarize in table 1.1 the signs of effective electromagnetic parameters in a left handed material according to physical phenomena that have been discussed in previous sections:

	time dependence exp(-jωt)	time dependence exp(+ jωt)
$\boldsymbol{\mu'}$	-	-
$\boldsymbol{\mu''}$	+	-
$\boldsymbol{\varepsilon'}$	-	-
$\boldsymbol{\varepsilon''}$	+	-
$\boldsymbol{z'}$	+	+
$\boldsymbol{z''}$	+/-	+/-
$\boldsymbol{n'}$	-	-
$\boldsymbol{n''}$	+	+

Table 1.1: Summary of signs of effective parameters for a left handed material for the two time dependence of the fields.

1.6 Different Categories of Metamaterials

In this section, we will discuss about different classes of metamaterials that have been proposed over the last few years by several research groups, in order to obtain desired electromagnetic properties.

1.6.1 Composite Metal-Dielectric Metamaterials

Composite metamaterials based on metallic inclusions in a dielectric matrix, have been the first metamaterials to be proposed. They gave rise to the first negative refractive index by a superposition of two different structures: Split Ring Resonators (Pendry, 1998) and continuous wires (Pendry, 1999) in a frequency band, where both the permittivity and the permeability are simultaneously negative.

a. Continuous Wires: Negative Permittivity Medium

Plasmas are considered as the only dielectrics available with a negative permittivity. In order to approximate the electrical properties of plasmas at microwave regime, a structure composed of a dielectric material with an array of metallic rods periodically arranged, has been proposed in the early 50's (Brown, 1953, Rotman, 1962). More recently, J. B. Pendry et al (Pendrey, 1998) introduced a theory that allows connecting the quantum parameters of plasma to the geometrical dimensions of the rods-array (figure 1.9).

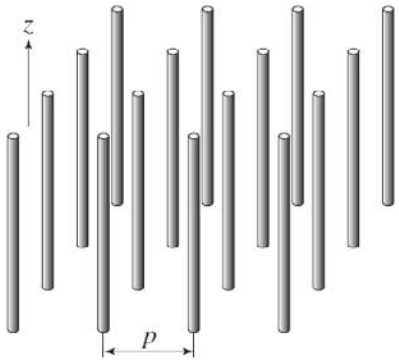

Figure 1.9: First metamaterial (thin-wires array), proposed by J. B. Pendry exhibiting negative effective permittivity $\boldsymbol{\varepsilon}$ if $\boldsymbol{E}\|\boldsymbol{z}$ (Pendry, 1998), the inter-element spacing $\boldsymbol{P}$, is much larger then the radius of each rod.

The plasma frequency of metals is typically located in the visible and near ultraviolet spectrum (~ PHz) and the concept of plasmons, allows assimilating the behaviour of metals to plasma of electrons. Once exposed to an electromagnetic radiation, the electron cloud of the metal atoms moves from one region to another, which creates an excess of charges of opposite signs compared to the initial equilibrium state. That gives rise to a return force due to a harmonic motion characterized by the following angular frequency ω_p:

$$\omega_p^2 = \frac{Ne^2}{\varepsilon_0 m_{eff}}, \tag{1.59}$$

where $\boldsymbol{\omega_p}$ is the angular plasma frequency, $\boldsymbol{N}$ the charge's volume concentration, $\boldsymbol{e}$ and m_{eff} are the charge and the effective mass of electron, respectively. According to Drude model, the dielectric function can be expressed as the following:

$$\varepsilon(\omega) = 1 - \frac{\omega_p^2}{\omega(\omega - j\gamma)}, \tag{1.60}$$

where $\boldsymbol{\gamma}$ is the dissipation parameter. At lower frequencies (~ GHz), the dissipation is very important and it makes virtually impossible the observation of this phenomenon. The solution proposed by J. B. Pendry (Pendry, 1998) consists to use a metallic rods-array rather then a metal sheet, which allows reducing the average concentration of electronic charges in the medium. Moreover, it increases the

effective mass of electrons due to the self-inductance of each rod, leading to the decrease of the plasma frequency into microwave range, according to equation (1.59).

b. Split Ring Resonators: Negative Permeability Medium

In order to obtain structures with different magnetic responses without using magnetic materials, J. B. Pendry (Pendry, 1999) proposed the insertion of both inductive and capacitive elements, as depicted in figure 1.10(a). The functioning principle is based on the resonant interaction between the self-inductance of a hollow metal and its capacitive elements. Once exposed to a magnetic field, polarized along the axis of the cylinder, the conducting currents flowing around the cylinder give the impression that this latter supports free magnetic poles, as in the case of a bar magnet. Each element of the structure behaves as a magnetic dipole and the structure can be regarded as a medium with permeability different from the unity, or even negative. To apply the effective medium theory to this structure composed of a series of SRR periodically distributed in a dielectric matrix, the dimensions of each element should be very small compared to the operating wavelength (Pendry, 1999). The effective magnetic permeability follows a Lorentz-like model according to the following expression:

$$\mu(\omega) = 1 - \frac{A\omega^2}{\omega^2 - \omega_{mp}^2 - j\Gamma\omega}, \tag{1.61}$$

where A is a constant, ω_{mp} is the magnetic plasma frequency of the system and Γ is the dumping factor, representing all the losses and the scattering mechanisms. The effective magnetic permeability shows a resonant behaviour, which leads to negative values of μ within a frequency band between the resonant frequency ω_0 and the magnetic plasma frequency ω_{mp}, as depicted in figure 1.10(b).

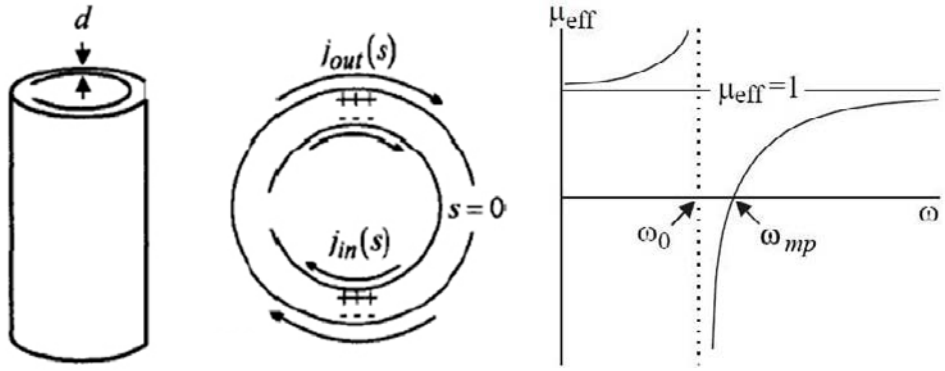

(a) (b)

Figure 1.10: (left panel) First negative μ metamaterial proposed by J. B. Pendry (Pendry, 1999), (a) side view, (b) top view, (right panel) magnetic effective permeability of the SRR.

At this stage, it is important to establish a parallel and to point out the place of conventional magnetic materials in the age of metamaterials. Indeed, it is interesting to remind the means used to create a static magnetic induction B and those used to generate a magnetic effective response μ_{eff} at

high frequencies. Static fields can be generated by materials (permanent magnets), currents (solenoids, Helmoltz coils, …) or by the combination of materials and currents (electro-magnet). In the case of metamaterials, the magnetic effective response results from currents that are induced in inductive metallic patterns, under the effect of an incident magnetic field $\boldsymbol{H}$.

Traditional magnetic materials are usually desired for their large values of permeabilities. For applications such as: inductor core, transformer core and magnetic recording head, we look for low levels of losses. On the contrary, for filtering or high frequencies parasitic absorber applications, we look for large levels of losses in the frequency band to be rejected. Figure 1.11(a) shows the typical permeability of a thin magnetic layer.

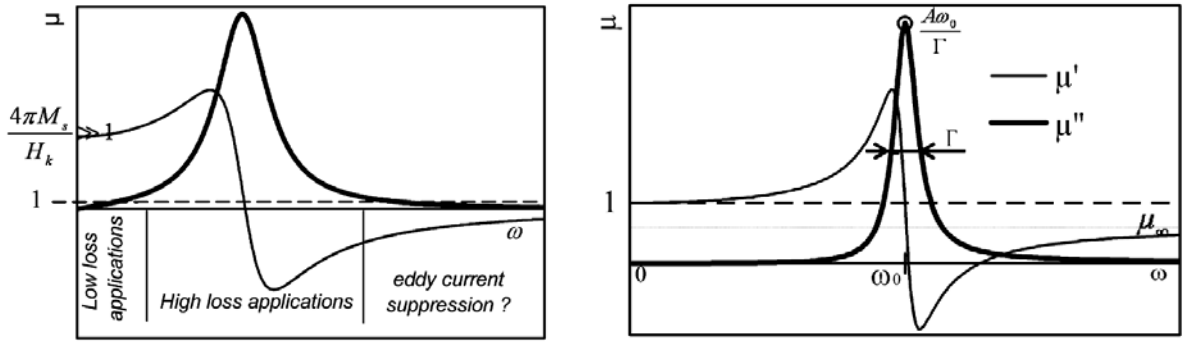

(a) (b)

Figure 1.11: Comparaison between the magnetic permeability exhibited by a conventional magnetic-material and that exhibited by a metamaterial based on non-magnetic materials, as reported by (Acher, 2009).

The region of the magnetic function located below the resonant frequency is very useful for low-losses applications, while the zone of the permeability around the resonant frequency is more appropriate for high loss applications. Beyond this latter spectral region, the real part of the permeability is less than unity (and even negative in a part of the curve) with low-loss level. This spectral region is very promising since its offers the possibility to reduce the skin effect in classical conductors (Amiri, 2007).

Since most common applications based on conventional magnetic materials require high levels of permeability, this latter seems thus to be a good criterion, which allows comparing performances of both metamaterials and standard magnetic materials. The typical effective permeability of a metamaterial is depicted in figure 1.11(b). Below the magnetic resonant frequency, the real part of permeability tends to unity $\mu_0=1$ (Lagarkov, 2009). Beyond the resonant magnetic frequency, the incident electromagnetic field is shielded by metallic patterns, the inclusions exhibit a diamagnetic behaviour: $\boldsymbol{\mu}$ is negative and the generated magnetic induction $\boldsymbol{B} = \boldsymbol{\mu H}$ is opposite to the incident magnetic field $\boldsymbol{H}$. At high frequencies, the permeability $\boldsymbol{\mu_\infty}$ lies between 0 and 1. Below the magnetic

resonant frequency, traditional magnetic-materials exhibit an extremely large level of permeability (μ_0 ~10^3), unlike metamaterials, which exhibit a high level of permeability (few dozen only) around the resonant magnetic frequency. In conclusion, it has been demonstrated that conventional magnetic materials remain more efficient than metamaterials, when high levels of permeabilities are desired, and for an operating frequency below 10 GHz approximately (Acher, 2009). However, at high frequencies, metamaterials can exhibit levels of $\boldsymbol{\mu}$ and spectral bandwidth, exceeding largely what can be reached by traditional magnetic materials.

c. Negative Refractive Index Metamaterials

In 2001, R. A. Shelby et al (Shelby, 2001) have experimentally demonstrated that negative refractive index is possible. The authors were inspired from the theoretical works of J. B, Pendry et al (Pendry, 1998, Pendry, 1999) and proposed a structure, which combines such continuous wires and SRRs elements, as depicted in figure 1.12(a). Using an appropriate polarization of the incident electromagnetic wave ($\boldsymbol{E}$ // continuous wires and $\boldsymbol{H}$ ⊥ SRRs planes), both electric and magnetic activities are simultaneously reached at the targeted frequency. This gives rise to negative permittivity, negative permeability and thus to negative refractive index.

Figure 1.12(b) shows the experimental setup (based on a micro-structured prism) used by the authors in order to demonstrate the negative refraction effect. Subsequently, a large variety of metallic patterns have been proposed in order to obtain the desired electromagnetic properties, such as: Ω-shaped structures (Huangfu, 2004), U-shaped structures (Enkrich, 2005), staplelike structures (Zhang, 2005), paired rods (Shalaev, 2005). At very high frequencies, when we deal with these kinds of structures, two main difficulties should be taken into account.

(a)

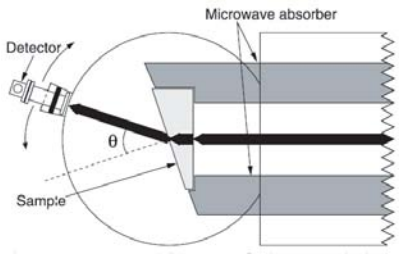

(b)

Figure 1.12: (a) The negative refractive index structure of R. A. Shelby et al (Shelby, 2001), (b) experimental setup used by the authors to demonstrate the negative refraction effect.

From the technological point of view, it is very difficult, or even virtually impossible to fabricate unit cells of complex geometry with submicron or nanoscale sizes. Another limitation related to the scaling law should be also taken into account. Indeed, concerning structures that exhibit a negative effective permittivity, it is possible to shift the plasma frequency in the mid-infrared range, by

modifying the thickness and the concentration of metallic wires. However, beyond this frequency range, the medium is not sufficiently diluted and the behavior of the structure is affected by diffraction effects. Concerning structures with magnetic activity, the increase in frequency can not only performed simply by reducing geometrical dimensions, several physical contribution effects related to the effective mass of electrons and energy absorption should be taken into account, as pointed out by S. O'Brien et al (O'Brien, 2002) who proposed a structure exhibiting a magnetic activity at infrared frequencies.

Fishnet metamaterials (Dolling, 2006) that will be discussed in great details at microwave and terahertz frequency ranges in chapter 3 and chapter 4, respectively have been proposed as an alternative to overcome some difficulties imposed by reducing geometrical dimensions and inertial properties of electrons. Fishnet metamaterials are very simple to fabricate, moreover one single layer illuminated at normal incidence is sufficient to exhibit a negative refractive index at the desired frequency.

1.6.2 All Dielectric Metamaterials

The operating principle of this class of metamaterials is based on Mie theory. They are considered as dielectric resonators, by analogy to metal resonators mentioned above and they can adopt different shapes such as: spheres, cubes, rods …etc. Once exposed to an incident plane wave with an appropriate polarization, resonant modes can occur within each particle. Using dielectrics with high relative permittivity, where effective wavelengths are considerably reduced; the excitation wavelength becomes very large compared to the size of resonators. The definition of an effective medium could be applied (Lagarkov, 2003, Vendik, 2004). This class of metamaterials will be discussed in great details in chapter 4.

1.6.3 Transmission Lines Based Metamaterials

It is well known that composite metal-dielectric metamaterials, can be described as an array of ***LC*** resonant circuits generating fields in response to an incident excitation wave. Eleftheriades et al in their works (Grbic, 2002, Iyer, 2003, Grbic, 2003, Eleftheriades, 2003) proposed a new approach to design negative refractive index metamaterials, which consists to integrate periodically localized circuit elements (inductances, and capacitances) on a microstrip propagation line. Using the basis of transmission line theory, and taking into account the distributed model of the conventional transmission line the inductance ***L*** and the capacitance ***C*** can be connected to the magnetic permeability μ and the electric permittivity ε, respectively. If we consider now a dual transmission line of length Δz, as depicted in figure 1.13, the propagating constant β can be expressed as follows (Caloz, 2004):

$$\beta = -\frac{1}{\omega\sqrt{LC}\Delta z}, \tag{1.62}$$

The phase velocity $\boldsymbol{v_\varphi}$ and the group velocity $\boldsymbol{v_g}$ are anti-parallel according to equations (1.66) and (1.67), given below:

$$v_\varphi = \frac{\omega}{\beta} = -\omega^2\sqrt{LC}\Delta z < 0, \tag{1.63}$$

$$v_g = \frac{\partial\omega}{\partial\beta} = \omega^2\sqrt{LC}\Delta z > 0, \tag{1.64}$$

A negative refractive index can be defined for this structure:

$$n = \frac{c}{v_\varphi} = -\frac{1}{\omega^2\sqrt{LC}\sqrt{\varepsilon_0\mu_0}\Delta z}, \tag{1.65}$$

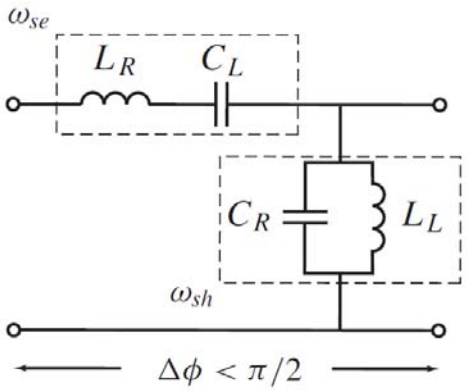

Figure 1.13: Unit cell of a composite right/left-handed (CRLH) transmission line (TL) prototype according to (Caloz, 2004), $\boldsymbol{\omega_{se}}$ and $\boldsymbol{\omega_{sh}}$ are the series and the shunt frequencies, respectively.

This structure supports backward waves, experimental prototypes has been proposed in order to demonstrate this negative refraction effect (*advance phase transmission line*) at microwave and terahertz frequency range, respectively (Eleftheriades, 2002, Caloz, 2004, Crépin, 2005). At first glance, one can think that the terminology "metamaterial" is not appropriate to these structures, since we deal in reality with microwaves transmission media loaded with localized ***LC*** elements. However, considering these structures as effective media leads to very interesting applications. Indeed, a super-resolution effect has been demonstrated using 2D and 3D loaded microstrip lines (Eleftheriades, 2002, Grbic, 2005, Alitalo, 2006) and figure 1.14 shows the experimental prototype, which has been used to this aim, according to (Grbic, 2005).

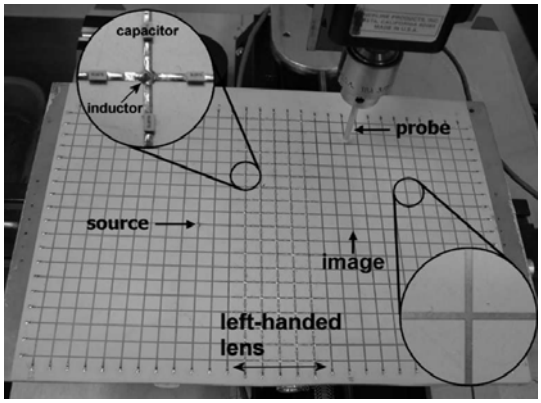

Figure 1.14: Experimental dual transmission line lens, according to (Grbic, 2005).

1.6.4 Photonic Crystals, a Particular Case

Photonic crystals are dielectric or metallic periodic structures in which diffractions effects occur, leading to Electromagnetic Band Gaps (EBGs) that are exploited with the aim to modify the propagation of electromagnetic waves. Once exposed to an incident plane wave at a frequency located in a band gap, reflections within the photonic crystal are destructive and this later acts as a high quality reflector. This property is already available as a commercial application in the optimization of optical fiber sheaths (Russell, 2003). Although these structures are used in the Bragg regime, i.e. for periodicities of the same order as the wavelength, it has been demonstrated that they can be used as a homogenous materials, giving rise to an effective negative refractive index (Enoch, 2003).

1.7 Superlens, a Promising Application of Metamaterials

One of the most spectacular applications of metamaterials is probably the superlens or the perfect lens. J. B. Pendry has already demonstrated that the propagation of electromagnetic wave in a left handed material is accompanied by an inversion of phase for propagating components and by an amplification of evanescent modes (Pendry, 2000). This result is particularly very interesting, since it offers the possibility to restore a perfect image of an object. In a classical lens, the focusing process is achieved due to the refraction of the beam on the curved shape of the lens, however in a superlens, the focusing is made possible by the negative refractive index.

If the lens is sufficiently thick, a first focal point can appear within the flat-lens, which is not very useful, but a second focal point occurs outside the lens. A superlens made of metamaterial can have a plane shape, which enables eliminating totally the spherical aberrations produced by a standard lens. Spherical aberrations in a biconcave lens give rise to a blurred image because the shape of the lens is not optimal, in other words: the light that passing at the edge of the lens does not have the same focal point, as the one that passing near the center of the lens. A superlens can reach a resolution, which is much larger than that limited by the classical diffraction limit. This later implies that it is impossible to

obtain a clear image of an active or passive source, which is much smaller than the working wavelength. The part of the wave containing the necessary information to obtain this resolution is dissipated rapidly, a superlens allows amplifying these parts of the wave, which offers the possibility to image sources much smaller than the wavelength of the light used. The superlens effect has been succesfully demonstrated in scientific literature (Fang, 2005, Liu, 2007). A better level of resolution can be at the origin of huge number of applications. Indeed, it would be possible to improve the storage capacity of optical discs (CD, DVD …etc) since we could etch more finely on the disc. In the field of microscopy, we would be able to observe in visible light very small objects, such as mitochondria in cells. A superlens is characterized by two main properties: perfect focusing effect and amplification of evanescent modes.

1.7.1 Focusing by a LHM-Based Flat Lens

Consider a LH slab sandwiched between two RH media, also called a "LH-lens". By applying Snell's law [Eq. (1.66)] twice to the sytem, we obtain the ***double focusing effect*** depicted in figure 1.15.

$$n_R \sin\theta_R = n_L \sin\theta_L, \tag{1.66}$$

Two radiated rays with equal symmetric angles from a source at the distance $\boldsymbol{l}$ from the first interface are negatively refracted under an angle of same magnitude to meet at a distance $\boldsymbol{s}$ in the slab; then they focus again after a second negative refraction in the second RH medium at the distance $\boldsymbol{d - l}$ from the second interface, where $\boldsymbol{s}$ is obtained by simple trigonometric considerations as:

$$s = l\frac{\tan\theta_R}{\tan\theta_L}, \tag{1.67}$$

where the angle $\boldsymbol{\theta_R}$ is the incidence angle and $\boldsymbol{\theta_L}$ is obtained by Snell's law [Eq. (1.66)], $\boldsymbol{\theta_L} = -\sin{-1}[(\boldsymbol{n_R}/\boldsymbol{n_L})\sin\boldsymbol{\theta_R}]$.

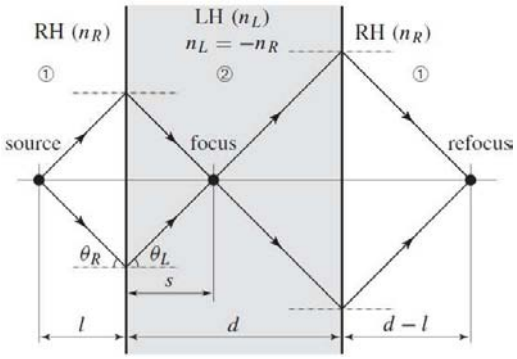

Figure 1.15: Illutration of the double focusing effect in a "flat-lens" as reported by (Caloz, 2006), which is a LH slab of thickness $\boldsymbol{d}$ and refractive index $\boldsymbol{n_L}$ sandwiched between two RH media of refractive index $\boldsymbol{n_R}$ with $\boldsymbol{n_L} = -\boldsymbol{n_R}$.

Formula (1.67) shows that if the two media have the same electromagnetic density, i.e. refractive indexes of same magnitude ($n_L = -n_R$), focus is obtained at the mirror image of the source, $s = l$, since $|\theta_L| = \theta_R$ from Snell's law.

1.7.2 Amplification of Evanescent Modes

If we consider an evanescent mode that propagates along the positive z axis, one can write the following expression:

$$A_{air}(z) = A_0 \exp(-\alpha z), \tag{1.68}$$

where A_0 is the amplitude and α the attenuation coefficient, $\alpha > 0$. The component of the wave increases exponentially within the superlens where $n = -1$, as depicted in figure 1.16. Equation (1.68) becomes:

$$A_{NRIM}(z) = A_0 \exp(-n\alpha z) = A_0 \exp(\alpha z), \tag{1.69}$$

The evanescent mode is amplified and the image of the original object is reproduced with a perfect resolution.

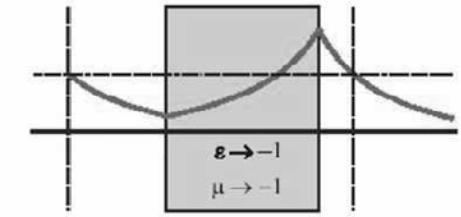

Figure 1.16: Amplification of evanescent modes in a superlens.

1.8 Conclusion

In conclusion, a general overview about fundamental properties of materials with negative refractive index has been exposed. We have presented a series of metamaterials proposed over the last few years in order to obtain desired electromagnetic properties. We have seen that a metamaterial with subwavelength features can be represented as an effective medium characterized by effective constitutive (μ_{eff}, ε_{eff}) and propagative (z_{eff}, n_{eff}) parameters. The retrieval method used in our research has been discussed and a particular attention has been focused on choosing appropriate signs of effective parameters. The superlens, considered as a promising application of metamaterials has been illustrated at the end of this chapter.

Chapter 2

Non-Destructive Measurements: Free Space Microwave Setup and Terahertz Time Domain Spectroscopy

2.1 Introduction

Electromagnetic waves are considered as the most efficient tool that can be used to observe, analyze and understand our environment. The electromagnetic spectrum is divided into different frequency (wavelength) regions. The extent of the electromagnetic spectrum allows observing a huge variety of physical phenomena. The frequency regions that have been targeted in our research are microwaves and terahertz, respectively. Terahertz regime, which extends from few hundreds of gigahertz to a few terahertz between microwave and optical frequencies (figure 2.1) remained inaccessible for long time due to the absence of appropriate emitters and detectors. Recently, the advances in semiconductors technology, have given rise to inexpensive sources and detectors operating at terahertz regime, which constitutes a breakthrough for many applications.

By its position between optics and microwave, terahertz regime is considered as a multidisciplinary domain leading to promising applications. Indeed, terahertz radiation is a non-ionizing radiation and shares with microwaves the capability to penetrate a wide variety of non-conducting materials without causing any damages. Terahertz radiation can pass through clothing, paper, cardboard, wood, masonry, plastic and ceramics for example. It can also penetrate fog and clouds, but cannot penetrate into metal or water.

In this present chapter, we will focus on different elements constituting experimental setups that have been used in our research in order to carry out measurements at microwave and terahertz frequency ranges. We have used both a non-destructive free space setup based on Vector Network Analyzer (VNA) and horn antennas (AB millimeter) at microwave frequencies (20GHz–110GHz), and terahertz time domain Spectroscopy (THz-TDS) at terahertz frequency range (0.1THz-3THz). But first, we will present briefly the numerical tools that have been used in order to predict the electromagnetic behavior of our samples.

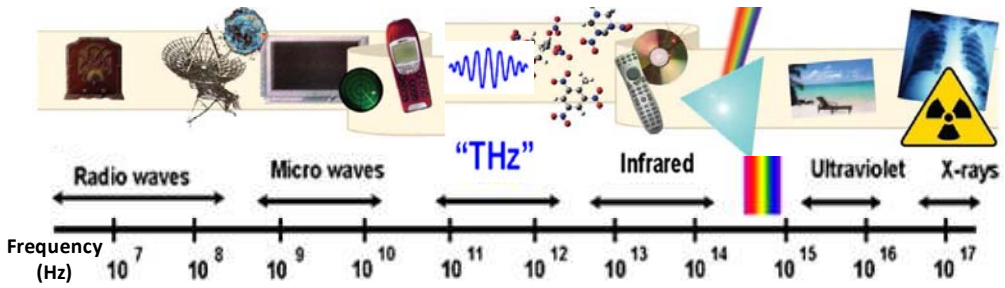

Figure 2.1: The Electromagnetic spectrum organized in different portions according to the corresponding frequency ranges.

2.2 Numerical Calculation Methods

Numerical solution of EM problems started in the mid-1960s with the availability of modern high-speed computers. Since then, considerable efforts have been expended on solving complex EM-related

problems for which closed form analytical solutions are either intractable or do not exist. Based on Maxwell's equations, each numerical method has its own unique advantages and disadvantages for specific needs. These methods serve as means to present the fundamentals of applying EM theory to the analysis of boundary-value problems. The study of metamaterials requires a priori an electromagnetic modeling work before any experimental prototyping, in order to predict the behavior, i.e. the spectral response of the investigated structures. Nowadays, a wide variety of dynamic and full wave approaches of calculations are available such as: Finite Difference Time Domain (FDTD), Finite Element Method (FEM), Transmission Line Matrix (TLM) and so on. The commercial calculators that we have used in our research: HFSS and CST-MICROSTRIPES are based on FEM and TLM methods, respectively. In this section we will briefly discuss about these two aforementioned methods.

2.2.1 Finite Element Method (FEM)

The finite element method originated from the need for solving complex elasticity and structural analysis problems in civil and aeronautical engineering. Its development can be traced back to the work by Alexander Hrennikoff and Richard Courant in the 40's (Courant, 1943). Few years later, it was introduced in electromagnetism science to solve Maxwell's equations. It is considered as a mathematical tool that solves in a discrete way and in a frequency domain Partial Differential Equations (PDEs). Basically, the equation concerns a specific function defined on a domain and characterized by boundary conditions, which ensures the existence and uniqueness of the solution. The finite element method is based on a division of the considered space generally in a tetrahedral mesh, which easily adapts to complex structures. The shape of the mesh can be modified depending on the geometry of the domain in order to mesh more finely some regions than others (figure 2.2). The resolution of partial differential equations cannot be performed directly in the mesh, it should be written in the variational form, which includes information about the PDE and boundary conditions.

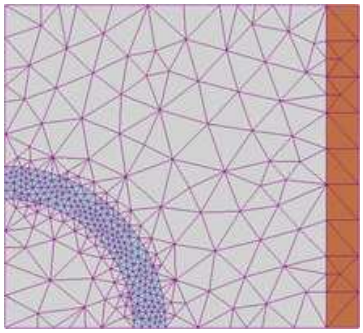

Figure 2.2: Example of adaptative mesh used by HFSS.

More details about the FEM can be found in the book of J. C. Sabonnadière and J. L. Coulomb (Sabonnadière, 1996). The software simulator that we have used in our calculations is HFSS, it is

commercialized by ANSOFT society and offers the possibility to solve propagative systems by solving the Maxwell equation given below at frequency domain:

$$\nabla\times\left[\frac{1}{\mu_r}\nabla\times E(\omega)\right]-k_0^2\varepsilon_r E(\omega)=0, \tag{2.1}$$

2.2.2 Transmission-Line Matrix Method (TLM)

Transmission line matrix method solves Maxwell equations in time domain. The basic principle of this method is based on the analogy between the propagation of electromagnetic waves in a medium and the propagation of voltages and currents, due to the similarity between Maxwell equations and the telegraph equation, in transmission lines. For a given electromagnetic system, the computational domain is filled with a transmission lines network and the calculated electric and magnetic fields are given as a function of voltages and currents. For each step time, the voltage pulses that arrive on each node of the transmission line are scattered in order to produce a series of new pulses that become incident on adjacent nodes during the next step time. The relationship between incident and scattered pulses is determined by the diffusion matrix, which must be compatible with Maxwell equations. Figure 2.3 shows a simple example of a 2D TLM mesh with 1V amplitude incident voltage pulse on the central node. This pulse will be partially reflected and transmitted according to the transmission line theory. If we assume that each line has a characteristic impedance ***Z***, then the incident pulse sees effectively three transmission lines in parallel with a total impedance of ***Z*** / 3. The reflection coefficient and the transmission coefficient are given by:

$$R=\frac{\frac{Z}{3}-Z}{\frac{Z}{3}+Z}=-0.5, \tag{2.2}$$

$$T=\frac{2\times\frac{Z}{3}}{\frac{Z}{3}+Z}=+0.5, \tag{2.3}$$

CST-Microstripes is a commercial software simulator based on TLM method, and unlike HFSS, the mesh in this case is based on rectangular elements.

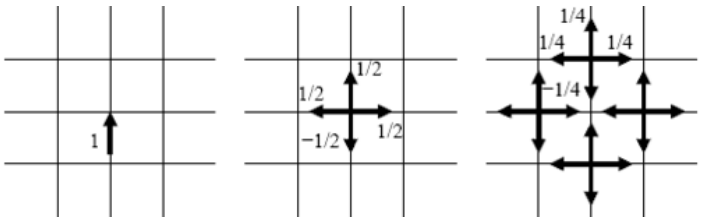

Figure 2.3: 2D TLM example: an incident voltage pulse in two consecutive scattering events.

Further electromagnetic numerical methods (not presented here) are various and widely discussed and used in scientific literature such as: Variational Methods (VM), Spectral Domain Method (SDM), Mode-Matching Method (MMM), Method of Moments (MOM), Method of Lines (MOL) and Artificial Neural Networks (ANN). See (Yagoub, 2007) and references therein, the authors present a survey of existing electromagnetic techniques, highlighting their main specific advantages and disadvantages for a circuit designer.

2.3 Free Space Measurement setup (ABmm) at Microwave Range

In this section we will describe the non destructive quasi optical free space setup that we have used (see figure 2.4 (a)) in order to carry out experiments at microwave frequencies from 18 GHz to 110 GHz. It is based on an AB-MillimetreTM Quasi-optical Vector Network Analyzer (MVNA 8-350-2) with simultaneously 2 receiving channels (reflection and transmission). New versions of this analyzer are available and can reach an operating frequency of about 1THz. Our setup is equipped with four pairs of millimeter heads, scanning the following frequency ranges: 18-26 GHz, 29-51 GHz, 42-72 GHz and 70-110 GHz.

Theses frequencies are obtained from a 8-18 GHz source looking frequency counter, the output signal is directed by SMA coaxial cables to frequency multipliers (Harmonic Generator) in order to obtain the aforementioned frequency ranges. These multipliers are connected to horn antennas by coax-waveguides transitions. The signal propagates in free space in the form of Gaussian beam and samples are placed in the beam waist, where the beam is focused. The signal transmitted by the sample is collected by a receiving horn antenna and a harmonic detector (Harmonic Mixer). The reflected signal is recovered by a coupler, and then transmitted by waveguide to a harmonic detector. A computer controls all the system and allows recovering data using acquisition cards, an oscilloscope displays in real time the magnitude and the phase of the detected signal.

Since the signal is propagating in free space, we should adapt the wave-guided impedance to the impedance of free space. To this aim, we use a pairs of pyramidal horn antennas in the frequency band, which extends from 18 GHz to 26 GHz and a series of scalar corrugated conical horn antennas for other frequency regions as illustrated in table 2.1. This type of corrugated horn antennas has a radiating pattern with a rotational symmetry, and the Gaussian beam is obtained by coupling different modes. The basic principle consists to convert a part of the energy of $\boldsymbol{TE_{11}}$ mode coming from circular waveguide into $\boldsymbol{TM_{11}}$ mode and then combined together with the appropriate phase relation in order to produce hybrid mode $\boldsymbol{HE_{11}}$. The $\boldsymbol{TE_{11}}$ mode is obtained from $\boldsymbol{TE_{01}}$ by a transition "rectangular waveguide – circular waveguide", which contributes to the impedance matching. The $\boldsymbol{TM_{11}}$ mode is

generated by the corrugations, which impose identical boundary conditions for the two polarizations of the electric field. The amplitude of the beam has a Gaussian variation when we move far away from the axis of the horn. The wavefront of a Gaussian beam is plane at the waist and curved in the rest of the propagation axis, the sample is placed in the waist where the wavefronts are plane. More details can be found about antenna theory in the book of C. A. Balanis (Balanis, 1997).

(a)

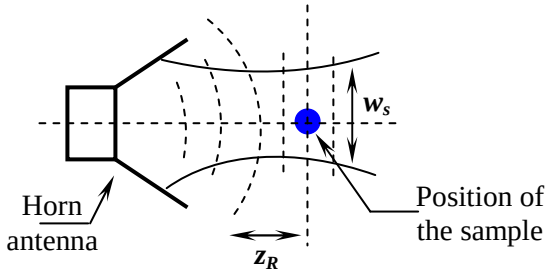

(b)

Figure 2.4: (a) Real images of our experimental quasi optical free space microwave setup, (b) schematic of the microwave horn used, the setup is completed by the mirror image to receive the transmitted signal through the sample

Frequency band	Type of horn	Aperture (cm)	Length (cm)
18-26 GHz	Pyramidal	2.9	5.5
29-51 GHz	Conical	5	24.2
42-72 GHz	Conical	3.1	18
70-110 GHz	Conical	2.5	12

Table 2.1: Dimensions of horn antennas depending on the targeted frequency region

With a quasi-optical focalized setup, it is not necessary to use an anechoic chamber in order to carry out measurements. However, parasitic reflections between the sample and the surrounding environment can considerably reduce the accuracy of the measurements. Preliminary measurements carried out in air for the transmission and on a metallic plane located at the waist position enable to calibrate the experimental setup. Reflections due to the surrounding environment are then suppressed.

To approximate a plane wave, there are two requirements. First, to ensure that the field amplitude is uniform over the samples, the beam waist at the sample w_s must be much larger than the transverse extent of the sample. Second, to ensure that the wavefronts are planar, the Rayleigh range z_R must be much larger than the longitudinal extent of the sample. The beam waist at the sample plane is w_{s1} ~ 4.4 cm for the 29-51 GHz frequency range and is w_{s2} ~ 2.2 cm for the 70-110 GHz frequency range, approximately. The corresponding Rayleigh ranges ($z_R = \pi.w^2_s/\lambda$, where λ is the centre wavelength of the working frequency band) for each frequency range at the sample are: z_{R1} = 13 cm and z_{R2} = 10 cm, approximately (Oyhenart, 2005).

One can see that w_{s1} and w_{s2} are of the same order of the aperatures dimensions of the conical horns (see table 2.1 given above) leading thus to a weak focusing. Indeed, the conical horns are long enough, about 24 cm and 12 cm, respectively to prevent the systematic divergence of the beam at the output of the horn. A good approximation to a plane wave is ensured because the latter two dimensions are indeed much larger than the samples that will be studied in chapter 3. In other words the number of unit cells illuminated at the position of the beam waist is rather enough. Indeed, about 12×12 unit cells (lattice periodicities: $a \times b$ = 3mm × 4mm and 3.6mm × 3.6mm, respectively) are spatially covered by the beam waist for the 29-51 GHz frequency range, and about 10×10 unit cells (lattice periodicity a = 2.5mm) for the 70-110 GHz frequency range.

2.4 Terahertz Frequency Regime

Terahertz frequency region has been explored intensively since about two decades due to the development of ultrafast lasers, which are able to produce optical pulses substantially shorter than 1ps. Terahertz time domain spectroscopy (THz-TDS) is considered as an optoelectronic method of measurement, exploiting the wide band spectrum associated to ultra-short laser pulses. Terahertz radiation covers a frequency band, where located vibration energies of many molecules such as Hydrogen Fluoride HF (1.23 THz) and Hydrochloric Acid HCl (1.25 THz). These spectral signatures of molecules in the far-infrared and terahertz regions are widely exploited in order to probe the internal composition of molecular clouds (Mittelman, 2003). THz-TDS also find applications in medical imaging. Indeed, due the low energy of a terahertz radiation (1 THz = 4.1meV), and since it is absorbed by water molecules, it is therefore possible to differentiate biological tissues due to the

contrast induced by the local concentration of water. The field of security imaging has also benefited from the contribution of terahertz radiations, since they offer the possibility to image sequentially hidden objects. For example, viewing objects that are inserted in a package optically opaque, or more recently millimeter imagers available in some airports making possible the detection of hidden objects (Karpowtrc 2005). Another application field is high-altitude telecommunications, above altitudes where water vapor causes signal absorption: aircraft to satellite, or satellite to satellite.

Terahertz (THz) spectroscopy, and especially THz imaging, holds large potential in the field of nondestructive, contact-free testing. The ongoing advances in the development of THz systems, as well as the appearance of the first related commercial products, indicate that large-scale market introduction of THz systems is rapidly approaching. Industrial applications for THz systems, comprising inline monitoring of compounding processes, plastic weld joint inspection, birefringence analysis of fiber-reinforced components, water distribution monitoring in polymers and plants, as well as quality inspection of food products employing both continuous wave and pulsed THz systems is already used (Jansen, 2010). In this section, we will briefly give the most commonly used optical terahertz radiating sources.

a- Terahertz Diodes

We call terahertz diodes all active electronic dipoles enable emitting millimeter and submillimeter radiations. In these semiconductors-based components, we observe in the characteristic current-voltage a decrease of the current when the bias voltage increases. This effect commonly called Negative Differential Resistance (NDR) is suitable to the generation of electrical oscillations. Gunn diode (Hu, 2010) for example, is based on a simple bar of gallium arsenide (GaAs), which exploits a physical property of the substrate: electrons move with different velocities due to their different effective masses after transfert in sattelite valley.

There are several local minima of energy that exist in the conduction band, depending on the displacement of electrons. The current then propagates as a burst of electrons, which means that a direct current gives rise to an alternative current. This phenomenon can be used to realize microwave oscillators, their frequencies can be controlled by the dimensions of GaAs and by the physical characteristics of the resonator in which the diode is placed. For example, a Gunn diode operating at 100 GHz can generate 250 mW, but a Gunn diode functioning at 300GHz causes a decrease of the power to 300µW. Currently, Gunn diodes are able to reach 100GHz with a power close to 200 mW. Other examples such as IMPATT diodes (IMPpact Avalanche Transit Time) (Eisele, 1998) and RTD diodes (Resonant Tunneling Diode) (Brown, 1991) representing NDRs but exploiting different principles are also used as terahertz sources. IMPATT diodes belong to the category of injections and time transit diodes, they use the avalanche effect to generate charge carriers and can reach more than

1Watt at 100 GHz, but the output power collapses dramatically beyond this limit. RTD diodes are considered as solid oscillators functioning in the millimetre band that exploit quantum effects in a double hetero-junction. This category of diodes has a lower emitting power compared to the aforementioned diodes. The major limitation of electronic diodes is related to the decrease of their generated electromagnetic power depending on the frequency and the small area of these high frequency devices (Eisele, 1998).

b- HEMT (High Electron Mobility Transistor)

High electron mobility transistor is a promising submicron component for the terahertz generation. The operating principle of a HEMT is identical to that of a field effect transistor with a MESFET Schottky gate. It is based on the modulation of the conductance between the source and the drain, under the electrostatic control of the gate. This basic component of the fast electronic can be used as an amplifier in the microwave regime. M. Dyakonov and M. S. Shur (Dyakonov, 1993, Dyakonov, 1996) have proposed a theory about the instability of plasma waves in a bi-dimensional electrons gas, which stipulates that a transistor can function as a terahertz source or detector, for a nanometer size of the grid. Indeed, when an electric current is injected, the HEMT develops instabilities in the electronic plasma under the grid of the nanotransistor.

Beyond certain amplitude of the current the excitation and the acceleration of charges generate a terahertz radiation. Recently, studies have allowed generating a terahertz radiation at room temperature, using nanometer HEMTs. These transistors can produce an output power of about 200 mW at 0.2 THz (Wang, 2001).

c- Backward Wave Oscillator (BWO)

Backward wave oscillators are tubes in which the submillimeter wave is generated by the Smith-Purcell effect (Smith, 1953). The Smith-Purcell effect is obtained when an electron beam propagates with a grazing incidence over a metallic diffraction array. Electrons are emitted with a relative velocity equal to $v_{re} = v / c$. During their displacement, electrons radiate an electromagnetic wave with a frequency $f_e = v_{re}\, c / d$, where d is the spatial frequency of the radiated field. The frequency of the sub-millimeter wave radiated by the BWO can be tuned by modifying the energy of electrons and the structure of the tube. BWOs are considered as coherent, compact and powerful (10 mW) terahertz sources. Table 2.2 illustrates some examples of BWO with their main properties.

Model	OB-24	OB-30	OB-32	OB-80	OB-81	OB-82	OB-83
Operating range, GHz	179-263	258-375	370-535	526-714	667-857	789-968	882-1111
Output power, typ, mW	20-50	10-20	4-15	4-15	4-15	3-10	3-10
Output power*, min, mW	1-10	1-10	1-5	1-5	1-5	1-3	1-3
Power difference in the range, max, dB	13	13	13	13	13	13	13
Magnetic field required**, min, T	0.7	0.8	1	1	1	1	1.1
Anode voltage, kV	1-4	1-4	1-5	1.5-6	1.5-6	1.5-6	1.5-6
Cathode current, mA	25-40	25-40	25-40	30-45	30-45	30-45	30-45

Table 2.2: Some examples of BWOs with their main properties, as reported in the following link: http://www.elva-1.com/products/microwave/bwo-180.html

d- Laser Sources

The first laser source emitting in the terahertz range was the molecular laser (Crocker, 1964). This laser gas is pumped by dioxide carbon (CO_2) lasers. The functioning principle is based on the transitions between rotation levels and vibration levels of the gaseous medium that fills the cavity. The best-known active media are methanol (CH_3OH) and formic acid (HCOOH). This source operates at discrete frequencies imposed by the gas introduced in the cavity, and can provide an output power of about some mW.

e- Quantum Cascade Laser (QCL)

A quantum cascade laser is based on a stack of ultrathin layers forming hetero-structures of semiconductor materials. Unlike semiconductor lasers, based on transitions between conduction and valence bands, the originality of QCLs lies in the use of inter-sub-band transitions in the conduction band (Barbieri, 2000). The first demonstration of QCLs operating in the terahertz range has been performed by J. Faist and his collaborators in 1994. In 2002, Kholer (Kholer, 2001) has shown the possibility for these lasers to radiate in the terahertz regime at 50 ***K*** and the next challenge is to radiate at room temperature. The record temperature that has been reached is 169 ***K*** in pulsed mode with an output power of about 250 mW and 117 ***K*** in continuous mode with 130 mW of power (Williams, 2005).

2.5 Generation of THz Field

After this overview about optoelectronic emitting terahertz devices, we will discuss in the following sections about different physical phenomena involved in the generation and the detection of terahertz radiations. Basically, four main optoelectronic techniques are used to this aim: surface effect (Greene, 1992, Zhang, 1992), non-linear processes generation (Yang, 1971), photoconduction effect (Auston, 1984) and beat frequency (Evenson, 1984, Brown, 1995).

2.5.1 Generation by Surface Effect

One of the simplest methods used to generate terahertz signal is the surface effect emission. It basically consists in illuminating the surface of a semiconductor material (GaAs, InP, InAs, …) by an impulse (ultra-short) laser. No technological fabricating steps are required for this kind of technique. The generated terahertz field radiates in two directions. The first direction is almost collinear to the reflexion of the optical beam and the second direction depends on the transmission properties of the material. Since the propagation of terahertz pulse is limited from the point of view of the divergence, we can deduce from the Snell's law the angles defining the emission directions of terahertz field as a function of the incident angle of the optical beam (Zhang, 1990):

$$n_{air}(\omega_{laser})\sin\theta_{laser} = n_{air}(\omega_{THz})\sin\theta_{R-THz} = n_{SC}(\omega_{THz})\sin\theta_{T-THz} \quad (2.4)$$

where $\boldsymbol{\theta_{laser}}$, $\boldsymbol{\theta_{R\text{-}THz}}$, $\boldsymbol{\theta_{T\text{-}THz}}$ and $\boldsymbol{n_{SC}}$ are the incident angle of the laser beam, the direction of the reflected terahertz beam, the direction of the transmitted terahertz beam and the refractive index of the semiconductor in the THz frequency band.

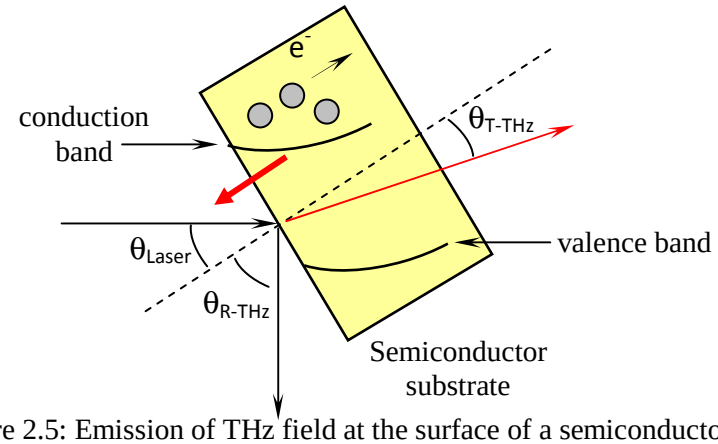

Figure 2.5: Emission of THz field at the surface of a semiconductor.

Two main physical phenomena are responsible for this electromagnetic emission: the acceleration by surface field (Greene, 1992), and the Photo-Dember effect (Dekorsy, 1995). The generation of THz field by surface emission effect has been performed using various semiconductor materials: InAs (Sarukura, 1995, Adomavicius, 2004), InP (Zhang, 1990, Nakajima, 2003) GaAs (Kersting, 1998), GaSb (Winnerl, 2004, InSb (Kono, 2000). Basically, the conduction and the valence bands are curved near the surface of the semiconductor as illustrated in figure 2.5, due to the superficial defaults that induce a spatial charge distribution at the surface of the semiconductor (symmetry breaking between the air and the semiconductor).

This gives rise to a native residual electric field $\boldsymbol{E_{surf}}$, normal to the surface and penetrating the semiconductor. When this latter is illuminated by a laser, the photo-generated charge carriers are accelerated by the residual field. The resulting photo-induced current generates an electromagnetic THz radiation as in the case of a Hertz dipole. Since the Hertz dipole is normal to the surface of the

semiconductor substrate, this latter must be inclined with respect to the direction of the propagation of THz waves (in other words the SC-crystal is illuminated at oblique incidence). The characteristics of the radiated THz field strongly depend on the properties of the material used. The expression of the surface static electric field can be written as follows (Robertson, 1995):

$$E_{surf}(z) = \frac{eN_D}{\varepsilon_0 \varepsilon_r}(W - z), \tag{2.5}$$

where W is the width of the depletion region created at the surface, which depends of the doping of the substrate and the electrical potential associated to the curvature of the bands (conduction and valence). The expression of the current density created by the surface field can be written as follows (Zhang, 1990):

$$J_{surf}(t) = \frac{e\alpha}{\hbar\omega}[1 - R(\theta)]\int_0^W \mu E_{surf}(z) e^{-\alpha z} dz \int_{-\infty}^{t} e^{-\frac{t-t'}{\tau}} I_0(t') dt', \tag{2.6}$$

where α is the absorption coefficient, at the considered wavelength, μ is the mobility of carriers, τ is the life time of free carriers in the depletion region, $I_0(t)$ is the temporal profile of the optical pulse excitation and $R(\theta)$ is the reflection coefficient of the optical incident beam at the surface of the semiconductor. In the case of the Dember effect, based on diffusion velocities of the photo-generated carriers, the expression of the created electric field can be written as follows (Ascázubi, 2005):

$$E_D = \frac{KT_e}{e} \frac{b\frac{\partial \Delta n}{\partial z}}{p + nb + \Delta n(1+b)}, \tag{2.7}$$

where b is the ratio between the mobility of electrons and the mobility of holes, n and p are the concentrations of the intrinsic carriers, Δn is the concentration of the photo-generated electron-hole pairs, T_e is the equivalent temperature of plasma related to the excess of energy transmitted to the carriers by photons. Numerical simulations performed using GaSb (Gu, 2000) have predicted values of E_D varying from 100 to 4000 kV/m.

Lastly, non-linear optical processes resulting in THz radiation emission are bulk or surface-field induced optical rectification of incident femtosecond laser pulses. The amplitude of a THz radiation pulse generated by optical rectification in a non-linear optical crystal depends on the following parameters: (1) amount of optical laser radiation transmitted into the crystal, (2) crystallographic orientation of the crystal, (3) the non-linear electric susceptibility of the crystal, and (4) microcrystal grain size. The amount of laser radiation transmitted into the crystal depends on the index of refraction. The magnitude of THz generation due to surface-field induced optical rectification is determined by the third order non-linear electric susceptibility of the material and THz generation due

to bulk optical rectification depends on the second-order non-linear electric susceptibility (Reid, 2005).

2.5.2 Generation by Optical Rectification

This technique (Zhang, 1992) is based on second order nonlinear effects that occur in some nonlinear dielectric crystals such as DAST (Schneider, 2006) and ZnTe, under optical excitation. The main idea here consists in substracting the energy of two photons; we obtain a local and static polarization, which lasts only the time of the optical illumination. The generation of THz radiation by optical rectification requires intense electric fields and sufficiently important (intense pulsed lasers) to induce nonlinear effects. The generated THz pulses obey to Maxwell equations as follows:

$$\Delta E_{THz} - \frac{n^2}{c^2}\frac{\partial^2 E_{THz}}{\partial^2 t} = \mu_0 \frac{\partial^2 P^{(2)}}{\partial^2 t}, \tag{2.8}$$

where $\boldsymbol{P^{(2)} = \varepsilon_0 \chi^{(2)} I_{opt}(t)}$ is the second order polarization, $\boldsymbol{\chi^{(2)}}$ is the second order susceptibility and $\boldsymbol{I_{opt}(t)}$ is the laser intensity. The efficiency of the conversion depends on $\boldsymbol{\chi^{(2)}}$ and also of the condition of matching group velocity (sometimes also called matching phase condition). Indeed, if we consider a Gaussian temporal profile of the pump laser pulse propagating and characterized by the duration $\boldsymbol{\tau_0}$, its spectral intensity can be written as follows:

$$I(\omega) = I_0 \exp\left(-\tau_0^2 \omega^2 / 2\right), \tag{2.9}$$

where $\boldsymbol{\omega}$ is the angular frequency of the radiation, we obtain:

$$P^{(2)}(z,\omega) = \chi^{(2)}(\omega) I(\omega) \exp\left(i\omega z / v_g\right), \tag{2.10}$$

where $\boldsymbol{v_g}$ is the group velocity of the optical pulse, the expression of the THz field, generated in point $\boldsymbol{z}$ of the crystal, can be written as follows (Delagnes, 2010):

$$E_{THz}(z,\omega) = z\omega^2 \chi^{(2)} I(\omega) \sin c \frac{\Delta k_{THz} \cdot z}{2}, \tag{2.11}$$

where $\boldsymbol{\Delta k_{THz} = k_{THz} - \omega / v_g}$ translates the mismatch between the group velocity of the optical pulse and the phase velocity of the terahertz pulse. The total field is the integral along the sample thickness of the local field that has been previously determined. If we neglect the dispersion of the group velocity, the coherence length, which corresponds to the optimal length for the generation process can be expressed as follows:

$$l_c = \pi / \Delta k = \pi c / \left(\omega_{THz} \left| n_{opt} - n_{THz} \right|\right), \tag{2.12}$$

$$l_c = \frac{c}{\omega_{THz} \left| n_{opt} - \lambda_{opt} \left(dn_{opt} / d\lambda\right) - n_{THz} \right|}, \tag{2.13}$$

Depending on the material, and the wavelength of excitation, different dispersion regimes can occur. In practice, very few crystals offer a phase matching in the THz band, due to the significant gap between the optical group velocity and the THz phase velocity. Thus, when we want to generate a broadband spectral region, using an ultra-short laser, the geometrical dimensions of the transmitter and the receiver must be highly reduced down to few microns in term of thickness, in order to preserve the spectral band, which is theoretically accessible by the duration of the laser pulse. Finally another limitation is related to the absorption of these materials in the THz band, which can be very important due to the presence of phonons characterized by frequencies typically located in the THz band. These fundamentals limitations are accompanied by a reduction of the ratio S/N.

2.5.3 Generation by Photoconduction Effect

This technique requires the use of a photoconductive antenna. The device consists of a semiconductor layer on which two metal contacts are deposited. The metallic plots act as electrodes and allow applying a static electric field at the surface of the semiconductor material. When photons of the incident laser beam interact with the semiconductor substrate, pairs of electrons-holes are created (the inter-electrode gap is illuminated by a femtosecond pulse laser with a much larger energy then the energy of the semiconductor gap). The conduction band is then occupied by electrons, while the valence band is filled by holes; the conductivity of the semiconductor is then greatly enhanced. An applied continuous bias voltage $\boldsymbol{V_c}$ across the device allows photocarriers to move. The fast displacement of charge carriers is responsible of the apparition of a brief transient currant $\boldsymbol{j_t}$, which gives rise to a terahertz field radiated by the photoconductive device. A hemispherical silicon lens positioned onto the backside of the wafer collects and allows formatting the terahertz beam. The schematic view of the photoconductive device is shown in figure 2.6. In the case where the antenna's gap is much smaller than the wavelength of emission, the mathematical formalism used to describe the generation of terahertz field is based on equations of charges transport. This model supposes that the THz radiation is generated by temporal variation of the surface density of charges, more precisely by assimilating the photoconductive device to a Hertz dipole. In an isotropic medium characterized by a refractive index $\boldsymbol{n}$, the radiated field at a distance $\boldsymbol{r}$ depends on the dipolar moment $\boldsymbol{P(t)}$ and can be expressed as follows (Born, 1965):

$$E(r,t) \approx \frac{1}{4\pi\varepsilon}\left(\frac{1}{r^3}P(t)+\frac{n}{cr^2}\frac{dP(t)}{dt}+\frac{n^2}{c^2 r}\frac{d^2P(t)}{dt^2}\right), \tag{2.14}$$

The different terms of equation (2.15) represent the static field, the near field and the far field, respectively. We will focus on the far field that varies as $1/\boldsymbol{r}$. The first derivative of the dipolar moment is equal to the product between the photocurrent $\boldsymbol{j_{pc}(t)}$ in the inter-electrodes gap and the length of the dipole. The THz far field is proportional to the first derivative of the photocurrent:

$$E_{THz}(r,t) \approx \frac{l_c}{4\pi\varepsilon c^2 r}\frac{\partial j_{pc}(t)}{\partial t}, \tag{2.15}$$

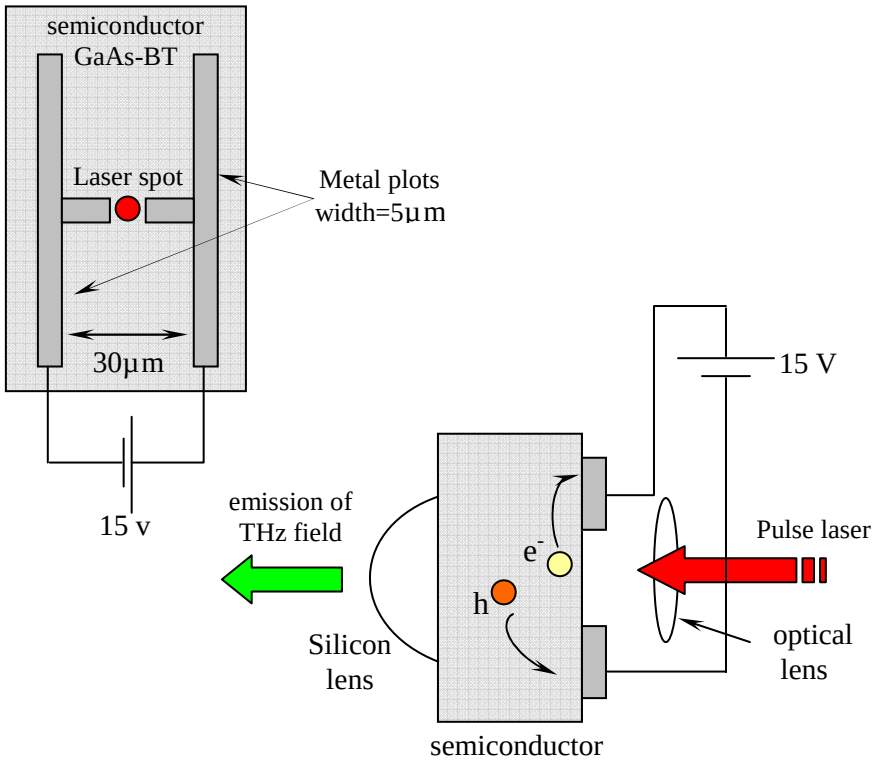

Figure 2.6: Emission of THz field by photoconduction effect.

The photocurrent $\boldsymbol{j_{pc}(t)}$ that flows in the antenna is defined as the convolution product between the optical pulse $\boldsymbol{I_{opt}(t)}$ and the response of the semiconductor substrate (Duvillaret, 2001):

$$j_{pc}(t) \approx I_{opt}(t) \otimes [n(t)qv(t)], \tag{2.16}$$

where $\boldsymbol{n(t)}$, $\boldsymbol{q}$ and $\boldsymbol{v(t)}$ are the carriers density, the electric charge and the displacement velocity of electrons and holes.

2.6 Detection of THz field

2.6.2 Detection by Photoconduction

Photoconduction detectors are identical to emitters of the same type that have been given above in section 2.5.3 except that the device is not connected to a voltage source. The device is illuminated by a pulse laser, creating charge carriers in the semiconductor. If the device is exposed to an incident terahertz pulse, the carriers are accelerated, giving rise to an electric current $\boldsymbol{J_d}$ in the circuit (see figure 2.7). This current is proportional to the amplitude of the terahertz field at the moment of illumination.

In the absence of terahertz pulse, the carriers recombine, and no current is induced. Thus, the detected current is proportional to the convolution product of terahertz and optical pulses:

$$j_d(t) = \int_0^{+\infty} \sigma_s(t-t')E_{THz}(t')dt', \tag{2.17}$$

where, t' is the time delay between the arrival of terahertz field and optical pulse on the detector.

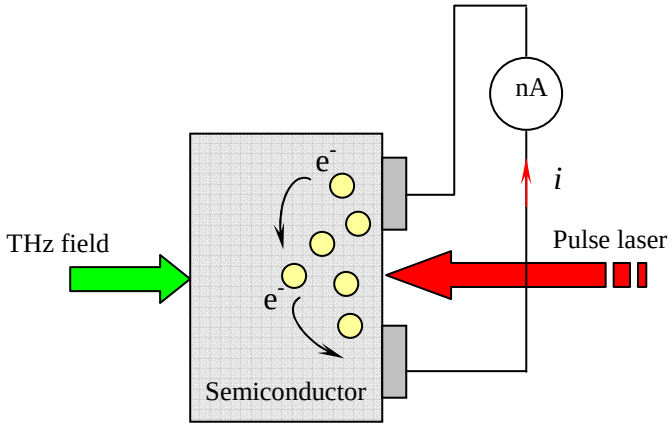

Figure 2.7 : Operating principle of a photoconductive detector

If we consider a lifetime of carriers less than the duration of the optical pulse, the surface conductivity can be expressed as follows:

$$\sigma_s(t) = \sigma_0 \delta(t-t'), \tag{2.18}$$

where, $\delta(t-t')$ corresponds to the Dirac function. Equation (2.18) allows writing the expression of the electric field J_d as follows:

$$j_d(t) \approx \sigma_0(t)E_{THz}, \tag{2.19}$$

The photo-switches are not ideal detectors, because they do not transcribe the real temporal profile of the terahertz electric field. Indeed, the lifetime of carriers and the inter-electrodes gap are the factors that can limit the capacities of detection of the device (Auston, 1980). The spectral bandwidth of a dipole antenna depends on the distance between its electrodes. A large inter-electrodes gap is very efficient for detecting low frequencies, but its bandwidth remains very narrow. To overcome this problem, we deal with small inter-electrodes gap antennas that allow detecting higher frequencies. Photoconductive detection is characterized by two main advantages, their extreme dynamic greater than 50dB and their sensitivity to the amplitude of terahertz field, not to its intensity. This technique remains the most commonly used technique to detect THz field.

2.6.2 Detection by Electro-optic Effect

The electro-optic effect translates a change in the optical properties (refractive index) of a material in response to an electric field that varies slowly compared to the the frequency of light. Judicious

choice of the group and the crystallographic orientation of the electro-optic substrate, which is illuminated by a THz-electric field, allows rotating the polarization of an optical incident radiation that passes through the crystal. This rotation is proportional to the amplitude of the THz field and can be detected using a standard experimental setup as illustrated in figure 2.8. The generated terahertz field propagates in free space, and passes through the beam splitter and interacts with the ZnTe crystal. The beam splitter is used to couple spatially the THz field and the optical radiation within the ZnTe. The presence of terahertz field induces modification of the index ellipsoid in the crystal by Pockels effect.

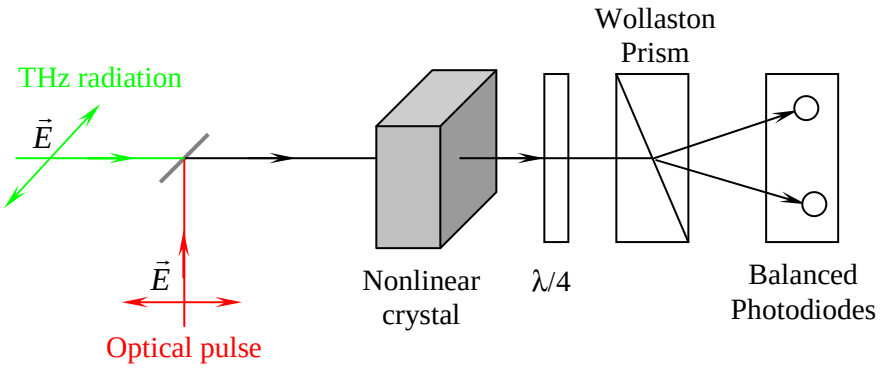

Figure 2.8 : Illustration of the detection by electro-optic effect with a λ/4 plate and a Wollaston polarizer.

The superposition of the optical pulse that is linearly polarized and the terahertz radiation within the crystal gives rise to a phase shift, which is generated by the THz radiation, confers to this later an elliptical polarization. The quarter-wave plate allows measuring polarizations along the two axes. The two components are distinguished by a Wollaston prism before being injected in a balanced photodiodes system. The difference of intensity between the two photodiodes is proportional to the incident THz field as follows:

$$\Delta I = I_{opt} \frac{\pi}{\lambda} n_c^3 E_{THz} r_{41} L_c, \tag{2.18}$$

where r_{41}=3.9 pm/V is the electro-optic coefficient for ZnTe, I_{opt} is the intensity of the optical field, n_c and L are the optical index and the thickness of the ZnTe crystal, respectively. The difference of intensity ΔI is proportional to the electric THz field. If the THz field is not constant, but has the shape of a pulse, the time delay between the THz radiation and the optical beam, should be varied. The reconstruction of the temporal profile of the THz field is performed by raising different values of ΔI versus time. The interested reader can find the full mathematical formalism related to this phenomenon with great details in the paper of G. Gallot et al (Gallot, 1999).

2.7 Terahertz Time Domain Spectroscopy (THz-TDS)

Terahertz time domain spectroscopy (THz-TDS) is a non destructive optoelectronic method for materials studies over a wide range of frequency which extends from a few tens of Gigahertz to a few terahertz. THz-TDS gives access to complex intrinsic parameters (refractive index, absorption, permittivity, permeability, conductivity), of a wide variety of materials such as, dielectrics (Duvillaret, 1996), semiconductors (Van Exter, 1990) and liquids (Pedersen, 1992). Furthermore, THz-TDS allows following the dynamics of ultra-fast charge carriers in semiconductors and interactions carrier-phonon (Grischkowsky, 1990).

The analysis of molecular interactions in condensed phase systems and gazes is also possible by terahertz time domain spectroscopy (Harde, 1991). The determination of the parameters of the material is achieved in a frequency domain, by analyzing the complex transmittance $T(\omega)$ and / or reflectance $R(\omega)$ functions. In this section, we will describe the experimental setup in a transmission configuration that we have used in order to carry out measurements at THz frequencies. Figure 2.9 shows the schematic view of our experimental setup.

Indeed, our standard THz-TDS transmission setup is based on a mode-locked Ti-Sapphire laser providing 80 fs pulses with a 76 MHz repetition rate with an output power of about 800 mW, at the central wavelength of λ_0=800 nm. The laser output is split into pump and probe beams. The pump is focused onto a bare InAs layer for surface field emission of the THz pulse which is further detected with a photo-switch triggered by the probe. After emission, the THz beam is collimated and focused at the sample's location. The time-resolved field variation is measured using the current generated in the LT-GaAs semiconductor receiver. The current induced by the probe beam in the detector is amplified and processed with a lock-in digital amplifier (SRS 830). It is referenced with a mechanical chopper located on the pump path, which is modulated at a frequency of about 1KHz before interacting with the THz emitter. This set up provides a frequency response up to 3.5 THz. The optical path length of the two paths (pump and probe beams) taken at the detector can be modified by an optical delay line, which offers the possibility to take several samples of the terahertz pulse that will be detected according to an equivalent time sampling. Indeed, since we deal with sub-picoseconds laser pulses, the measurement of this type of signals requires a sampling operation according to Shannon theorem. This latter stipulates that for a given signal characterized by a maximum frequency f_{max} in the spectral response, the sampling frequency f_e should be at least equal to $2\times f_{max}$:

$$f_e \geq 2\times f_{\max}, \tag{2.19}$$

The conservation of information included in the signal is then guarantied. We can rapidly deduce that for sampling a THz pulse in real time, we must have an electronic device with a bandwidth of

several terahertz. In other words, it means to be able to take huge number of samples in a record time below the picosecond.

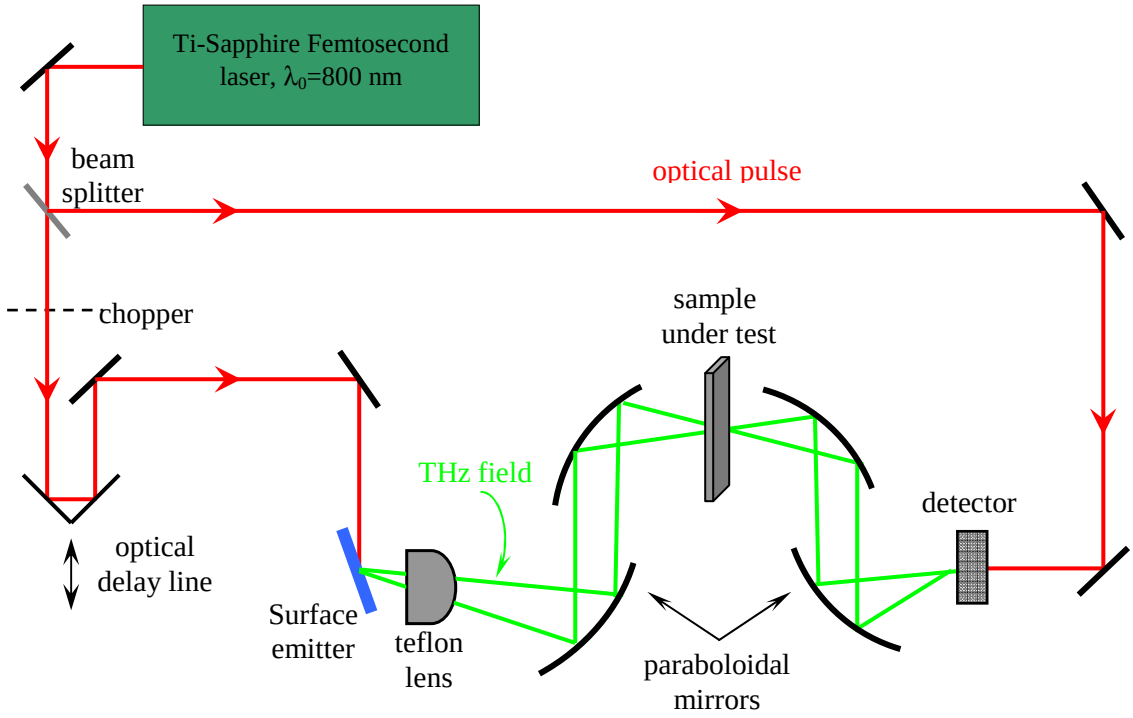

Figure 2.9: Terahertz Time Domains Spectroscopy (THz-TDS), schematic view of our experimental setup in the transmission configuration. The reflexion configuration has not been investigated in this work, we will propose in chapter 4 an alternative method of measurement that give us the possibility to obtain both the transmission and reflexion spectrum of an investigated sample with a single shot transmission measurement at normal incidence.

Till now, the most commonly electronic devices exhibit bandwidths which extend from few tens of gigahertz to few hundreds of gigahertz. Moreover, since the measured signals are generally very weak (~ pA, ~ nA), the electronic device must have a great sensitivity in order to convey rapidly with no losses nor dispersion or attenuation over few centimeters at least from the detector to the measuring device. For these multiple reasons, it is virtually impossible to apply the standard real time sampling technique on THz signals. The equivalent time sampling constitutes an alternative, which offers the possibility to overcome this drawback. Indeed, this technique is possible using standard acquisition systems for the measurement of fast signals (i.e. by using electronic devices with bandwidths that are less than the bandwidths of the measured signals).

The THz radiation to be measured is a periodic signal, the different samples that will be used to reconstitute this latter will be taken over different and successive periods of the signal (see figure 2.11). This indeed requires: periodic signals, synchronization between the measurement system and the measured signals (performed by the chopper) and the possibility to delay precisely the measurements of the signal to be sampled (performed by the delay line). Thus, the measurement of a

THz radiation can be performed over a sufficiently large duration (on several thousands of periods of the signal), which gives us the possibility to perform an average on the measurement for weak signals, in order to increase the Signal/Noise ration. Note that the time increment Δt can be deduced from the spatial increment Δx of the optical delay line as follows:

$$\Delta t = 2\Delta x / c, \tag{2.20}$$

where c is the velocity of the light in vacuum ($c = 3\times10^8$ m/s), the presence of the factor 2 in equation (2.20) results from the round trip of the optical beam in the delay line. The generation of the THz radiation in our experimental setup is based on the surface effect emission as described in section 2.5.1, while a photoconductive antenna is used for the detection (as described in section 2.6.1). The equivalent time sampling is illustrated below in figure 2.9.

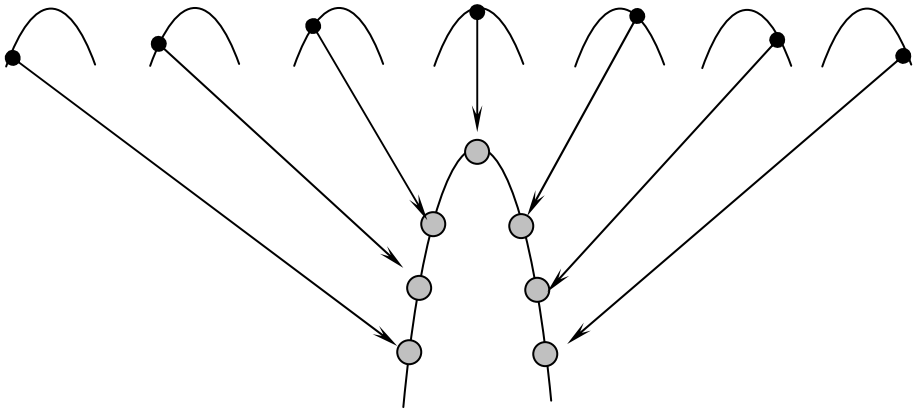

Figure 2.10: Illustration of the equivalent time sampling technique.

A quasi optical system (teflon lens and paraboloidal mirrors) as illustrated in figure 2.9 is required for shaping the THz signal. Indeed, we have placed a teflon lens near the surface emitter, which is accompanied by paraboloidal mirrors in order to focus low-frequency components, since these latter are not sufficiently focused by the teflon lens that have dimensions of the same order or less than the wavelengths of the components. The detected currents are generally very weak as mentioned previously, so a synchronous detection amplifier characterized by a high gain and low noise is used as an electronic measurement device (a current-voltage high gain preamplifier).

Figures 2.11(a) and 2.11(b) show respectively the typical time profile of the THz field that has been measured using the experimental setup of figure 2.9, and the spectral response calculated using the Fourier transform. Measurements are generally performed in a vacuum environment to get rid of the water vapor that results in a series of absorption peaks as illustrated in figure 211(b), and can affect the validity of the measurement. One can see that the useful signal extends from 100 GHz to 4 THz approximately, and can note that the dynamics of the experiment is extremely large (about 50 dB). Below 100 GHz, the THz field is poorly focused by the focusing optics elements and beyond 3THz the

emitter radiates a very weak energy, and the signal is less than the noise. The transmitted signal through the sample $E_{THz\text{-}s}(t)$ is normalized with respect to transmission in free space between the emitter and the detector $E_{THz\text{-}r}(t)$. The determination of the intrinsic dielectric parameters of a given material under investigation is performed by analyzing the complex transfer function in the frequency domain $T(\omega)$.

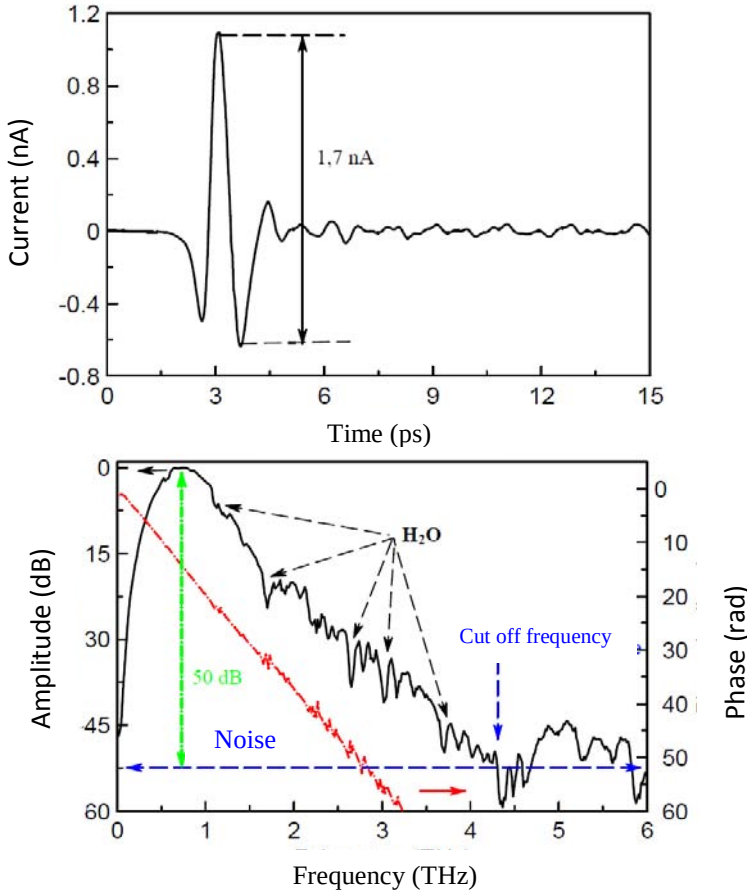

Figure 2.11: (a) Typical temporal profile of the measured THz pulse, (a) magnitude of the spectrum associated to the THz pulse that has been obtained by Fourier transform.

2.8 Conclusion

A brief description of numerical methods used in this work to predict the spectral behavior of our investigated structures has been given (Finite Element Method and Transmission Line Matrix Method, respectively). We have also described the quasi optical non destructive free space measurement setup based on horn antennas and network vector analyzer used to carry out experiments at microwave frequencies. A general overview of some terahertz sources has been given. The most common techniques used in the generation and the detection of Terahertz field have been also given. Finally the terahertz time domain spectroscopy (THz-TDS) setup has been presented.

Chapter 3

Investigations of Metamaterials at Microwave Frequencies

3.1 Introduction

Periodic stuctures have been used in many different applications, in the microwave field, and an extensive and sophisticated periodic-structure theory has been developed over the past 50 or more years in connection with these applications. The applications include microwave tubes, linear accelerators, filters, artificial-dielectric materials, leaky wave antennas, slot arrays, phased-array antennas, frequency selective surfaces, and so on. Within the past few years, a new terminology has been introduced in the microwave field : "Electromagnetic Band Gap Structures", this terminology comes from the photonics field in reference to the "Photonic Band Gap Structures" due to the similarities between the stop-band performance of optical periodic structures and solid state electronic band gaps.

In the first part of this chapter, we propose to investigate a Frequency Selective Surface calculated, fabricated and experimentally characterized around 40 GHz, and then applied as a Partially Reflecting Surface (PRS) in a Fabry-Pérot cavity in order to enhance the performances of printed antennas. This work has been performed in collaboration with our colleagues (Pr. André de-Lustrac and Dr. Shah Nawaz Burokur) from Institut d'Electronique Fondamentale at university of Paris-Sud 11. The second part of this chapter is dedicated to the study of "new" class of metamaterials, the so-called "fishnet metamaterials" which exhibit negative refractive index at millimeter frequency band. Indeed, we will present the theoretical and experimental studies carried out on different fishnet structures.

Initially, we used an electromagnetic software simulator based on the finite element method (HFSS) in order to predict the spectral response of our metamaterials, then we applied the numerical retrieval method (Smith, 2002) in order to extract the effective parameters of the considered metamaterial z_{eff}, n_{eff}, μ_{eff} and ε_{eff}. In this present dissertation we adopted the following expressions of the effective parameters $\mu = \mu' + j\mu''$, $\varepsilon = \varepsilon' + j\varepsilon''$, $z = z' + jz''$ and $n = n' + jn''$, and we assumed a time dependence of the form $e^{-i\omega t}$. Two different manufacturing procedures have been used to fabricate our prototypes: standard optical lithography and mechanical micromachining technique. Experimentally, we have used a non-destructive free space setup at microwave frequencies based on the use of a Vector Network Analyzer, transmitting and receiving horn antennas in order to measure our fabricated prototypes.

3.2 Frequency Selective Surfaces

Since the emergence of the Frequency Selective Surfaces (FSSs) in the early 60's, many researchers have contributed to their development and integration in modern telecommunications systems, in order to achieve spatial filtering operation (Zhang, 1993, Huang, 1994, Romeu, 2000,

Parker, 2001, Schoenlinner, 2004, Sarabandi, 2007, Lin, 2009). The Frequency Selective Surface (or dichroic structures) to space waves are the counterparts of filters in transmission lines. Once exposed to an electromagnetic radiation a Frequency Selective Surface acts as a spatial filter, causing some frequencies to be transmitted and some others to be reflected. FSSs have been used traditionally by military in stealth technology for reducing the Radar Cross Section (RCS) of an antenna system outside its frequency band of operation. FSSs are formed by periodic arrays of usually metallic elements on a dielectric substrate; they may be also in the form of slots etched through metal plate. The response of a Frequency Selective Surface is entirely determined by the size and geometry of the unit element, periodicity, and also by electrical properties of the dielectric substrate. Considered as a subclass of metamaterial surfaces also known as metasurfaces, FSSs with their remarkable properties in controlling the propagation of electromagnetic waves have found many applications, which make them promising solutions to antennas and microwave circuit's problems. Some examples are reflector antennas, radome design, polarizers, beam splitters and planar radar absorbers. In the following sections, I will present the study hat has been performed on a planar Frequency Selective Surface (FSS) operating in the microwave regime. It should be noted that the results of this study is the subject of a paper that has been submitted for publication (Yahiaoui, 2011).

3.2.1 Design, Fabrication and Characterization of our Frequency Selective Surface at millimeter wavelengths

The unit cell of our frequency selective surface is shown in figure 3.1(a). It consists of a 35µm thick metallic (copper) pattern printed on one side of a 0.5mm thick dielectric substrate (Epoxy, ε_r = 4.4, tan(δ) = 0,02) using the standard optical lithography. The unit cell of our investigated structure is repeated periodically along the electric $\vec{E}$ and magnetic $\vec{H}$ field directions with the following geometrical dimensions: ***a*** = 4 mm, ***b*** = 3 mm, ***c*** = 1 mm and ***d*** = 3 mm. Using the full wave electromagnetic simulator based on the finite element method (HFSS), we performed simulations in order to predict the frequency response of the structure.

It should be noted that for saving computing time, only one unit cell is designed in HFSS and appropriate boundary conditions (electric and magnetic walls) are wrapped around the unit cell in order to simulate an infinite bi-dimensional array. The sample is illuminated by a plane wave (TM mode, $\vec{E}$//z, $\vec{H}$//y and $\vec{k}$//x) at normal incidence with only one layer along the direction of propagation $\vec{k}$. Microwave measurements have been done on a fabricated prototype composed of 23 × 25 cells. The reflection and transmission measurements have been performed applying the AB Millimetre™ vector network analyzer and horn antennas in a quasi-optical configuration (described in chap. 2, sec.2.3). In the transmission measurements, the incident plane waves are normal to the sample surface and the transmitted intensity is normalised with respect to transmission in free space between

the two horn antennas. Similarly, the reflection coefficient, measured with a directional coupler in the reflexion geometry, is normalised using a sheet of copper as reflecting mirror Figure 3.1(b) shows the simulated and measured transmission response of the FSS. We observe a pass band frequency behavior centered around 40 GHz with a bandwidth at -3 dB estimated at 6 GHz. The bandwidth is rather wide, which indicates the poor selectivity of the spatial filter. Further simulations performed on our FSS, taking into account the TE mode (i.e. $\vec{E}$ //y, $\vec{H}$ //z and $\vec{k}$ //x) over a wide frequency band up to 75 GHz, as illustrated in figure 3.1(c), reveal that the fundamental resonant mode which occurs at 40 GHz in TM mode, completely disappears in TE mode and remains only the higher mode orders beyond 68 GHz. The transmission peak reaches a maximum value of about -1 dB at 40 GHz and a fairly good agreement is reported between theory and experiment.

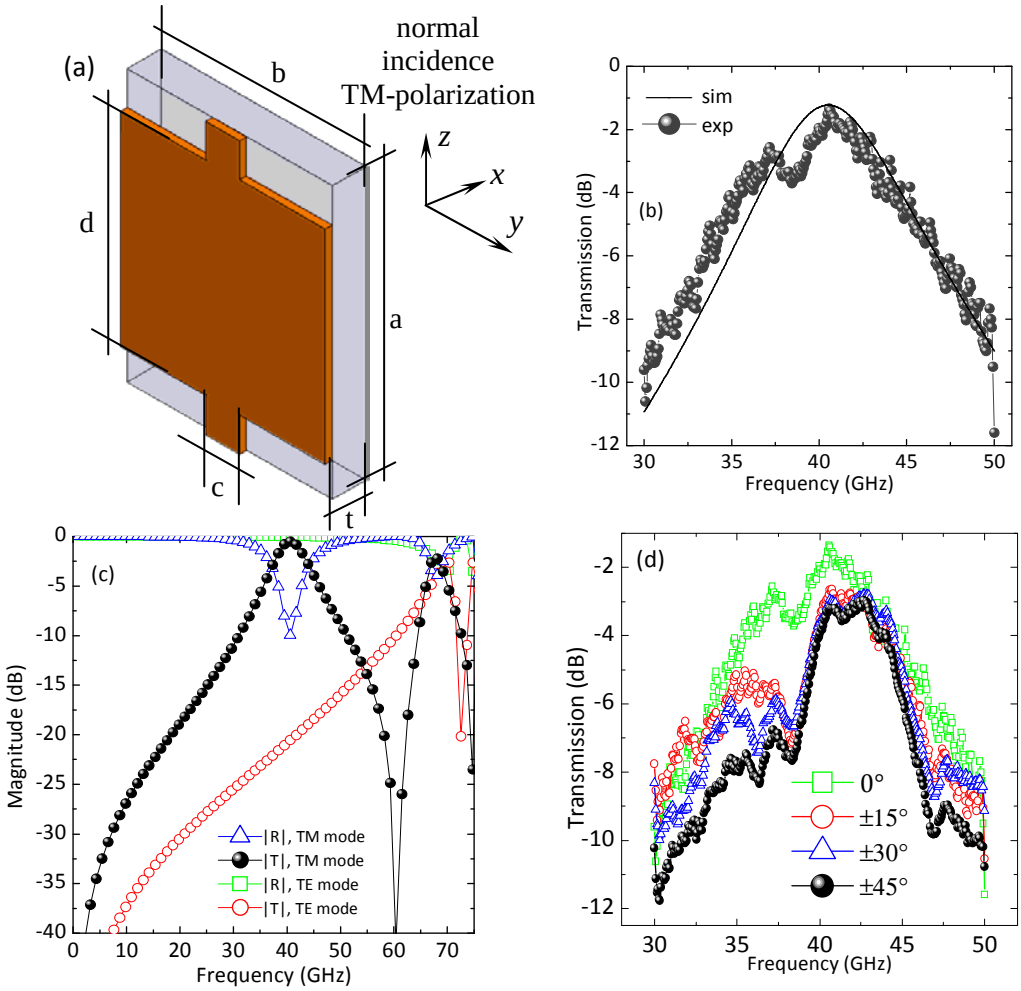

Figure 3.1: (a) Unit cell of our investigated Frequency Selective Surface with the relevant geometrical dimensions a=4mm, b=3mm, c=1mm, d=3mmm t=0.5mm. (b) magnitude of the simulated (solid line) and measured (line and symbols) transmission coefficient. (c) comparison of the magnitudes of transmission and reflexion coefficients for TE and TM polarization, (b) magnitude of the transmission coefficient of the FSS measured for different incidence angles -45°<θ<+45°.

We also focused on the dependence of the frequency selective surface on the incidence angle of the electromagnetic exciting wave. Figure 3.1(d) shows the transmission coefficient that has been measured, for different values of the incident angle. The transmitting and receiving antennas are fixed, while the sample under investigation is rotated. The spectral response of our FSS remains substantially unchanged for incidence angles between ± 45°, which is potentially very interesting for oblique incidence applications.

The dip in the measured transmission around 38 GHz near the resonant frequency is due to the finite nature of the fabricated prototype, since we have simulated in HFSS an infinite 2D structure, which is fully illuminated by a plane wave. Further numerical calculations that have been performed but not shown here demonstrated the critical influence of a more realistic and finite prototype on the spectral response. This dip is much more pronounced beyond ±15° incidence since the number of unit cells illuminated by the incident wave-fronts is reduced.

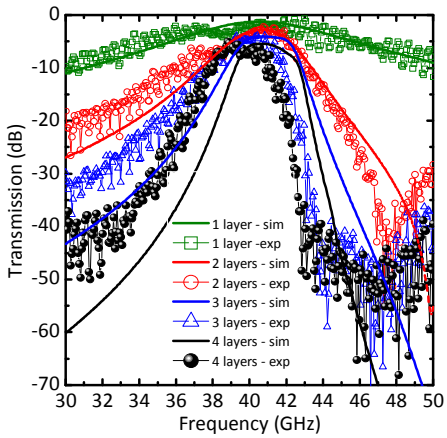

Figure 3.2: Magnitude of the calculated (solid lines) and measured (lines+symbols) transmission coefficient for 1, 2, 3 and 4 stacked layers respectively along the direction of propagation k.

Depending on the targeted application, the selectivity of a spatial filter can be a very important and critical characteristic in its functionality, which should be taken into account during the designing procedure. We propose here to enhance the selectivity of our FSS by staking several layers of our prototype along the direction of propagation *k*, and regularly spaced by an air gap g_{air} = 1 mm. Indeed, the selectivity of the spatial filter is significantly increased as shown in figure 3.2 and a fairly good quantitative agreement between the simulated (solid lines) and measured (lines and symbols) transmission coefficient for 1, 2, 3 and 4 FSS layers is observed. Indeed, the bandwidth of the filter at -3 dB goes from 6 GHz to 3 GHz for 4 FSS staked layers, the same effect has been reported in previous works (Lunet, 2009). This effect is very promising for highly selective filtering applications. We also notice a decrease in the level of transmission at the 40 GHz resonant frequency, with a minor shift towards low frequencies in the measured responses, in the case of 3 and 4 staked layers,

compared to the simulated responses. This is may be due to the shift that can occur between the metallic patterns when the layers are stacked.

3.2.2 Tunability of the Spectral Response of the Frequency Selective Surface

Frequency tunable responses of electronic and electromagnetic devices are highly desired, since they offer the possibility to operate at different frequencies. The most common method to obtain tunability is to change the effective electric length or the effective permittivity of the structure, and the techniques used to reach this goal are various and widely discussed in scientific literature. The design and development of agile functions based on localized components is extremely dynamic, it consists to integrate well-known and controlled elements such as Diodes (Vardaxoglou, 1993, Chang, 1996, de-Lustrac, 2001, Yang, 2002, Mias, 2005, Djermoun, 2006, Mercier, 2006, Chen, 2006, Ourir, 2009), MEMS and Transistors (Barlevy, 1999, Poilasne, 2000, Gianvittorio, 2002) to a standard passive structure.

It is also possible to use materials such as liquid crystals (Dolfi, 1993, Busch, 1996, Takeda, 2002, Chen, 2004), piezoelectric materials (Chang, 2002), ferroelectrics (Parker, 1996, Kuylenstierna, 2003, Yashchyshyn, 2005, Hidaka, 2005, Hu, 2007) and ferromagnetic (Pozar, 1993, Chang, 1994, Adam, 2002) in order to achieve reconfigurable structures. In this section, we propose theoretically an original way to tune the response of our Frequency Selective Surface. The basic idea consists in stacking two layers of our FSS spaced by an air gap g_{air} = 1 mm, and to apply a lateral displacement denoted by ***d*** along ***yy'*** axis to only one layer with regard to the other, as illustrated in figure 3.3(a).

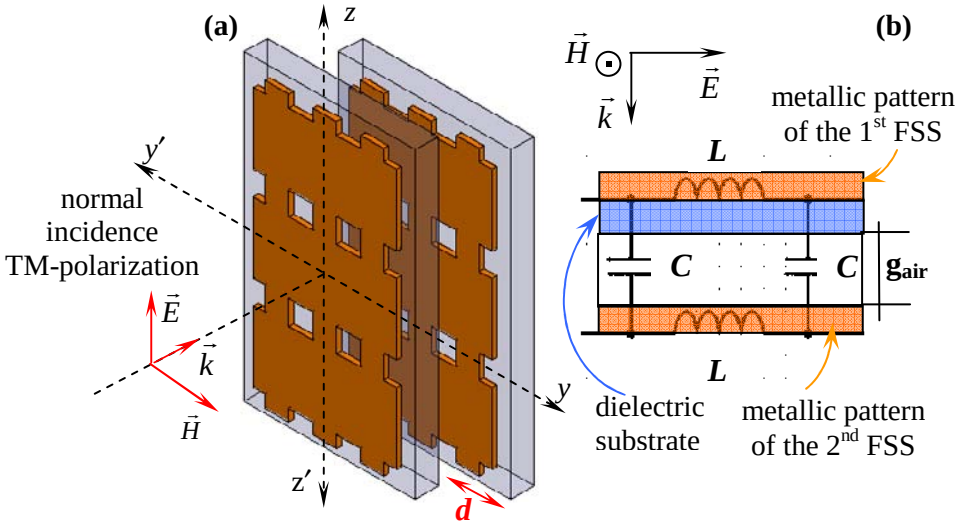

Figure 3.3: (a) configuration of our system which leads the tunability of the spectral response of the double-FSS, one layer of the double-FSS translates horizontally along the yy′ axis, while the second layer remains fixed (b) equivalent electrical circuit proposed of the unit cell of our system, which consists of stack of two FSSs along the direction of propagation $\vec{k}$ separated by and air gap g_{air}=1mm.

Indeed, the total structure can be regarded as an electric equivalent ***LC*** circuit that resonates at the frequency f_r in the path of an incident plane wave as shown in figure 3.3(b). The resonant frequency strongly depends of the electric properties of the material used and the geometrical dimensions of the unit cell of the sample. The inductance ***L*** corresponds to the inductance of the metallic patterns of the unit cell along the direction of the electric field $\vec{E}$ and ***C*** corresponds to the capacitance created between the two metallic patterns separated by the dielectric substrate (epoxy) and the air-gap. The capacitance *C* takes into account both the capacitance C_n of the so called *neck pair* and the capacitance C_s of the so called *slab pair* as detailed by (Kafesaki, 2008) for the fishnet structure. This proposed equivalent circuit will be discussed in details in section 3.4.4, related to fishnet metamaterials.

The electromagnetic frequency of the equivalent circuit is given by the following approximate expression (Yan, 2008): $f_r = 1/2\pi\sqrt{LC}$. The lateral displacement along the *yy'* axis of one layer in the double-layered FSS causes a misalignment of the metal patterns, changing C_n and thus modifying the resonant frequency of the structure. In this case, both ***L*** and $\boldsymbol{C_s}$ is unchanged. Figures 3.4(a) and 3.4(b) show the tunability effect on the transmission and reflection spectra, respectively for different values of the parameter ***d***. The resonant frequency decreases from its nominal value 41 GHz to 32 GHz, approximately when ***d*** goes from 0 µm to 500 µm (we obtained about 22% of tunability). From our calculations, we have also noticed that the translation of one layer along the electric field $\vec{E}$ direction (polarized alond ***zz'*** axis) does not affect significantly the response of the FFS, creating only a minor level of tunability.

In this type of translation, we will be in presence of two possible situations; either one *neck* faces another *neck* or one *neck* faces a *slab*. In both cases, $\boldsymbol{C_n}$ will be similar. However, $\boldsymbol{C_s}$ will be modified, but only slightly, ***L*** remains also unchanged, the minor level of tunability is then expected. The main transmission peak centred at about 41 GHz splits into new peaks which move in opposite directions. The fundamental mode decreases in intensity and moves towards low frequencies from 41 GHz to 32 GHz approximately, when ***d*** increases from 0µm to 500µm. Furthermore, a resonant frequency of about 25 GHz is reached for the fundamental mode, when the horizontal displacement ***d*** is set to 1mm. Higher order resonant modes are observed around 42.5 GHz and 46 GHz on both reflexion and transmission coefficients, as depicted in figures 3.4(a) and 3.4(b).

For a better understanding of the origin of these additional peaks, we have performed a series of numerical simulations on our double-layerd FSS. Our investigations reveal that each peak is in fact the contribution of different sub-elements constituting the unit cell of our double-layerd FSS, thus the resulting response is the superposition of each sub-element′s response. Similar effects have been already observed for multiple-frequency band applications in terahertz regime (Yuan, 2008, Yahiaoui, 2009, Yahiaoui, 2011). Indeed, the dissymmetrical unit cell of our investigated double-FSS can be

regarded as a combination of an array of shifted metallic long-wires pairs in the direction of electric field and an array of double-plate pairs as illustrated below in figure 3.5.

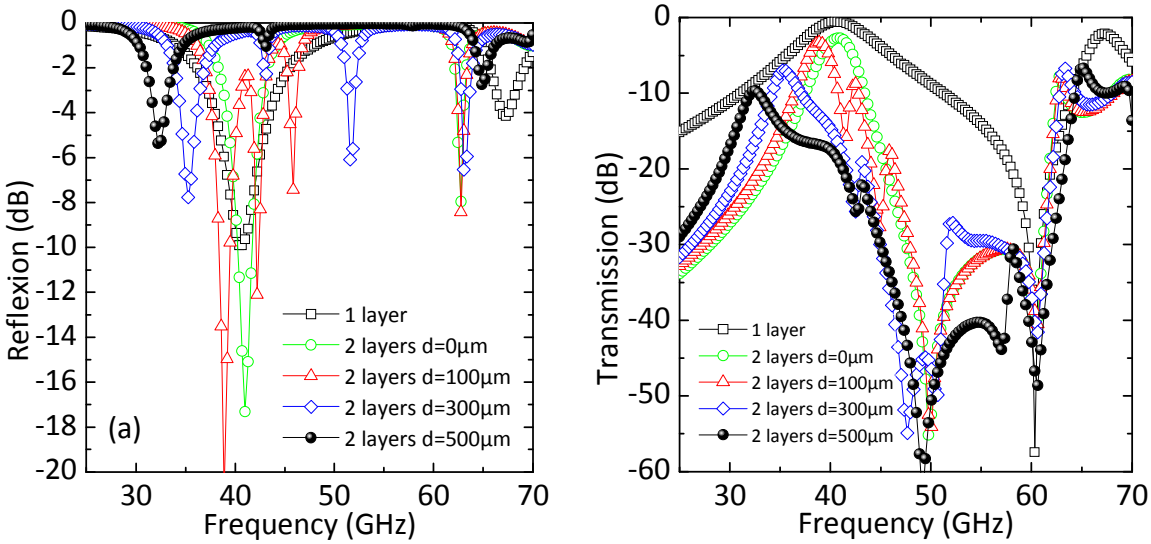

Figure 3.4: Evolution of the reflecion (a) and the transmission (b) coefficients for different values of the displacement ***d*** along ***yy'*** axis from 0 µm to 500 µm, the tunability is about 22 % from 41GHz to 32 GHz.

The first and the second higher order modes that appear at about 42.5 GHz and 46 GHz approximately, comes from the metallic shifted continuous wires pairs and the third higher order mode that occurring around 62.7 GHz corresponds to the contribution of the double-plate pairs. Figure 3.6(a) shows the reflection coefficient of each individual sub-particle. Furthermore, the extraction of effective parameters of our investigated double-FSS using the classical retrieval method (Smith, 2002) reveals that the additional peaks supported by the structure show both electric and magnetic activity. Indeed, both effective permeability and effective permittivity of the structure exhibit a resonant behavior at the aforementioned frequencies, as illustrated in in figures 3.6(b) and 3.6(c).

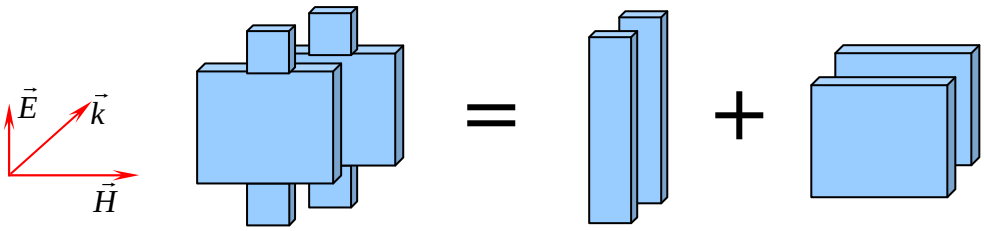

Figure 3.5: Decomposition of the unit cell of our investigated double-FSS into long-wires pairs and double-plate pairs in order to explain the origin of the additional peaks observed in the spectral response.

At this stage, it is important to note that when the air gap g_{air} and the horizontal shift ***d*** are set to 0, the double-layered FSS can be assimilated to the previously reported fishnet structure (Kafesaki, 2007, Yan, 2008), presenting a negative refractive index. However, due to the air gap of 1 mm used in our study, negative refractive index will not be observed. Indeed, in our case, the refractive index does not

reach negative values, as illustrated in figure 3.6(d), because the negative electric and magnetic regions do not overlap (see chap.1, sec. 1.5.1 related to the necessary condition leading to a negative refractive index). Indeed, the electric plasma frequency f_p~38.4 GHz is located below the first magnetic resonant frequency f_{m1}=38.9 GHz, in other words the metallic parts of the structure are too much diluted. Despite this drawback, further numerical calculations reveal that the air gap g_{air} contributes efficiently to obtain a much broader frequency region of negative permeability compaired to what is commonly used to obtain in scientific literature in classical "magnetically active" resonant structures.

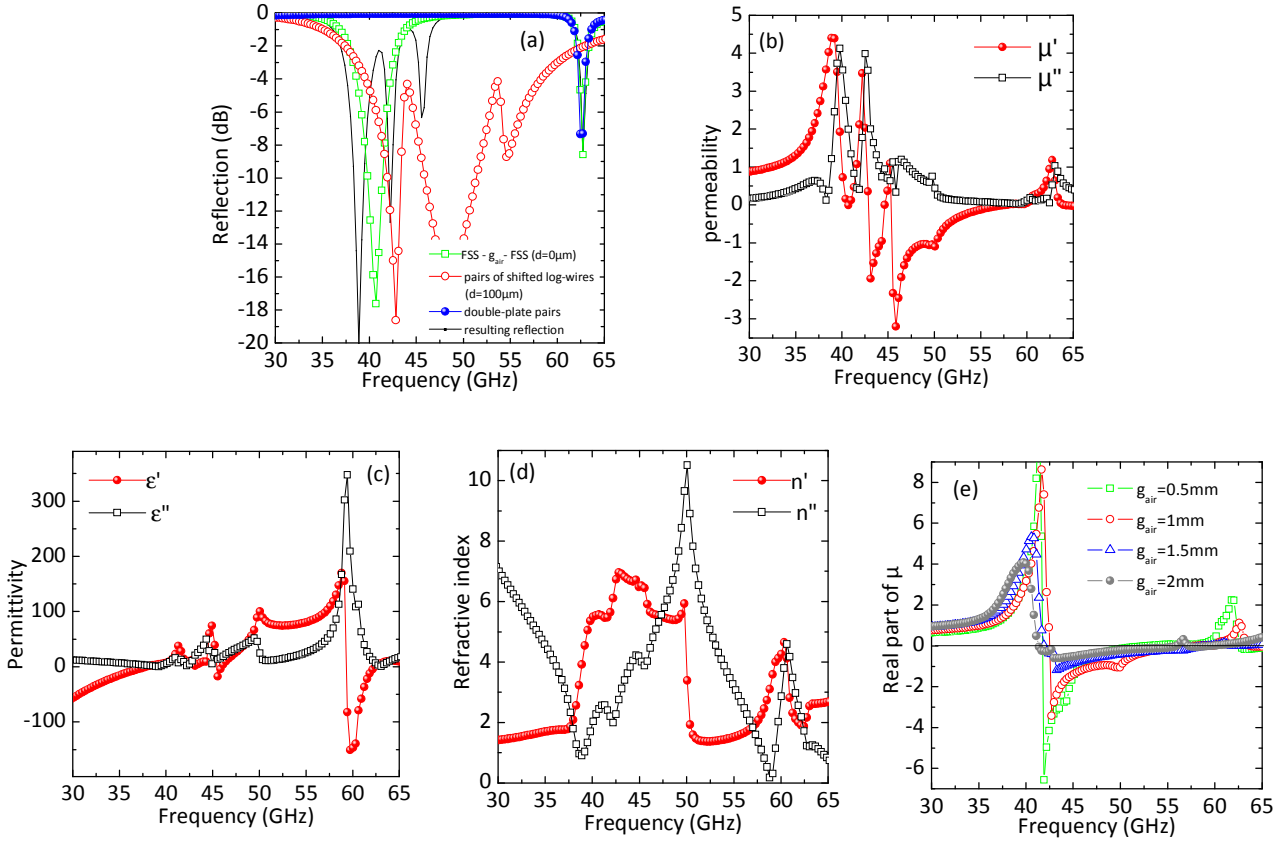

Figure 3.6: Illustration of the origin of additional peaks that appear on the reflexion coefficient of the dissymmetrical (***d***=100µm) double-FSS. Extraction of the effective parameters: (b) permeability, (c) permittivity, and (d) refractive index, (e) influence of the air gap g_{air} in the enlargement of the region of negative µ, g_{air} varies from 0.5mm to 2mm, where the horizontal displacement ***d*** is set to zero.

Indeed, as we will see in the following sections, which are dedicated to the study of fishnet metamaterials, these latter exhibit a very narrow (few gigahertz only) frequency band of negative ***µ***. A moderate air gap of about 1mm, with no horizontal displacement (***d*** = 0µm) gives the best compromise in terms of *the frequency range* (about 16 GHz, from: 42.5 to 58 GHz) and the *amplitude level* of negative ***µ*** (see figure 3.6(e)). The third higher order mode around 62.7 GHz that arises from the contribution of the double-plate, exhibits both electric and magnetic resonant behavior, as illustrated in

figures 3.6(b) and 3.6(c), respectively. We notice that the electric resonance is much more pronounced that the magnetic resonance at this frequency.

As a partial conclusion, we have theoretically and experimentally investigated a planar FSS that has been designed, fabricated and characterized for an operation frequency in the microwave regime. The selectivity of the studied FSS is considerably enhanced when stacking several layers. The angular robustness of the transmission response was demonstrated, and an original technique has been proposed in order to obtain a tunability on the spectral response. We will now propose, in the following section, a potential and interesting application of this metasurface, as a Partially Reflecting Surface (PRS) in Fabry-Pérot (FP) cavity in order to enhance the directivity of printed patch antennas.

3.3 Application of the Frequency Selective Surface as a Partially Reflecting Surface in a Fabry-Pérot Cavity Antenna

Antennas are devices that may radiate (transmitter) or receive (receiver) electromagnetic waves and make it possible to liaise between two distinct areas. This means of transmission is advantageous from an economic point of view, since the areas to connect are remote. It is also interesting in terms of logistics and ergonomic, when the areas to cover are difficult to achieve using a traditional wired system. Antennas are classified by different parameters such as: Gain, Radiation Pattern, Directivity, Operating Band and Bandwidth.

A first classification of antennas can be made using the criterion of directivity, depending on the targeted application, we can seek for an illumination of the surrounding space, as uniform as possible, or a localized illumination in a specific direction. Each of these categories of antennas has its own applications. Indeed, non-directive antennas are usually used in the case where the position of the receiver is not necessarily known, such as mobile phone applications and radio communications. Directive antennas are used for point to point links, where the positions of transmitting and receiving devices are well known, such as uplink (a link from terrestrial transmitter to satellite receiver) and downlink (a link from satellite transmitter to terrestrial receiver) communications, or links type: **L**ocal **M**ulti-point **D**istribution **S**ervice (**LMDS**).

This type of antennas is very interesting to increase the scope of the radio communications links and for increasing the flow of the transmissions. In this section, we will particularly focus in directive-antennas. Several technologies can be used in base and mobile stations such as lens antennas (Fernandes, 1999) and printed antennas array (Levine, 1989, Lafond, 2000), but the feeding mechanism of the array leads to a significantly loss in efficiency. Another way to achieve directive antennas is to place a source between two reflectors to form a Fabry-Perot resonant cavity antenna as introduced for the first time by G. V. Trentini in the 50's (Trentini, 1956). With the phase constraint

related to the multiple reflections suffered by the electromagnetic wave inside the cavity from a reflector to another, a cavity thicknesses of about $\lambda/2$ (λ is the operating wavelength) were used since each reflector presented a reflection phase of 180°.

3.3.1 Fabry-Pérot Cavity Antenna

The purpose of this section is to use our investigated Frequency Selective Surface (FSS) in a Fabry-Perot cavity, in order to realize high directivity antennas with narrow beam and low side lobes. Figure 3.6 shows the quasi-optical cavity model proposed by G. V. Trentini in 1956 (Trentini, 1956), this structure simulates the operation of antennas array, and the functioning principle is based on the Fabry-Perot interferometer and the optical ray theory. The Fabry-Perot cavity antenna proposed by G. V. Trentini consists of a completely reflecting screen and partially reflecting sheet, separated by a distance l as shown in figure 3.7. An electromagnetic wave source placed in S is used to feed the entire system, the reflection coefficient of the sheet can be written as: $Pe^{j\psi}$. Assuming no transmission losses, the amplitude of the direct ray 0, the once-reflected ray 1 and the twice-reflected ray 2, …etc, are proportional to $\sqrt{1-p^2}$, $p\sqrt{1-p^2}$ and $p^2\sqrt{1-p^2}$, respectively, where p is the magnitude of the reflexion coefficient. The Electric field intensity in the Fraunhofer zone (far field region) consists of the vector sum of these partial rays, and for an infinite screen and sheet we may write the following expression:

$$E = \sum_{n=0}^{\infty} f(\alpha) E_0 p^n \sqrt{1-p^2}\, e^{j\theta n}, \tag{3.1}$$

The phase angle θ is composed of the phase variations during reflections from the completely reflecting screen (π) and partially reflecting sheet (ψ), and also of the path differences of the partial rays. The phase difference between ray 1 and ray 0 may be written as :

$$\left[\theta_1 = \frac{2\pi}{\lambda} 2l \tan(\alpha)\sin(\alpha) - \frac{2\pi}{\lambda}\frac{2l}{\cos(\alpha)} + \pi + \psi\right]_0^1, \tag{3.2}$$

And between ray 2 and 0 as

$$\left[\theta_2 = \frac{2\pi}{\lambda} 4l \tan(\alpha)\sin(\alpha) - \frac{2\pi}{\lambda}\frac{4l}{\cos(\alpha)} + 2\pi + \psi\right]_0^2, \tag{3.3}$$

Which, somewhat transformed, gives

$$\theta_n = n\theta = n\left[-\frac{4\pi}{\lambda} l\cos(\alpha) + \pi + \psi\right], \tag{3.4}$$

Since P<1, we obtain:

$$\sum_{n=0}^{\infty}\left(pe^{j\theta}\right)^n = \frac{1}{1-pe^{j\theta}}, \tag{3.5}$$

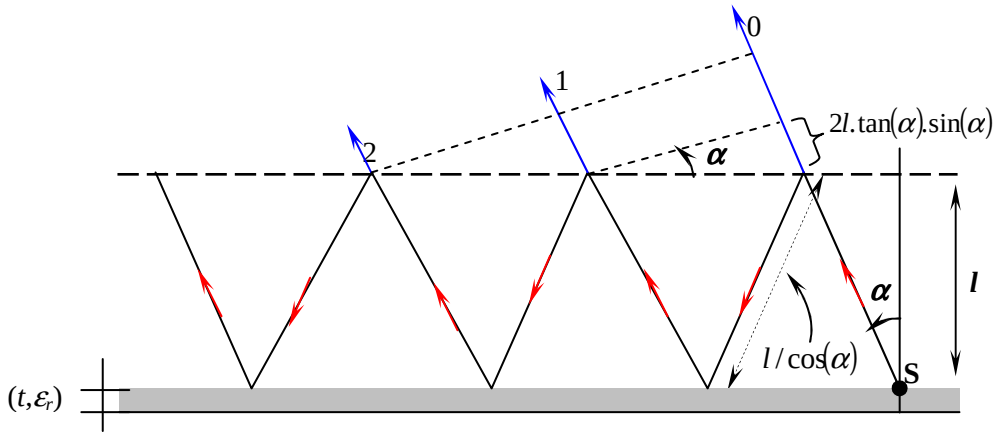

Figure 3.7: Schematic view of the Fabry-Pérot cavity antenna proposed by G. V. Trentini in 1956 (Trentini, 1956).

Inserting (3.5) in (3.1), the absolute value of field strength becomes

$$|E| = |E_0|\, f(\alpha) \sqrt{\frac{1-p^2}{1+p^2-2p\cos\theta}}, \tag{3.6}$$

And the power pattern is therefore

$$S = \frac{1-p^2}{1+p^2-2p\cos\left(\psi+\pi-\frac{4\pi}{\lambda}l\cos(\alpha)\right)} f^2(\alpha), \tag{3.7}$$

We must take into account that the amplitude P and the phase ψ of the sheet reflection coefficient are functions of the angle of incidence α. Maximum power in the direction of α=0° is obtained when

$$\psi + \pi - \frac{4\pi}{\lambda} l = 0, \tag{3.8}$$

The equation determining the resonance distance l_r of the sheet is

$$l_r = \left(\frac{\psi}{360} + 0.5\right)\frac{\lambda}{2} \pm N\frac{\lambda}{2}, \tag{3.9}$$

With $\boldsymbol{\psi}$ represents the reflection phase of the partially reflecting surface (expressed in degree), $\boldsymbol{\lambda}$ is the operating wavelength and $\boldsymbol{N}$ is an integer corresponding to the order of the cavity's electromagnetic mode. Taking into account the thickness of the antenna's substrate $\boldsymbol{t}$ and its relative dielectric permittivity $\boldsymbol{\varepsilon_r}$, the resonant thickness of the Fabry-Perot cavity can be expressed as follow:

$$l_r = \left(\frac{\psi}{360} + 0.5\right)\frac{\lambda}{2} - t\sqrt{\varepsilon_r} \pm N\frac{\lambda}{2}, \tag{3.10}$$

In recent years, this class of antennas has received renewed interest particularly with the development of metallo-dielectric periodic structures, and they have been studied as reflex-cavity

antennas for their directive emissions (Sievenpiper, 2003, Feresidis, 2005, Zhou, 2005, Ourir, 2006, Yahiaoui, 2009, Burokur, 2009). If it is necessary that these antennas possess good performances and low sidelobes to reduce the influence of multipath, they must also lead to low cost and compact systems in order to integrate them into transmitting and receiving devices. In this context, if the wavelength λ, the permittivity and the thickness of the substrate ε_r and t are fixed, the resonant thickness l_r of the cavity can be minimized by reducing the reflection phase of the partially reflecting surface ψ according to equation (3.10).

Taking advantage of the phase dispersive characteristics of metasurfaces, several models of reflex-cavity antennas have been proposed over the last few years in scientific literature. Indeed, Feresidis et al (Feresidis, 2003), have proposed a $h=\lambda/4$ thick cavity, which is slightly more compact than the standard Fabry-Pérot cavity by using a meta-surface which exhibits a zero reflection phase at resonant frequency instead of 180°. Zhou et al (Zhou, 2005) proposed a much more compact cavity antenna with a thickness of about $h=\lambda/12$, using dispersive characteristics of High Impedance Surface (HIS) of Sievenpiper (Sievenpiper, 2003). Subsequently, Ourir et al (Ourir, 2006) demonstrated an ultra-compact $h=\lambda/60$ resonant Fabry-Pérot cavity antenna based on the use of low reflexion phase of metamaterial structures.

3.3.2 Our FSS-based Fabry-Pérot Cavity

Following our investigations on the FSS in the above sections, we now propose a potential and interesting application of the latter surface. Indeed, the FSS can be very useful as a metasurface reflector in Fabry-Pérot (FP) cavities. Consequently, we propose to evaluate the studied FSS as a Partially Reflecting Surface (PRS) in a FP cavity so as to enhance the directivity of antennas based on the use of a single feeding source. For antenna experimental measurement setup availability, we carry out this application investigation in the X band at around 9 GHz. Here we design our FSS in order to act as the PRS in such a reflex-cavity antenna. Using a standard printed circuit board and optical lithography, a planar prototype composed of 9×9 cells having optimized geometrical dimensions: a = 18 mm, b = 12 mm, c = 3.5 mm and d = 12 mm, has been fabricated on the epoxy substrate of thickness 1.6 mm and(ε_r=4, tan(δ)~0.05) in order to validate simulation results.

Measurements have been carried out in the anechoic chamber of IEF using a network vector analyser, and two horn lens-antennas working in the [2 GHz - 18 GHz] frequency band are used as emitter and receiver, as shown in figures 3.8(a) and 3.8(b)). Figures 3.8(c) and 3.8(d) show the calculated and measured magnitudes and phases of transmission and reflection coefficients of our investigated FSS, with a good quantitative agreement between theory and experiment. Our proposed structure can be regarded as a pass-band spatial filter, with a first resonant mode localized at about 7.5 GHz, which exhibits about 90 % of transmission (|T|= -1 dB). At the working frequency of the Fabry-

Pérot cavity, a high level of reflectivity is required (R should be as close as possible to unity) in order to confine electromagnetic waves in the cavity. This confinement allows achieving high directivity, since the expression of the maximum boresight directivity is given by D_{max}= (1+R)/(1-R) (Feresidis, 2005). From figure 3.8(c), one can see that beyond the resonant frequency of the fundamental mode particularly around 9.5 GHz, which corresponds to the operating frequency of our system, the FSS plane exhibits a reflectivity of about 89 % (R ~ 0.89 ~ −1dB), which is quite enough to confine the electromagnetic wave and then enhance the directivity of the source (patch antenna). The reflection phase varying from +180° to -180° and passing through zero at resonance 7.5 GHz (see figure 3.8(d)), is used to determine the thickness of the cavity. The schematic view of the Fabry-Perot cavity and the picture of our fabricated FSS, used as PRS are given in figure 3.9(a).

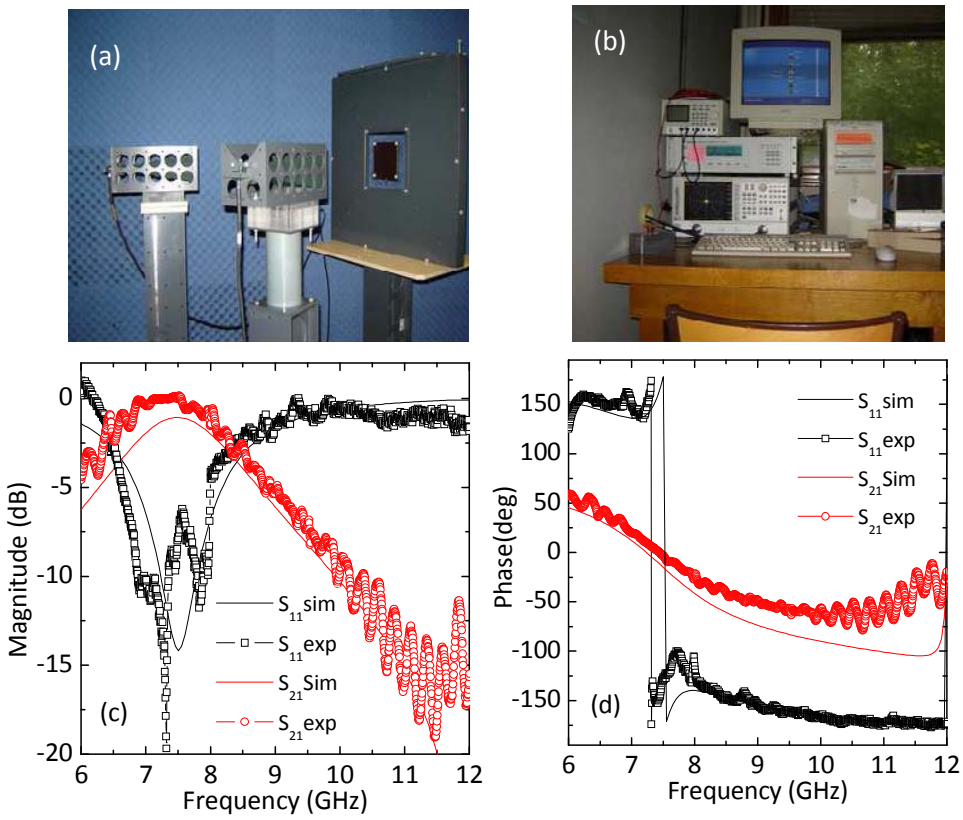

Figure 3.8: (a)-(b) pictures of the experimental equipment from: Institut d'Electronique Fondamentale (IEF) used for measurements. Calculated (solid lines) and measured (lines and symbols) magnitudes (c) and phases (d) of the transmission and reflexion coefficients of our proposed FSS, used as Partially Reflecting Surface in the Fabry-Perot cavity. The single feeding source is a square copper patch antenna (6.2mm × 6.2mm) printed on 1.6mm thick epoxy (εr=4, tan(δ)~0.05) operating at about 9GHz.

Taking into account the thickness of the antenna's substrate (t=1.6mm), and its electric properties (ε_r=4, tan(δ)=0.05), we have depicted in figure 3.9(b)) the thickness $\boldsymbol{l_r}$ of the cavity versus frequency, given by equation (2.10) from calculated and measured reflection phases, at which the maximum of boresight directivity (θ = 0°) can be obtained. At the operating frequency of 9.5 GHz, the reflection

phase is very close to -180°, suggesting a cavity thickness l_r of about 15 mm ~ $\lambda/2$. A good agreement is observed between the different results. From the return loss spectrum shown in figure 3.9(c), we can see a clear deep around 9.5 GHz which corresponds to the resonance mode of the patch antenna. One can see that the resonant frequency of the Fabry-Pérot cavity is slightly shifted towards low frequencies at around 9GHz. Both the patch antenna and the Fabry-Pérot cavity exhibit a good impedance matching (i.e. $|S_{11}|$<-10 dB).

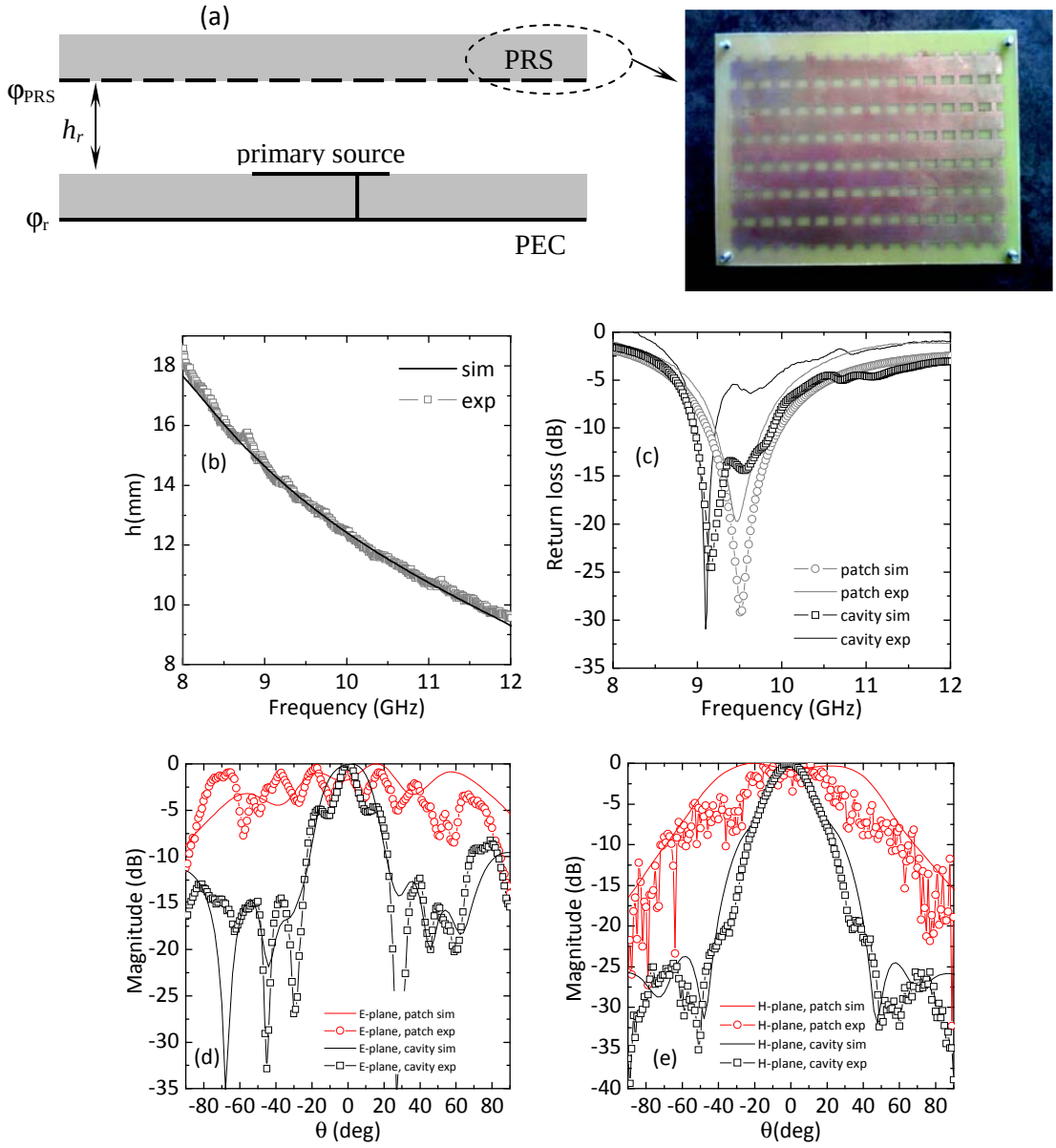

Figure 3.9: (a) Schematic view of the Fabry-Pérot cavity antenna and the picture of our fabricated FSS used as PRS, (b) Calculated (solid lines) and measured (lines and symbols) cavity's thickness versus frequency, (c) return loss of patch antenna and FP-cavity, (d)-(e) radiation patterns in E- and H-plane for both patch antenna (red color) and Fabry-Pérot cavity (black color), respectively.

In order to illustrate the enhancement of the directivity, we have depicted in figures 3.9(d) and 3.9(e) the calculated and the measured radiation patterns in E- and H-planes for the patch antenna and for a 15 mm thick resonant Fabry-Pérot cavity, respectively at about 9 GHz. Here also, we can observe a very good quantitative agreement between simulations and measurements. The directivity of our investigated system is considerably enhanced and goes from 8 dB for the patch antenna to 20 dB for the cavity and the side lobes level of the cavity remains below -10 dB. These results show the potential application of our proposed metasurface in a Fabry-Pérot cavity for enhancing directivity of planar patch antennas. Furthermore, the study performed above in section 3.2.3 on the frequency tunability of the double-layered FSS suggests the possibility of a *frequency reconfigurable cavity* using such type of FSS as reflector. Indeed, this will be the subject of further investigations as reported in perspectives. We will now move to the second part of this chapter, which is dedicated to the study of, the so called: fishnet metamaterials.

3.4 Fishnet Metamaterials

Fishnet metamaterials (metal-dielectric-metal) were initially introduced as structures with negative refractive index with low losses at near-infrared frequencies (Zhang, 2005), and subsequently demonstrated at microwave and terahertz frequencies (where metals are almost perfect conductors) (Beruete, 2006, Beruete, 2007, Navarro-Cıa, 2008), in the far-infrared frequency range (Dolling, 2005, Valentine, 2008), and in the visible range (Dolling, 2007).

The fishnet structure also aims to be an alternative to the conventional structure consisting of a combination of SRR (Split Ring Resonators) and continuous wires, initially proposed by J. B. Pendry et al (Pendry, 1998, Pendry, 1999), fabricated and then characterized by R. A. Shelby et al at microwave frequencies (Shelby, 2001). Although the SRRs / continuous-wires based metamaerial exhibits a negative refractive index, the multilayer topology of the structure, which is illuminated at grazing incidence, remains a major disadvantage of this class of metamaterials, making them very difficult or even virtually impossible to fabricate at very high frequencies.

Further drawbacks related to physical phenomena, as already mentioned in the first chapter also limit the functioning of this structure at very high frequencies. The advantage of the fishnet metamaterial is its simplicity of manufacture, furthermore only one single layer excited at normal incidence is sufficient to exhibit a negative refractive index at the desired frequency. In the following sections, we will study two main fishnet metamaterials based on a double-sided metal grid and a perforated metal-dielectric-metal structure that exhibit a negative refractive index around 40 GHz and 85 GHz, respectively.

3.4.1 Double-Sided Metal Grid Metamaterial, Design Specifications

Figure 3.10(a) shows the schematic view of the unit cell of our investigated fishnet metamaterial. It consists of 0.5mm thick dielectric substrate (Epoxy, εr=4, tan(δ)=0,02) with 35µm thick identical metallic cross patterns printed on his both sides. Figure 3.10(b) shows our fabricated prototype, using standard optical lithography. The geometrical dimensions of the unit cell of our metamaterial *a*=3.6mm, *b*=1.5mm were chosen for functionality within the frequency band [30 GHz – 50 GHz] for the resonant frequency of about 40 GHz. The structure is illuminated with a plane wave at normal incidence with TM polarization (***E***//***z*** and ***H***//***y***) and only one layer is taken into account along the direction of wave propagation $\vec{k}$. Simulations and measurements were performed using HFSS and quasi optical free-space setup, respectively. Note that the geometry of the unit cell of our investigated structure confers to this latter a dual-polarization functioning (both TE and TM polarizations), which is a first and promising step in designing isotropic metamaterials independent from the incident polarization.

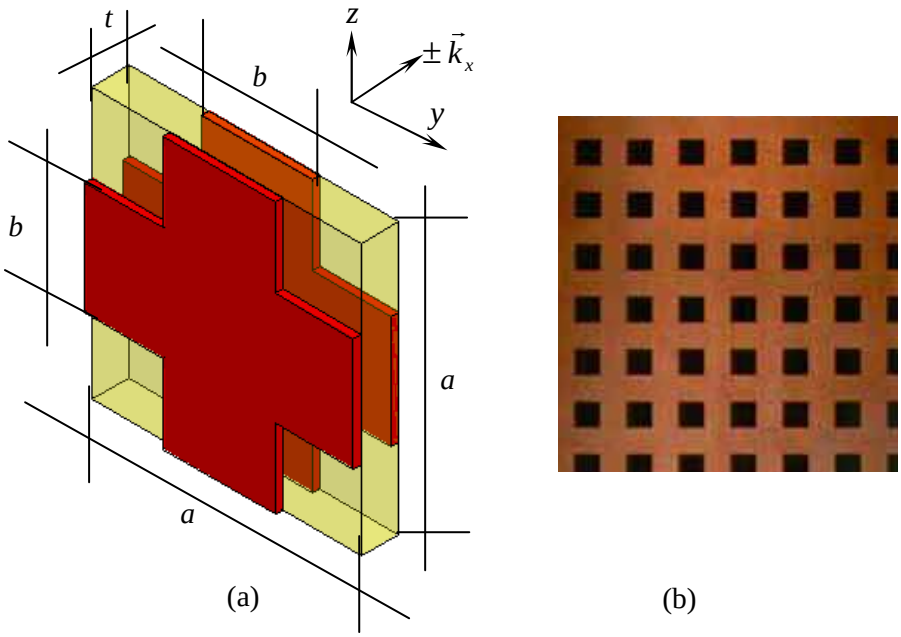

Figure 3.10: Schematic view of the unit cell of our investigated metamaterial with relevant geometrical dimensions: a=3.6mm, b=1.5mm, t=0.5mm, the experimental prototype that has been fabricated using the standard optical lithography is also shown in the left panel.

3.4.2 Simulations and Experimental Verifications

In order to demonstrate the validity of the simulation in free-space environment, a prototype sample is fabricated (see figure 3.10(b)) and tested using free-space measurement setup. Figure 3.11 shows both magnitudes and phases of the calculated and measured spectral response (transmission and reflexion) of our metamaterial, with fairly good qualitative agreement between experiments and theoretical predictions. The structure exhibits a resonance around the frequency of 40 GHz, the dip in

the reflection near 47.5 GHz for the simulation and at about 45 GHz for the measurement is due to the fact that the real part of the sample impedance z′ is equal to 1 at these frequencies, and so no reflexion is possible, a high level of transmission is then expected as illustrated below in figure 3.11(a). We think that there are two potential causes for the shift between simulations and experiments: (1) the actual dielectric constant of the circuit board material may be slightly higher than the value used in the simulations. (2) The metallic patterns on the top and bottom sides of the dielectric layer may be slightly misaligned. At these same aforementioned frequencies, the phase reflexion undergoes a jump of +180°. It should be noted that theoretically, we simulated in HFSS an infinite 2D structure which is fully illuminated by plane wave, while the fabricated prototype has more realistic and finite geometrical sizes. The number of unit cells that have been exposed to the electromagnetic radiation during the measurement is then restricted. However we arranged so that the lateral dimensions of the experimental prototype are larger (100 mm × 160 mm) than the apertures of the transmitting and receiving horn antennas (∅=50mm) which avoid diffractions at the edge of the sample.

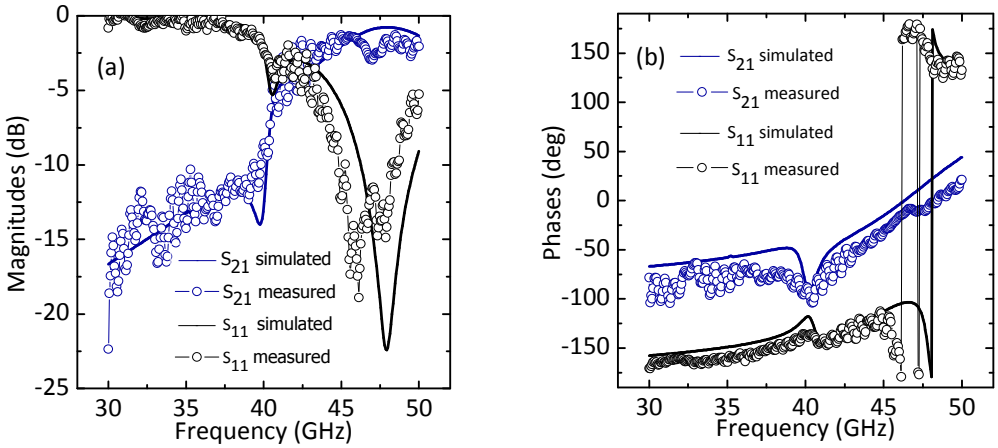

Figure 3.11: magnitudes (a) and phases (b) of the simulated (solid line) and measured (line and symbols) response (transmission and reflexion) to electromagnetic radiation incident on the double-sided metal grid fishnet metmaterial.

3.4.3 Extraction of Effective Parameters

Using the numerical retrieval procedure range (Smith, 2002), we can extract the effective parameters from the transmission and reflexion results. A particular attention has been paid in the choice of the right branch ***m***, as explained in chap.1, sec. 1.4. The extracted permeability, permittivity, wave impedance and refractive index are shown in figure 3.12. The plots show that the real part of the permeability (figure. 3.12 (a)) follows a Lorentz-like model dispersion and exhibits a resonant behaviour around 40 GHz, which leads to negative values over a very narrow frequency band: 40 GHz < f < 42.5 GHz. The imaginary part of the permeability μ" is given in the insert for a better identification of curves.

The real part of the permittivity (figure. 3.12 (b)) is negative over most of the frequency band below the plasma frequency f_p=47 GHz and exhibits a hybrid anti-resonant dispersion. The real part of the wave impedance z'=1 near 47.5 GHz for the simulation and at about 45 GHz for the measurement (figure. 3.12 (c)), which indicates a good impedance matching of the metamaterial with its host medium (the surrounding environment) at these frequencies.

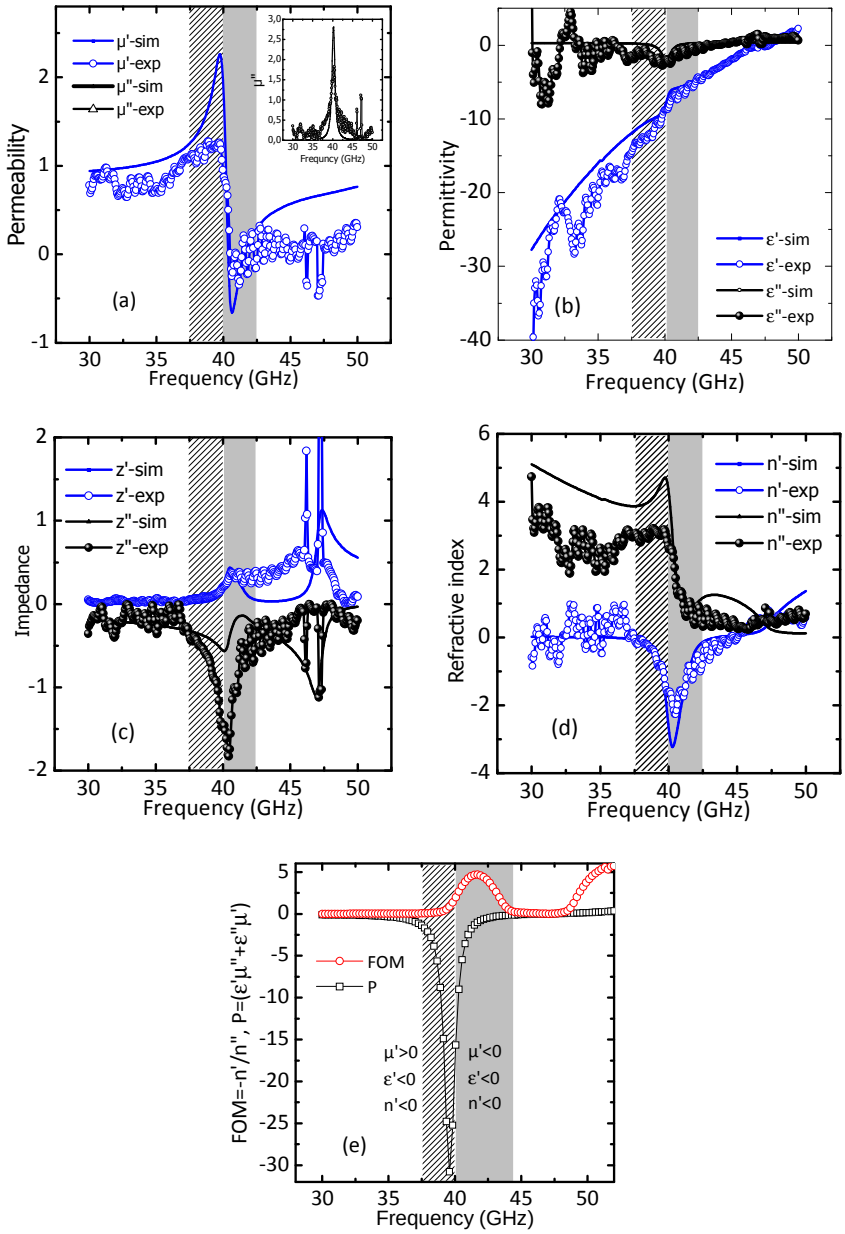

Figure 3.12: Extracted electromagnetic properties simulion (solid lines) measurements (line and symbols) of a periodic array of our double-sided metal grid fishnet metamaterial, using the simulated and measured data of figure 2.11. Real and imaginary parts of : permittivity (a), permeability (b), impedance (c) and refractive index (d). (e) FOM = (-n′/n″) and values of the expression: $P=\mu'\varepsilon''+\mu''\varepsilon'$. To guide the eye, the spectral regions corresponding to the (DNM) and (SNM) are highlighted by different shadowed areas.

The extracted real part of the refractive index is negative over a narrow frequency band from: 37.5 GHz to 42.5 GHz, including the single-negative band ($\mu'>0$ and $\varepsilon'<0$) from 37.5 GHz to 40 GHz and the double negative band ($\mu'<0$ and $\varepsilon'<0$) from 40 GHz to 42.5 GHz. Although the real part of the effective permeability μ' does not reach negative values at the low-frequency side, the negative refractive index $n'<0$ can be achieved at the whole frequency range from 37.5 GHz to 42.5 GHz (see figure. 3.12 (d)) when the condition: $P = \mu'\varepsilon'' + \mu''\varepsilon'<0$ is satisfied (Depine, 2004) (the refractive index is negative by absorption). Note that there are two frequencies on both sides of the resonant frequency (~ 40 GHz) where $\mathrm{Re}\{n_{eff}\} = -1$, which is an important criterion for sub-wavelength focusing (Pendry, 2000). A negative refractive index n' can be obtained for a sufficiently large imaginary term without requiring both μ' and ε' to be simultaneously negative, however this type of negative refractive index n' should not be considered as left handed behaviour. To achieve a negative refractive index metamaterial with low losses, i.e. a small imaginary part of the refractive index, the double negative condition is required.

The figure of merit of a metameterial is usually defined as $|\mathrm{Re}\{n_{eff}\}| / \mathrm{Im}\{n_{eff}\}$, it is mainly considered as a losses-indicator, which evaluates the "quality" of the negative refraction and this is plotted in figure 3.12(e). Basically, large values are associated with small losses, the double negative metamaterial (DNM) has a maximum FOM of 4.6 at about 41.7 GHz, contrasted to the significantly lower FOM values of the single negative metamaterial (SNM) as shown in (figure. 3.12(e)).

3.4.4 Resonance Mechanism, Dispersion Diagram, and Stability of the Spectral Response for Different Field Polarization Angles

In this section, in order to explain the mechanism of resonance, we use the common approach of describing the artificial magnetic structures as equivalent effective RLC circuit (Yan, 2008). We examined the distribution of conduction surface current density at the electromagnetic resonant frequency 40 GHz. We depict the flow of the induced conduction current J_c at the upper and lower metallic patterns in figure 3.13(a).

Obviously the two current directions are opposite to each other and these currents can produce magnetic resonance. The other resonance observed is related to the current flows near the so-called "neck-regions" along the $\vec{E}$ direction. They are opposite to those located in the slab areas, thus producing different transient charges localization in the zones where the two opposing flowing currents meet each other. As a result, a capacitance $\boldsymbol{C}$ is generated between regions A1 and B1, as well as between regions A2 and B2 denoted by arrows in figure 3.13(a). In other words, the capacitance $\boldsymbol{C}$ takes into account both the capacitance $\boldsymbol{C_n}$ of the neck pair and the capacitance $\boldsymbol{C_s}$ of the slab pair. But from figure 3.13 (a), we can see that the charges mainely accumulate near the two "neck-regions",

thus the capacitance between the two slabs primarly results from the "neck-regions" $\boldsymbol{C_n}$. A conductive current $\boldsymbol{J_c}$ starts from the point A_2 and flows through the upper metallic pattern to A_1. When $\boldsymbol{J_c}$ arrives at A_1 it runs toward the point B_1 on the lower metallic pattern in the form of displacement current $\boldsymbol{J_d}$ through the parasitic capacitor C that is between the two points of A_1 and B_1. Finally, after going through a similar way on the lower pattern, $\boldsymbol{J_c}$ and $\boldsymbol{J_d}$ form a Virtual Current Loop (VCL), which gives the impression that the structure supports free magnetic poles as in the case of a bar magnet. The structure behaves as a magnetic dipole and the negative magnetic response is then expected. From these analyses, we can draw the simple effective RLC circuit model describing our investigated fishnet metamaterial as is illustrated in figure 3.13(b). $\boldsymbol{L}$ represents the inductance arising from a parallel connexion along the electric field $\vec{E}$, between the inductance of the continuous wires denoted by $\boldsymbol{L_1}$ and that of the slab region denoted by $\boldsymbol{L_2}$ in the unit cell.

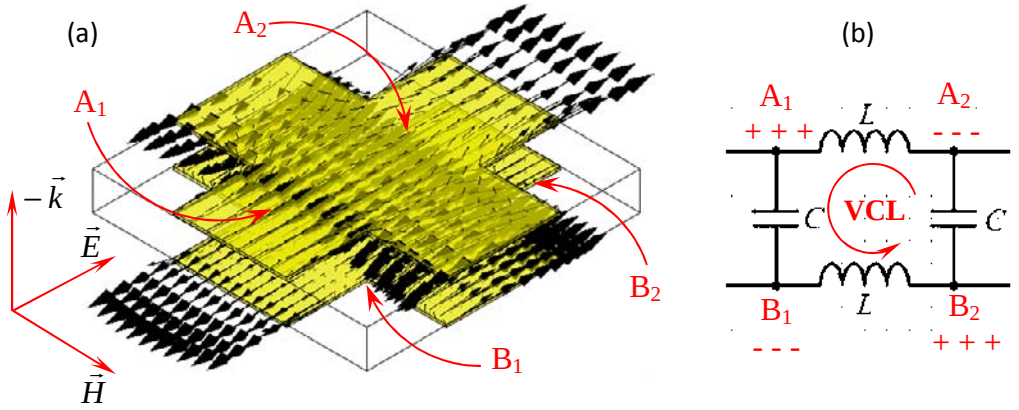

Figure 3.13: (a) The flow of the conductive surface current density on top and bottom sides of our investigated fishnet metamaterial, (b) correspondence between the RLC effective circuit elements and our fishnet metamaterial to explain the negative effective permeability μ. The arrows show the direction of the currents at the magnetic-resonance frequency. $\boldsymbol{C}$ corresponds to a parasitic capacitance through which, displacement currents flowing from one side to another of the unit cell, thus giving rise to Virtual Currents Loop (VCL). Signs related to surface charge density areas are depicted in the equivalent electric circuit.

Taking into account the effective $\boldsymbol{LC}$ circuit description, the resonance frequency of the structure $\boldsymbol{f}$ can be calculated as: $f = 1/2\pi\sqrt{LC}$. Moreover, the resonant behavior of the magnetic response of our investigated metamaterial can be explained by the common approach used to describe the artificial magnetic structures as equivalent effective $\boldsymbol{RLC}$ circuits (see figure 3.13(b)). Indeed, using circuit theory and basic electromagnetic considerations, we can determine the frequency-dependence of the effective magnetic permeability μ(ω). Indeed, assuming our investigated system shown in figure 3.13(a) illuminated by a magnetic field of the form $H=H_0e^{-i\omega t}$, and applying the Kirchhoff voltage rule, one can obtain the following expression:

$$L\frac{\partial^2 I}{\partial t^2} + R\frac{\partial I}{\partial t} + \frac{1}{C}I = -\frac{\partial^2 \phi}{\partial^2 t} = \omega^2 \mu_0 l t H_0 e^{-j\omega t}, \qquad (3.11)$$

ϕ is the external magnetic flux, $\phi=\mu_0 atH$, $\boldsymbol{\mu_0}=1.257.10^{-6}$ H.m^{-1} is the magnetic constant, ***a*** and ***t*** are the lattice constant and the thickness of the dielectric substrate of the unit cell (see figure 3.10), ***R***, ***L*** and ***C*** are the resistance, the inductance and the capacitance of the system, respectively. The obvious solution of equation (3.11) is $I=I_0 e^{-j\omega t}$, with

$$I_0 = -\frac{\omega^2 \left[\mu_0 lt / L\right]}{\omega^2 - 1/LC + i\omega R/L} H_0, \tag{3.12}$$

Having the current one can easily obtain the pair magnetic dipole moment, m = area × current = $\boldsymbol{at \times I}$, where ***a*** is the lattice constant and ***t*** is the thickness of the metal. The magnetization is given by $M = (N_{LC} / V) \times atI = (1 / V_{uc}) \times atI$, N_{LC} is the number of "*RLC*" circuits in the volume *V*, and $V_{uc}=a_E a_H a_k$ is the volume per unit cell, where a_E, a_H, and a_k are the system lattice constants along the *E*, *H* and *k* directions, respectively. Finally, using $M=\chi_m(\omega)H$, $\mu(\omega)=1+\chi_m(\omega)$, with $\chi_m(\omega)$ the magnetic susceptibility, one obtains:

$$\mu(\omega) = \mu_0 \left\{1 - \frac{1/V_{uc}\left[\mu_0 (lt)^2 / L\right]\omega^2}{\omega^2 - \omega_{LC}^2 + i\omega\gamma}\right\}, \tag{3.13}$$

with

$$\omega_{LC} = \frac{1}{\sqrt{LC}}, \quad \gamma = \frac{R}{L}$$

ω_{LC} is the magnetic resonant frequency of the system and γ is the dumping factor, representing all the losses and the scattering mechanisms. Our proposed fishnet metamaterial acts as a low frequency plasmon system above its plasma frequency. From these analyses and taking into account the effective LC circuit description of the fishnet structure, the effective magnetic resonant frequency $\boldsymbol{f_m}$ of the structure can be calculated from the relevant geometrical dimensions and the dielectric properties of the substrate of the unit cell of our investigated metamaterial, as follows (Yan, 2008):

$$f_m = \frac{1}{2\pi}\sqrt{\frac{1}{LC}} = \frac{1}{2\pi}\sqrt{\frac{1}{L_1 C} + \frac{1}{L_2 C}}, \tag{3.14}$$

where,

$$L_1 = \frac{\mu_0 a t_{metal}}{b}, \tag{3.15}$$

$$L_2 = \frac{\mu_0 b t_{metal}}{(a-b)}, \tag{3.16}$$

$$C \approx C_n = \frac{\varepsilon_0 \varepsilon_{substrat} \times \frac{b(a-b)}{2}}{2t_{substrat}}, \tag{3.17}$$

The evaluation of each lumped element was made assuming the following parameters: μ_0=1.257.10^{-6} H.m^{-1}, ε_0=8.854.10^{-12} F.m^{-1}, a=2.5mm, t_{metal}=35µm, b=0.6mm and $\varepsilon_{substrate}$ about 2.17, we calculate C ~ 0.8pF, L_1 ~ 100 pH and L_2 ~ 30pH, and find a resonant frequency of about 37 GHz, which is a rather good prediction. One can see that about 40 GHz was predicted by the simulation and confirmed by the experiment, this indicates that the LC circuit model can rougly describe the electromagnetic resonance of the fishnet structure.

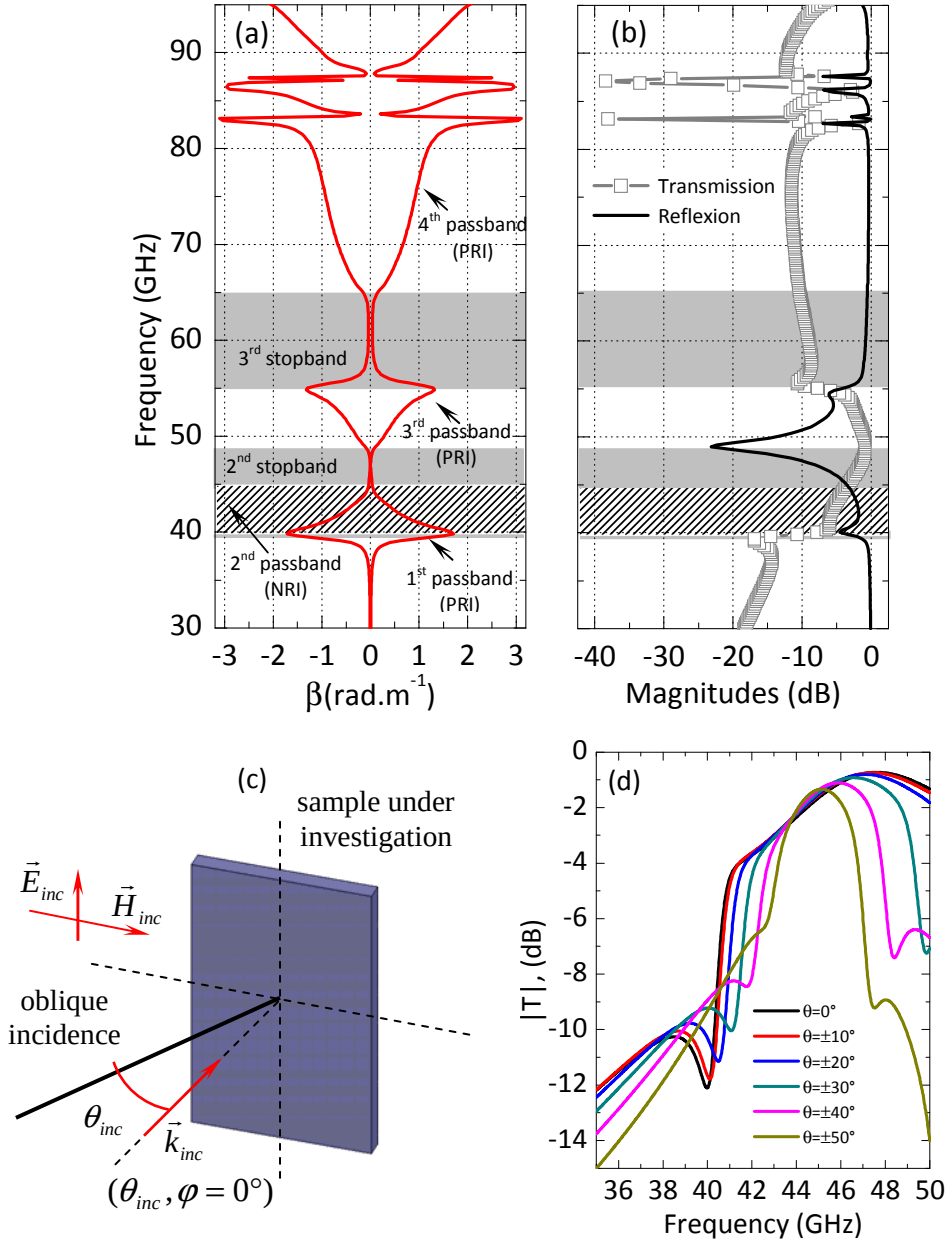

Figure 3.14: (a) Dispersion diagram on the contour ΓX (normal incidence) of the first Brillouin region, (b) theoretical magnitudes of transmission S_{11} and reflection S_{11} spectra of the double-sided grid metallic fishnet metamaterial, (c) illustration of the scenario used for the angular study, (d) transmission magnitude of the investigated fishnet metamaterial for different incident angles (θ_{inc}).

The dispersion diagram on the contour ΓX of the first Brillouin region calculated from the simulated complex reflection and transmission coefficients is depicted in figure 3.14(a), where β_z means a propagation constant in the z-direction in the metamaterial. The plots exhibit a negative refractive index (NRI) passband that corresponds to about 40 GHz to 42.5 GHz (shaded area on the dispersion diagram and transmission and reflexion spectra), characterized by a negative phase velocity $\omega/k<0$, which is one of the necessary signatures of LHM.

At the end of the 2nd passband (NRI), the structure exhibits a stop-band from 42.5 GHz to 47.5 GHz (highlighted area), where the refractive index is zero and the evanescence is negligible. At the beginning of the positive refractive index (PRI) passband, the transmission coefficient (see figure 3.14(b)), reaches its maximum value at about 50 GHz, and then decreases in amplitude from 55 GHz and continue throughout the 4th (PRI) passband, which begins at about 65 GHz. The sudden drop level of the transmission around 83 GHz and 87 GHz respectively, corresponds to the absence of the right-hand modes.

The influence of the incident field polarization angle has been also analyzed. Figure 3.14(c) shows the typical scenario used for the oblique incidence study of a our structure. The transmitting and receiving antennas remain fixed, while the sample under investigation is rotated. The transmission magnitude of the fishnet metamaterial has been calculated and depicted in figure 3.14(d) for different incident field $\vec{E}_{inc}$ polarization angle θ_{inc}.

When the incident angle varies from 0° to ± 50°, the sensitivity of the metamaterial results in a shift towards higher frequencies of the spectral signature characterizing the negative refraction zone. This shift is accompanied by a more selective behavior around the frequency of the impedance matching, located beyond the electromagnetic resonant frequency around 47.5 GHz for the simulation. One can see that the frequency of the impedance matching moves towards low frequencies from 47.5 GHz to 44 GHz approximately, when the incident angles goes from 0° to ± 50° as illustrated in figure 3.14(d).

Globally, our investigation reveals a very interesting sensitivity of the frequency response to the incident angle of the exciting electromagnetic wave, particularly in the frequency range of the negative refractive index (where the electromagnetic properties are not dramatically affected and remain substantillay unchanged). This can be very potential and promising for oblique-incidence applications and for high selectivity filtering applications.

In conclusion, we have investigated a negative refractive index metamaterial in both simulations and experiments, and a very good agreement has been reported. We will now move to the study of a variant of the fishnet structure, which is the holes-array metamaterial.

3.5 Holes-Array Metamaterials

3.5.1 Design Specifications, Simulations and Experimental Verifications

In this section, we propose to investigate a variant of the double-sided metal grid metamaterial that has been studied in the previous section and which consists of a holes-array metamaterial. This structure has been widely investigated in scientific literature at millimeter wavelengths and in the terahertz regime (Beruete, 2009, Kuznetsov, 2009). The unit cell of our proposed negative refractive index holes-array metamaterial is shown in figure 3.15(a). It consists of dielectric substrate coated on both sides with 35 µm thick copper and holes with a diameter ∅ of 1.9 mm are achieved mechanically by a milling machine entirely through the substrate with a periodicity of a=2.5 mm along x and y directions.

The commercial Isoclad-Arlon printed circuit board, which has a thickness $\boldsymbol{t}$ of 100 µm, a moderate relative permittivity ε_r of about 3.16 and a low loss tangent ($\tan\delta$) of about 0.009, is used for fabrication. The chosen PCB has a good mechanical flexibility due to its low thickness, which is very potential for conformity applications like radomes. The structure operates obviously with a dual-polarization TE (E_x, H_y, k_z) and TM (E_y, H_x, k_z). Due to the periodic structure, only one unit cell is simulated in HFSS, and only one single layer of the metamaterial is taken into account along the direction of propagation k_z.

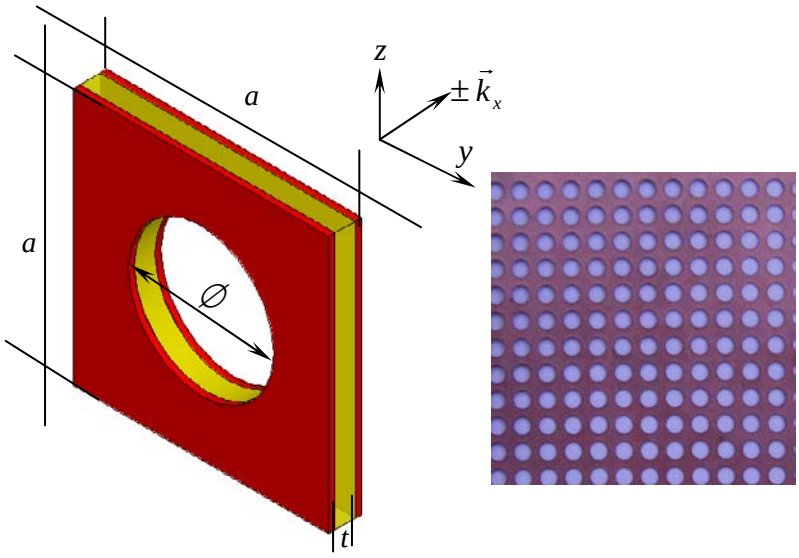

(a) (b)

Figure 3.15: (a) Schematic view of the unit cell of our invetigated holes-array fishnet mtamaterial with the relevant gometrical dimensions $\boldsymbol{a}$=2.5 mm, ∅=1.9 mm, $\boldsymbol{t}$=0.1 mm, (b) image of our manufactured prototype.

Our proposed metamaterial is very simple to manufacture without using traditional lithography techniques which is a major advantage for a transfer to industrial applications. Figure 3.16 shows the magnitudes and phases of the simulated and measured transmission and reflexion coefficients. From

our characterization results, we will find that the electromagnetic resonance wavelength λ is much larger than the size of the unit cell t (thickness of the metamaterial along the direction of propagation z) (λ/t=35), the effective medium model is then successfully employed. Although the sizes of the unit cells of our metamaterial along the x and y directions are not much smaller than λ, diffraction still cannot occur.

The reason is that electromagnetic waves are not propagating along the x and y directions (Yan, 2008). The photograph of our manufactured prototype is shown in figure 3. 15(b). Using HFSS, which is full wave commercial software simulator based on the finite element method we calculated the magnitudes and phases of the transmission S_{21} and reflexion S_{11} coefficients. Experiments have been done using a non-destructive free-space setup, based on a vector network analyser (AB Millimetre™) with transmitting and receiving horn antennas. The result of our characterization is depicted in figure 3.16. The structure has a resonance around 85 GHz and exhibits a good impedance matching (z=1) at about 107 GHz for the simulation and near 104 GHz for the measurement (see figure 3.16(a)). At these frequencies the reflexion undergoes a phase jump of +180°. The dip in the phase of transmission around 85 GHz indicates the presence of a negative refractive index band (see figure 3.16(b)).

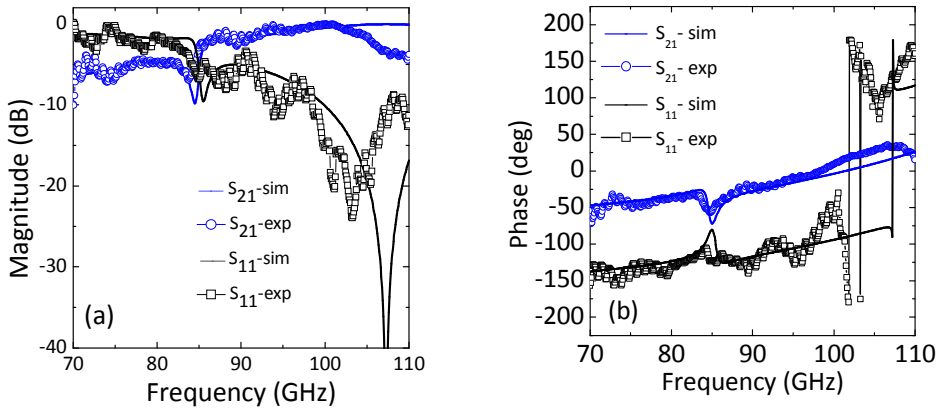

Figure 3.16: magnitudes (a) and phases (b) of the simulated (solid line) and measured (line and symbols) response (transmission and reflexion) to electromagnetic radiation incident on the holes-array fishnet metmaterial.

3.5.2 Extraction of Effective Parameters

Using the S-parameters retrieval method (Smith, 2002), the complex effective permeability μ, permittivity ε, wave impedance z and refractive index n have been extracted in figure 3.17. The permeability shows a resonant Lorentz dispersion (figure 3.17(a)), while the permittivity is analogous to the Drude dispersion of the continuous wires (figure 3.17(b)). The negative permeability is the result of a strong resonance response to an external magnetic field while negative permittivity can be achieved by either plasmonic or a resonance response to an external electric field. Around the

frequency of resonance, the real part of the effective wave impedance z' is real positive with very low imaginary parts, which attests the passivity of the structure (see figure 3.17(c)).

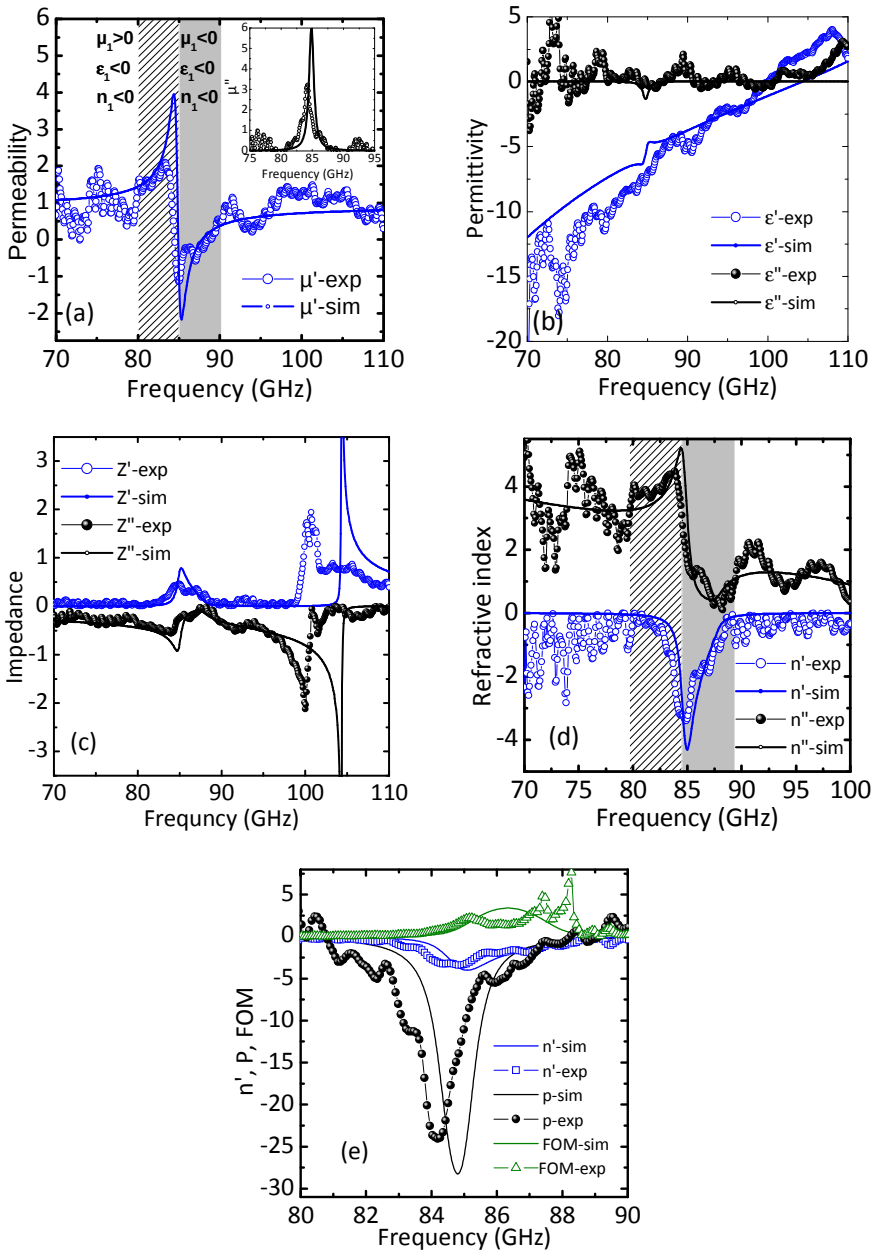

Figure 3.17: Extracted electromagnetic properties of a periodic array of our double-sided metal grid fishnet metamaterial unit cell, using the simulated and measured data of figure 3.16. Real and imaginary parts of: permittivity (a), permeability (b), impedance (c) and refractive index (d). Simulated (solid lines) and measured (lines+symbols) curves of real part of the refractive index n′, P=$\mu'\varepsilon''+\mu''\varepsilon'$ and FOM=(-n′/n″) (e). To guide the eye, the spectral regions corresponding to the (DNG) and (SNG) are highlighted by different shadowed areas.

According to what we have mentioned in the previous section, the real part of the effective wave impedance $\boldsymbol{z'}$= 1 near 107 GHz in the simulation and at about 104 GHz in the measurement, which confirms a good impedance matching between the structure and its host medium. Our extracted effective refractive index is negative over a frequency band from 80 GHz to 90 GHz, which includes

both Single NeGative metamaterial (SNG: $\mu' > 0$ and $\varepsilon < 0$) from 80 GHz to 85 GHz and double NeGative metamaterial (DNG: $\mu' < 0$ and $\varepsilon < 0$). The negative refractive index is achieved when the condition $P = \mu'\varepsilon'' + \mu''\varepsilon' < 0$ is satisfied, as clearly shown in figures 3.17(d) and 3.17(e), respectively. Several prototypes have been fabricated for different operating frequencies: 35 GHz, 55 GHz, 85 GHz and 94 GHz, which leads to cover a very broad spectral range of functioning, depending on the targeted application. At about 86.3 GHz, the double negative metamaterial (DNM) has a maximum FOM of 3.5 in simulation and about 1.4 GHz in measurement, contrasted to the significantly lower FOM values of the single metamaterial (SNM) as shown in figure 3.17(e).

3.5.3 Stability of the Spectral Response for Different Field Polarization Angles and Dispersion Diagram

The influence of the incident angle θ_{inc} on the stability of the response of our investigated holes-array fishnet metamaterial has been studied numerically. The spectral response of our metamaterial is very sensitive to the incident angle θ_{inc}, as illustrated in figure 3.18(a). Indeed, at ±10°, an additional peak appears around 105 GHz and splits into new peaks, which move gradually toward lower frequencies as the angle of incidence increases.

The resonance at 85 GHz that characterizes the negative refractive zone is not modified up to an incident angle of ±20°. Beyond this angle of incidence, the negative refractive index signature is significantly affected and completely disappears for an incident angle of about ±50°. In other words, it seems that the structure supports higher order modes that might be very useful for multiple-frequency band applications. The origin of this anomaly still remains unknown.

The theoretical and experimental first mode dispersion diagram on the ΓX contour of the first Brillouin zone of our studied metamaterial is depicted in figure 3.19. The structure exhibits a left-handed propagation, characterized by a negative slope ($d\omega / dk < 0$) within the frequency range 85 GHz - 90 GHz (highlighted regions in figure 3.19) which demonstrates that the phase velocity and group velocity are anti-parallel.

The structure also exhibits a band gap between 90 GHz and 105 GHz approximately in simulation (right horizontal dashed regions in figure 3.19) and between 90 GHz and 98 GHz approximately in measurement (left vertical dashed region in figure 3.19). Beyond the experimental and theoretical frequencies of 98 GHz and 105 GHz respectively, which correspond to the plasma frequencies of the structure, the metamaterial allows a right-handed propagation of electromagnetic waves.

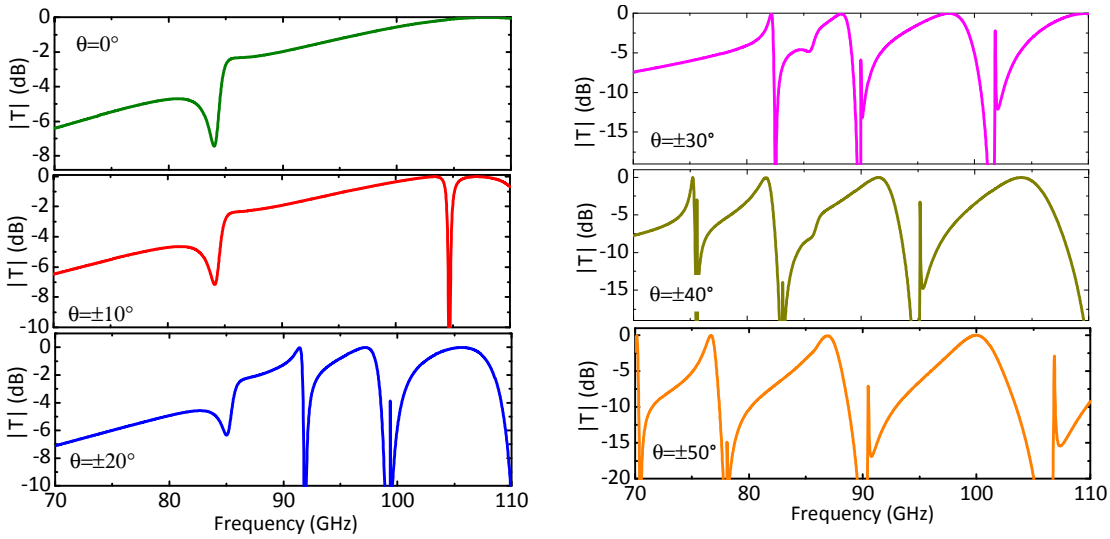

Figure 3.18: Transmission magnitudes of the investigated holes-array metamaterial for different incident angles (θ_{inc}) from 0° to ±50°.

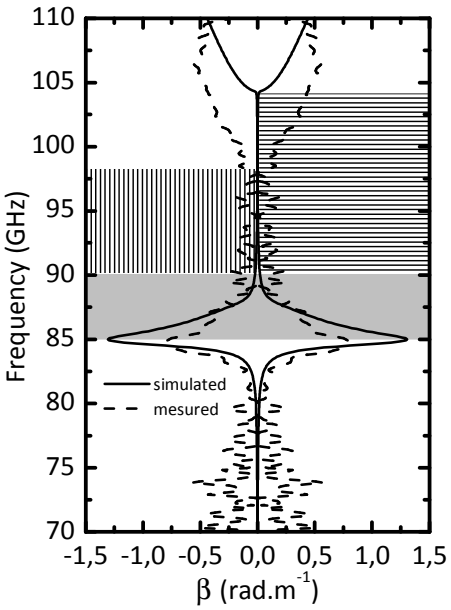

Figure 3.19: Simulated (solid lines) and measured (dashed lines) first-mod dispersion diagram on the contour ΓX of the first Brillouin zone of the holes-array fishnet metamaterial.

3.5.4 Demonstration of the Negative Refraction

In order to demonstrate the existence of a frequency band where the refractive index is negative, and give a direct image of the negative refraction of the electromagnetic wave for the holes-array fishnet metamaterial, a two dimensional metamaterial prism is designed for simulation and composed by stacking 12 to 2 metamaterial unit cells from right to left. Both simulations and experiments have been performed on the prism characterized by a refractive index that reaches a maximum negative value of about -4 around 35 GHz.

Using the full wave commercial code based on the Transmission Line Matrix (TLM) CST Microstripes, we have depicted in figure 3.20(a) the calculated electric field distribution at the resonant frequency of 35 GHz. The simulation results demonstrate the negative refractive behaviour. Indeed, the refracted beam, which corresponds to the E_z-field, propagates toward a left-handed region with a negative refraction angle of about -15° (in other words, the beam is transmitted in the same side than the incident beam, with respect to the normal axis **Δ**).

One can clearly observe that the magnitude of the Electric field is considerably enhanced within the metamaterial-based stacked prism, which demonstrates the amplification of evanescent modes. Figure 3.20(b) shows the experimental prototype that has been manufactured and tested using the experimental setup depicted in figure 3.20(c).

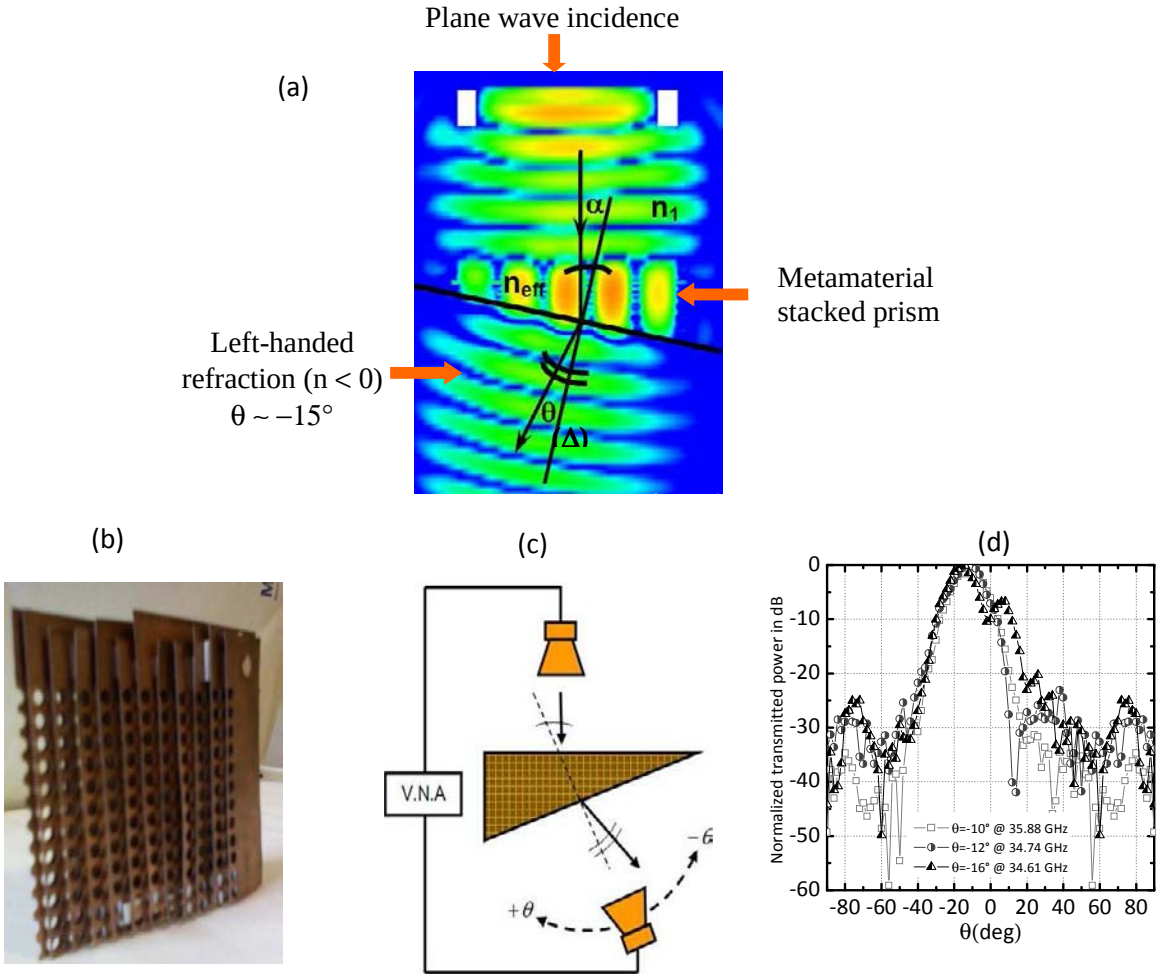

Figure 3.20: (a) stacked-metamaterial-prism-based negative refraction simulation at 35 GHz, (b) the fabricated fishnet-based microstructured prism, (c) normalized transmitted power measured through the prism for different frequencies with a beam steering to the negative angles.

The results of the measurement show a beam steering toward negative angles, depending on the operating frequency within the negative refraction region. We have obtained refractive angles of about -10°, -12°, and -16 ° for operating frequencies of about 35.88 GHz, 34.74 GHz, and 34.61 GHz respectively.

3.5.5 Influence of the Holes's Geometry on the Spectral Response and the Refractive Index

In order to demonstrate that the geometry of holes is of only secondary importance and that the dielectric and magnetic functions follow the same tendencies, we considered a fishnet structure with square holes instead of circular one, as illustrated in figure 3.21(a). The simulated transmission curves of the structures are presented in figure 3.21(b). Globally, the transmission properties remain substantially unchanged as observed by other authors (Dolling, 2007), with a frequency shift of the resonance from 84.5 GHz for a metamaterial with circular holes to 86 GHz for a metamaterial with square holes. Moreover, after the numerical extraction of the effective refractive index (see figure 3.21(c)), we find that the minimum of the refractive index is not considerably affected by the geometry but primarily depends on the dielectric losses. This results in a better flexibility in dimension tolerances during the fabrication steps. Further simulations have been performed in order to obtain a tunability effect on the spectral response of our metamaterial, by filling the holes-array with a dielectric substrate whose relative permittivity ε_r varies from 1 to 3. Indeed, as clearly shown in figure 3.21(d), the resonant frequency varies from 85 GHz to 80.9 GHz, when the relative dielectric permittivity ε_r goes from 1 to 3.

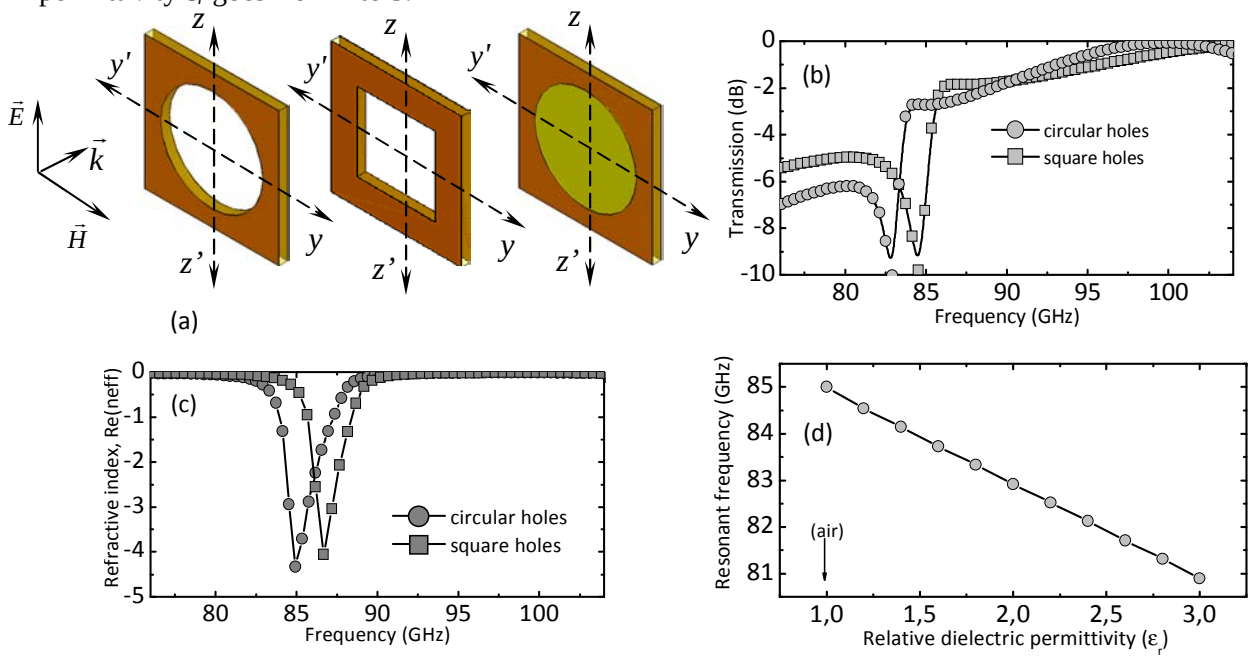

Figure 3.21: Unit cells of different investigated metamaterials, (a) calculated transmission magnitudes, (b) calculated refractive index for different shapes of holes (circular and square), (c) variation of the resonant frequency of the circular holes-array metamaterial, when the holes are filled with a dielectric substrate whose relative permittivity ε_r varies from 1 to 3.

3.6 Conclusion

In conclusion, we have investigated composite metal-dielectric metamaterials at microwave frequencies. Calculations based on the finite element method have been performed in order to predict the spectral response of our proposed structures. Prototypes have been fabricated using both the classical optical lithography and the mechanical machining technique and measurements have been carried out using a non-destructive free space setup based on a vector network analyzer and horn antennas, in order to validate the numerical predictions. Good agreements have been reported between simulations and experiments. One of our proposed structures has been used as a partially reflecting surface in a Fabry-Perot cavity in order to enhance the directivity of printed patch antennas. The negative refractive index exhibited by our structures (fishnet metamaterials), has been calculated and measured, and the left handed behaviour has been demonstrated numerically and experimentally in the last part of the chapter.

Chapter 4

All-Dielectric (AD) and Composite (Metal-Dielectric) Metamaterials for Terahertz Applications

4.1 Introduction

This chapter is dedicated to the study of metamaterials in the terahertz frequency range. This frequency band [0.1 THz – 10 THz] that allows bridging the gap between microwaves and optical frequencies remained inaccessible for long times and rarely used for a lack of suitable sources and detectors. But recently, due to the advances of the semiconductor technology, scientists have fabricated in laboratories inexpensive lasers that emit in terahertz regime and operating at temperature close to the room temperature, which constitutes a promising breakthrough for many applications. In the first part of this chapter, we focused on a new category of metamaterials, the so called: All Dielectric (AD) metamaterials.

The conventional method which consists to have sub-wavelength metallic patterns in a dielectric matrix is very difficult to fabricate, particularly for unit cells of complex geometry with submicron or nanoscale sizes. Another drawback of the conventional approach is the anisotropy of theses metallic patterns, which makes the desired electromagnetic properties only available in certain directions. We will consider a new approach based on the Mie resonances with high relative dielectric permittivity (ε_r) particles, as an alternative way which offers a simpler route for achieving low-loss and homogenous metamaterials.

Two main different structures have been investigated, the first one consists of a series of Strontium Titanate ($SrTiO_3$) rods-arrays, characterized by high relative dielectric permittivity and low loss level at room temperature (ε_r= 300, tan(δ)=0.025 at 0.25 THz) and which exhibit an artificial magnetism that leads to negative magnetic permeability, i.e. $Re(\mu_{eff})<0$. The spectral response of our metamaterials have been tuned in frequency by changing the temperature in a cryostat. Our second investigated AD metamaterials, consists of a series of Titanium dioxide-based (TiO_2) disordered and polydisperse (in size and shape) micro-particles layers that have been fabricated and characterized at terahertz frequencies and exhibit a negative effective permeability.

In the second part of this chapter, we investigate the Extraordinary Optical Transmission (EOT) effect, induced in sub-wavelength apertures-based metamaterials. We have also investigated both single and double layer fishnet metamaterials, which have been designed, fabricated and characterized for an operating frequency of about 1 THz. Standard optical lithography, laser micromachining technique and chemical synthesis have been used in order to fabricate our experimental prototypes and Terahertz Time Domain Spectroscopy has been used for the measurements.

4.2 Ferroelectric Materials

Ferroelectric materials are dielectrics with permanent electric dipole moment, which exists even if an external electric field is not applied. The moment per unit volume corresponds to the polarization $\vec{P}$ of the material. In a ferroelectric, this polarization can be reversed by applying a strong external electric field in the opposite direction. The polarization depends on the temperature and disappears beyond a critical Curie temperature $\boldsymbol{T_c}$. For temperatures above the critical temperature "$\boldsymbol{T_c}$", the ferroelectric is in paraelectric state, with no spontaneous polarization as shown in figure 4.1(a). There are two types of ferroelectric materials : displacement and order-disorder ferroelectrics. The Strontium Titanate material ($SrTiO_3$) that we have used in our research is considered as displacement ferroelectric materials, which posseses a Perovskite ABO3 structure that changes its symmetry during the ferroelectric-paraelectric phase transition.

At high temperature "$\boldsymbol{T > T_c}$", the material is in a paraelectric cubic phase. The Titanate ion $\boldsymbol{Ti^{4+}}$ occupy the center of the unit cell, the Stontium cations Sr^{2+} are located at the summits of the cube and the oxygen ions $\boldsymbol{O^{2-}}$ are located at the center of each face, as illustrated in figure 4.1(b). For temperatures below the critical Curie temperature "$\boldsymbol{T_c}$", a tetragonal distortion of the cell occurs, and the oxygen octahedron elongates in the direction of the *c*-axis and instead of the equilibrium state, two different positions are possible for the $\boldsymbol{Ti^{4+}}$ ion, shifted in one direction or another with respect to the midplane of the cell as illustrated in figure 4.1(c). The shift of $\pm\ \boldsymbol{u_0}$ up or down along $\boldsymbol{c}$ axis corresponds to the two states of spontaneous polarization $\pm P_s$, in this case the material is in the ferroelectric phase. As mentioned above, materials typically demonstrate ferroelectricity only below a certain phase transition temperature, called the Curie temperature, $\boldsymbol{T_c}$, and are paraelectric above this temperature.

Most materials are polarized linearly by an external electric field; nonlinearities are insignificant. This is called dielectric polarization. In the paraelectric phase ($\boldsymbol{T > T_c}$), a more pronounced nonlinear polarization is observed. The electric permittivity, corresponding to the slope of the polarization curve, is thereby a function of the external electric field. In addition to being nonlinear, ferroelectric materials ($\boldsymbol{T < T_c}$) demonstrate a spontaneous (zero field) polarization (see figure 4.1(d)). The distinguishing feature of ferroelectrics is that the direction of the spontaneous polarization can be reversed by an applied electric field, yielding a hysteresis loop. $\boldsymbol{SrTiO_3}$ is known to exhibit a high dielectric tunability in the THz range with a reasonable level of dielectric losses ($\tan(\delta)$~0.025 at 0.25 THz) (Němec, 2005). The temperature dependence of the relative permittivity of the $SrTiO_3$ thin single Crystal in the paraelectric phase usually obeys the Curie-Weiss law in a broad temperature range (Kužel, 2008):

$$\varepsilon_r(T) = \frac{C}{T - T_c}, \tag{4.1}$$

where C is a material-specific Curie constant, T and T_c is absolute and Curie temperatures, respectively, measured in Kelvins. The law predicts a singularity in the temperature-dependence of the relative permittivity $\varepsilon_r(T)$ at $T = T_c$. Above this temperature the ferroelectric loses its intrinsic polarization and becomes paraelectric.

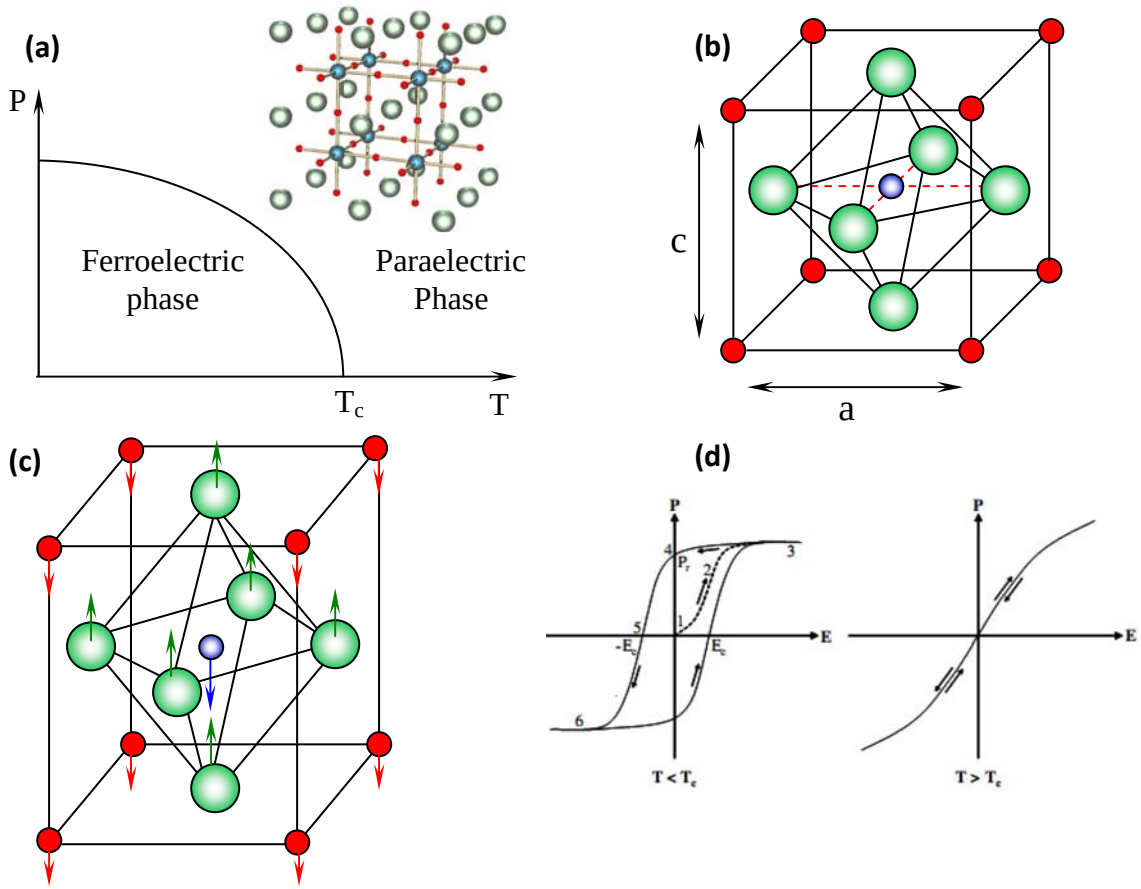

Figure 4.1: (a) evolution of the spontaneous polarization P of a ferroelectric as a function of temperature with the structure of $SrTiO_3$ in the insert. The red spheres are oxygens, blue are Ti^{4+} cations, and the green ones are Sr^{2+}, (b) at high temperature, (c) below the critical Curie temperature "Tc". The dashed square indicates the available positions for the Ti^{4+} ion, in the paraelectric phase (b), there is only one equilibrium position located in the central plane of the cell. In the ferroelectric phase (c), there are two positions on either side of the mid-plane. (d) Polarization versus external electric field for the two possible phases: ferroelectric and paraelectric.

4.3 Negative Effective Permeability induced in All-Dielectric Strontium Titanate ($SrTiO_3$) Rods-Array Metamaterials

In recent years, All-Dielectric (AD) metamaterials based on the Mie resonances, have been the subject of intense research activity. Indeed, AD metamaterials are usually based on magneto-dielectric (Holloway, 2003), ferroelectric (Vendik, 2004), polaritonic (Wheeler al., 2005) spheres, and

ferroelectric rods (Huang, 2004), respectively. Zhao et al. (Zhao, 2008) demonstrated experimentally at microwave frequencies a negative magnetic permeability in a three-dimensional dielectric composite metamaterial based on high relative dielectric permittivity cubic particles of $Ba0.5Sr0.5TiO_3$ (BST) coated in Teflon. In another paper of Zhao et al. (Zhao, 2008), in order to demonstrate the isotropy of the negative permeability, the authors used a composite material based on BST-MgO to fabricate the cubes and the host medium remains Teflon. Vendik et al. (Vendik, 2006, Vendik, 2008, Vendik, 2009) in their works at microwave frequencies investigated analytically and numerically a periodic composite medium consisting of two lattices of different dielectric spherical particle.

Indeed, the authors showed that effective isotropic double negative media (DNG) can be realized in the frequency region where resonance of TM mode in one kind of particles and TE mode in another kind of particles are presented simultaneously, under the conditions of concentration and particle size ration. Moreover, Peng et al. (Peng, 2007) observed experimentally a left-handed behaviour in an array of standard dielectric resonator. More recently, Shibuya et al. (Shibuya, 2008) in their theoretical works, predicted the same left handed behaviour at terahertz frequency range, using TiO_2 cube arrays, and Lepetit et al. (Lepetit, 2009) have measured a negative refractive index in all-dielectric metamaterial at microwave frequency range.

4.3.1 Periodic Medium of Our Investigated Metamaterial

This section covers the works carried out in collaboration with the group of Professor Petr Kužel, from the Institute of Physics of Prague in Czech Republic. The investigated metamaterials consist of a series of rods, made of $SrTiO_3$ (STO) thin single crystal plate characterized by high dielectric relative permittivity with reasonable low level of dielectric losses at room temperature (ε_r= 300, tan(δ)=0.025 at 0.25 THz) as depicted below in figure 4.2 (Němec, 2005).

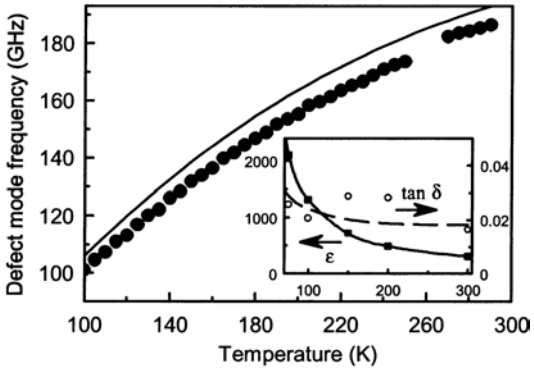

Figure 4.2: Evolution of the measured (symbols) and the simulated (solid line) defect mode frequency. Inset, temperature dependence of the permittivity (ε) and the loss tangent (tan δ) of a SrTiO3 single crystal at 0.2 THz measured by THz time-domain spectroscopy, (Points) measured values (solid line) analytical fits of the data, as reported by (Němec, 2005).

First, plane parallel wafers of STO were prepared by mechanical polishing with a thickness of $\boldsymbol{t}$ = 52 μm, the thickness of some samples was reduced down to $\boldsymbol{t}$ = 22 μm by a subsequent wet etching in Orthophosphoric acid (H_3PO_4). A series of grooves with a width d and period P (structure A: $\boldsymbol{d}$ = 33 μm, $\boldsymbol{P}$ = 75 μm, and $\boldsymbol{t}$ = 52 μm; and structure B: $\boldsymbol{d}$ = 28 μm, $\boldsymbol{P}$ = 96 μm, and $\boldsymbol{t}$ = 22 μm) were drilled in the wafers by femtosecond laser micromachining. The grooves were directly etched by a Yb:KGW 1.03 μm femtosecond laser at Alphanov technological center (http://www.alphanov.com/uk/).

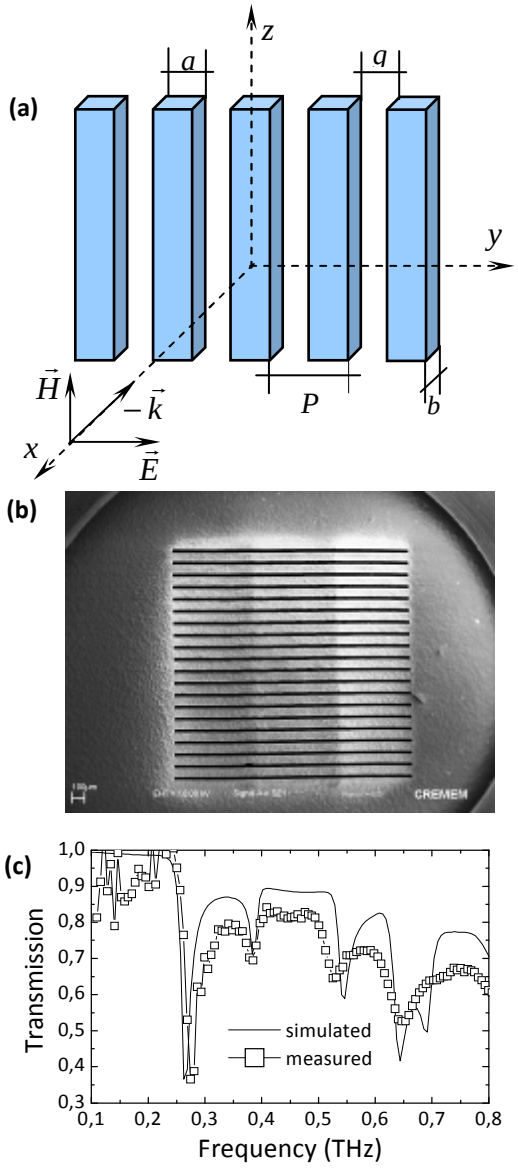

Figure 4.3: (a) Schematic view of our All-Dielectric-Metamaterial with the appropriate fields polarization and the geometrical dimensions (structure A: a=33μm, P=75μm, and b=52μm; and structure B: a=28μm, P=96μm, and b=22μm). (b) Scanning Electron Microscope Image (SEMI) of our investigated metamaterial. (c) Simulated and measured magnitude of transmission.

The ultrafast regime offers an enhanced control in producing the desired microstructures as laser energy absorption occurs on a time scale much faster than heat transport and electron-phonon

coupling. The resulting patterns covered areas up to 2.5×3 mm² and the technological challenge was to fabricate a large area pattern in a very thin brittle material. Indeed, one can note the high aspect ratio between thickness and area. Figures 4.3(a) and 4.3(b) show a schematic representation and a Scanning Electron Microscope Image (SEMI) of our investigated metamaterial, respectively. The metamaterial is illuminated by plane wave at normal incidence with the appropriate polarization of the electric and magnetic fields ($\vec{E} \perp$ rods and $\vec{H} /\!/$ rods), as depicted in figure 4.3(a). Our metamaterials are basically birefringent, and only one layer is taken into account along the direction of propagation $\vec{k}$.

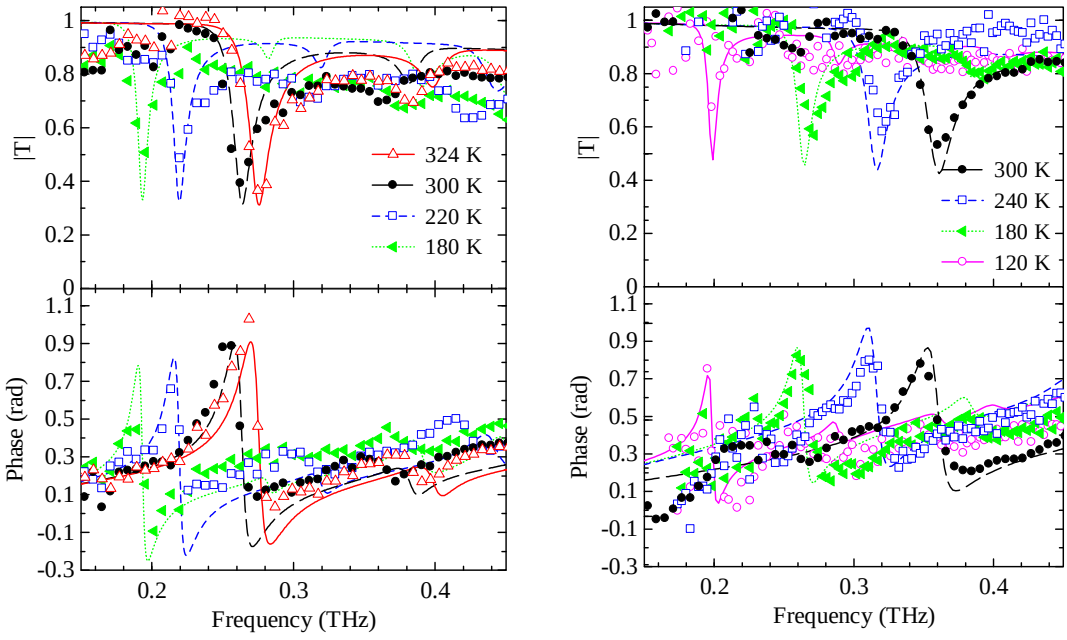

Figure 4.4: Magnitudes and phases of our metamaterial, calculations (solid lines), measurements (lines and symbols), using the Transfer Matrix Method (TMM) and Terahertz Time Domain Spectroscopy (THz-TDS), respectively for different values of the temperature, (a) structure A, (b) structure B.

The modes considered here are transverse electric TE_{mn}, since the magnetic field of the incident wave is polarized along the axis of the resonators. A series of Mie resonances occur on the spectral response of the metamaterial at 0.263THz, 0.383THz, 0.547THz, 0.643THz and 0.691THz, respectively (see figure 4.3(c)). This resonant behavior is closely connected to the high value of the relative permittivity of STO at room temperature (ε_r= 300). Indeed, high values of permittivity are necessary for supporting resonances in the particles (Vendik, 2004), thus providing to the particles sizes which are considerably less than the wavelength in the surrounding medium. The effective medium is then successfully employed. The dielectric resonators to the photons are considered as the counterparts of potential wells in quantum systems, which confine electrons. For further details related to the Mie theory, see appendix B. Figures 4.4(a) and 4.4(b) show the calculated and measured

magnitudes and phases of transmission coefficient for the structures A and B, using HFSS and Terahertz Time Domain Spectroscopy (THz-TDS), respectively, for different values of the temperature. A fairly good quantitative agreement is reported between theory and experiment. These characterizations were done in a cryostat available in Prof. Kuzěl's group.

The spectral response and the effective properties of our metamaterials can be tuned by a temperature control of the permittivity of $SrTiO_3$ over a broad spectral range from 0.18 THz to 0.29 THz for the structure A when the temperature goes from 180°K to 324°K, and from 0.2THz to 0.36THz for the structure B when the temperature goes from 120°K to 300°K, thus leading to ~ 33% and ~ 55% of tunability, respectively. Indeed, according to equation (4.1) when the temperature increases the relative dielectric permittivity of the STO decreases, the spectral response of our investigated metamaterial is then shifted towards high frequencies. Note that it was the first demonstration of tunable spectral response in the THz range. Our present work has been the subject of publications of the following journal articles (Němec, 2009, Yahiaoui, 2011).

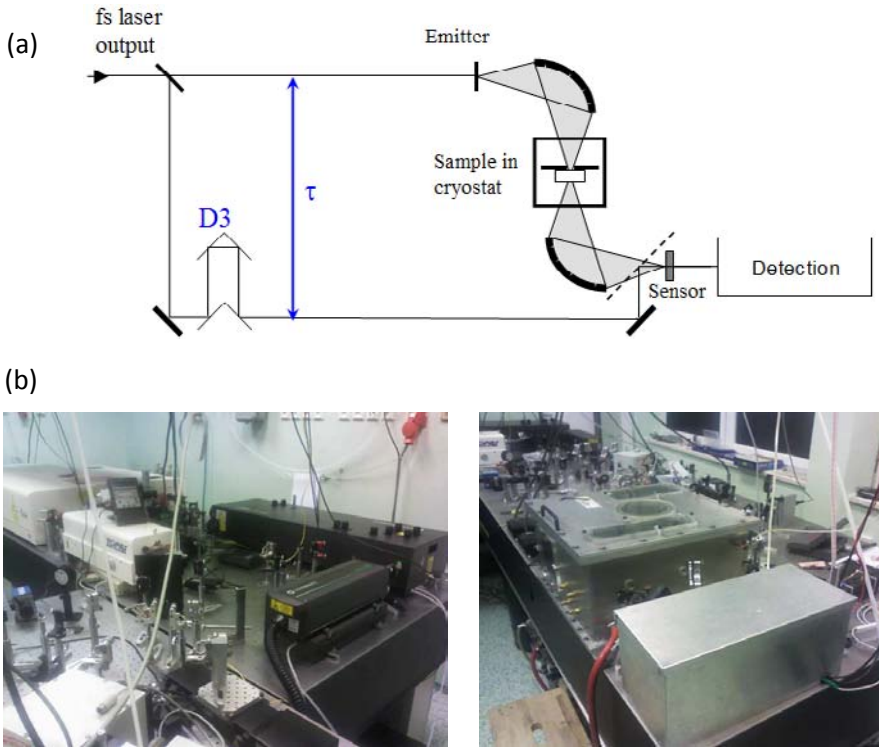

Figure 4.5: (a) Schematic view, and (b) real time image of the experimental THz-TDS setup used for measurements at the institute of physics of Prague in the Czech Republic.

Figure 4.5 (a) and 4.5 (b) show the schematic view and real time images of the experimental setup, respectively that has been used in order to carry out measurements at the institute of physics of Prague in the Czech Republic. The setup is based on the electro-optic emission and detection, as explained in chapter 2, section 2.6.1. The frequencies where the Mie resonances occur depend strongly on the optical thickness of the rods, i.e. the relative permittivity ε_r and the geometrical dimensions.

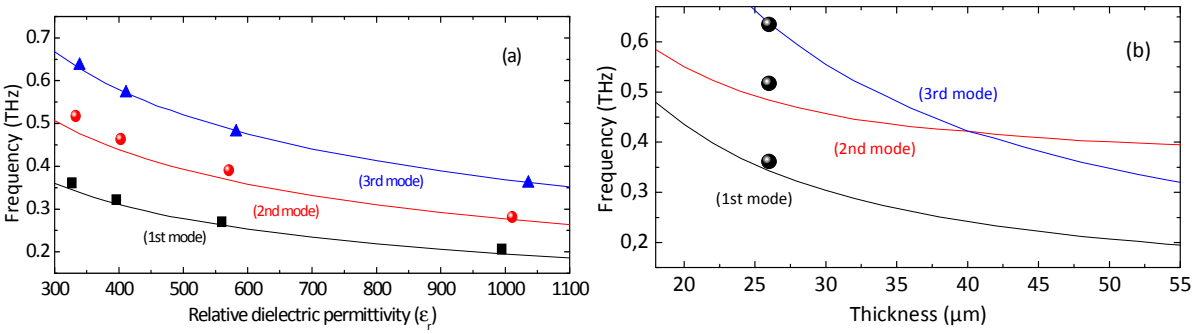

Figure 4.6: (a) resonant frequencies as a function of real part of relative dielectric permittivity Re(ε_r) of the $SrTiO_3$, (b) resonant frequencies as a function of the thickness (t) of the rods, calculations (lines), experiments (symbols).

In figures 4.6(a) and 4.6(b), we have depicted the evolution of the fundamental, the second and the third modes of Mie resonances, for different values of the thickness and the relative permittivity of $SrTiO_3$ rods. Beyond the good quantitative agreement between numerical and experimental results, our investigation reveals a hyperbolic decay of the resonant frequencies with an increase of thickness $\boldsymbol{t}$ and relative permittivity of the rods $\boldsymbol{\varepsilon_r}$.

4.3.2 Retrieval of Effective Parameters

Using the retrieval method, the calculated effective parameters ($\boldsymbol{\mu_{eff}}$, $\boldsymbol{\varepsilon_{eff}}$, $\boldsymbol{z_{eff}}$ and $\boldsymbol{n_{eff}}$) have been extracted from the complex transmittance and reflectance spectra and depicted in figure 4.7. It can be seen that the aforementioned Mie modes, are accompanied by a series of electric and magnetic resonances. Indeed, the first mode (TE_{11}) of Mie resonance at 0.263THz results in a resonant effective permeability, an anti-resonant behaviour of the permittivity associated with a negative imaginary part appears at the same frequency, which is inherent to periodic structures (metamaterial) as pointed out by (O'brien, 2002, Koschny, 2003), but their validity have not been discussed and their origin not demonstrated by the authors. This anomaly has been the subject of intense investigations by other authors, for a negative refractive index media consisting of split-ring resonators and metallic wires in the microwave regime (Seetharamdoo, 2005).

The second mode (TE_{12}) of Mie resonance located at about 0.383THz exhibits a resonant electric permittivity. As for the first mode (TE_{11}) of Mie resonance, the third (TE_{13}) and fourth (TE_{14}) modes result also in a resonant magnetic permeability around 0.547THz and 0.643THz, respectively. As noticed previously, an anti-resonant behavior related to these later modes is expected. The last fifth mode (TE_{15}) exhibits once again a resonant electric permittivity at about 0.691THz. The effective wave impedance is positive over the entire frequency band of study, thus demonstrating the passivity of the structure and the real part of the refractive index remains also positive.

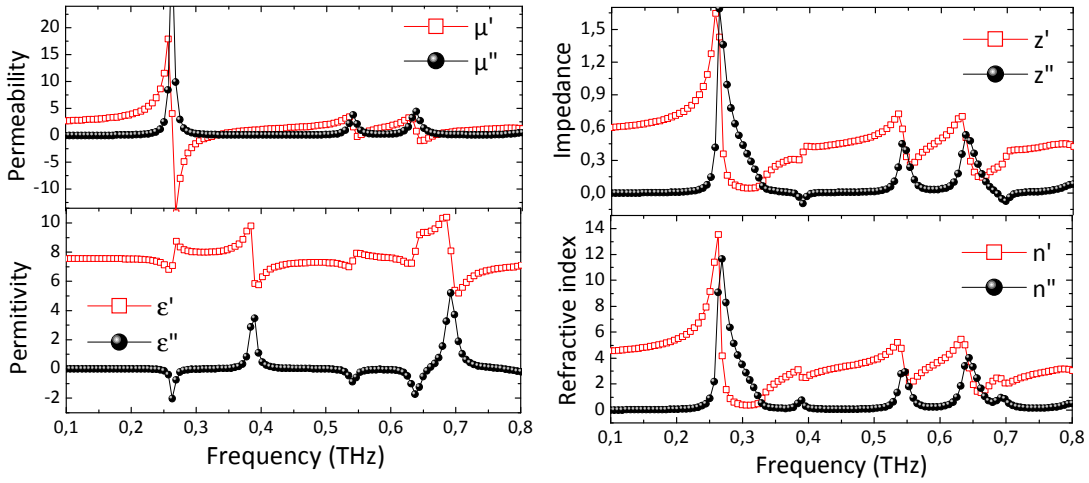

Figure 4.7: Extraction of the effective parameters, using the retrieval method (Smith, 2002), (a) permeability, (b) permittivity, (c) wave impedance, and (d) refractive index.

From the experimental point of view, while the complex transmittance spectrum can be easily measured in the THz range, the determination of the reflectance phase with a high precision, so as to allow a subsequent unambiguous determination of optical properties, is a challenging task requiring specific experimental approaches (Pashkin, 2003).

Moreover, during a THz-TDS measurement, it is very complicated to obtain simultaneously both transmittance and reflectance spectra with a ***single scan configuration measurement, at normal incidence*** by analogy to microwave measurements, using network vector analyzer and horn antennas (see chap. 2, sec. 2.3). We propose here an alternative method (***SSMM***: ***S****ingle* ***S****can* ***M****easurement* ***M****ethod*) to retrieve the complex effective parameters.

The main idea consists to put the investigated metamaterial into optical contact with a 2-mm thick high-resistivity silicon wafer ($\varepsilon_r \sim 11.7$, measured by THz-TDS) that was polished to achieve an excellent plane parallelism of input and output faces (<1μm), as illustrated in figures 4.8(a). The THz wave transmitted through this structure consists of a series of time-separated pulses $\boldsymbol{T_0}$ (direct transmission) and $\boldsymbol{T_1}$ (first echo) (see highlighted regions in figure 4.8(b)) originating from internal reflections within the sample (see figure 4.8(a)).

The time-windowing approach allows us to analyze their spectra one by one (Duvillaret, 1996) and to retrieve the complex permeability and permittivity (Smith, 2002, Němec, 2006) from complex transmittance and reflectance of the metamaterial encoded in these signals. Note that the sample must be sufficiently thick to enable this approach (Němec, 2006).

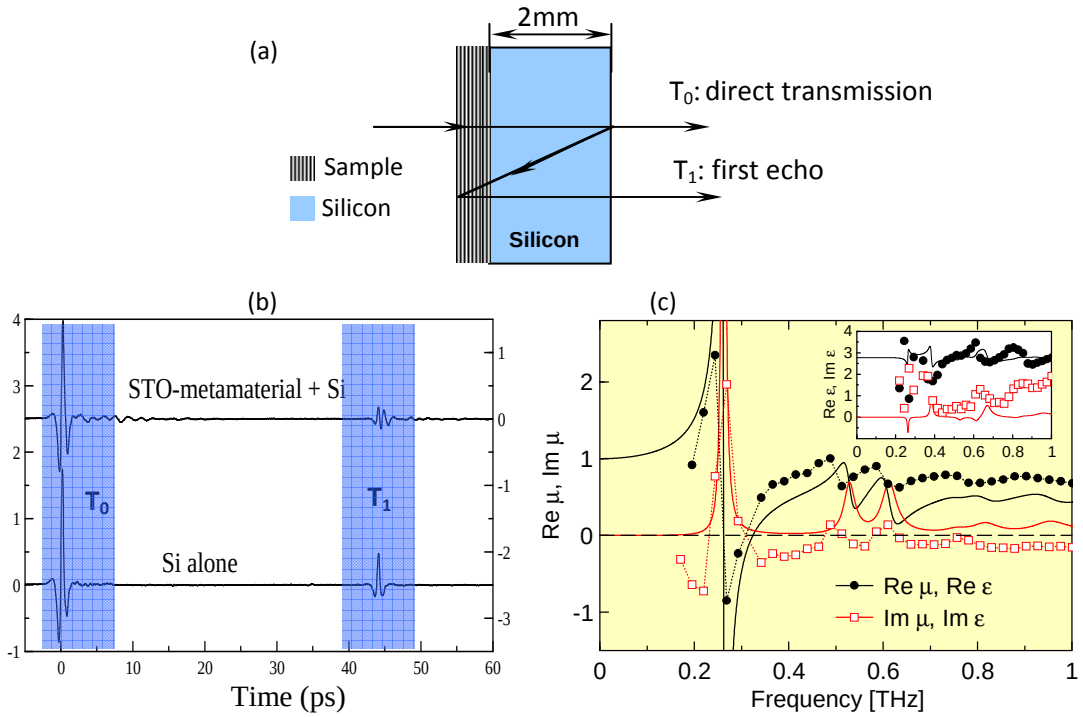

Figure 4.8: (a) Configuration of the Single Scan Measurement Method (SSMM) used to retrieve the effective parameters of our metamaterial, (b) spectra of time-separated pulses corresponding to internal reflections in the samples (metamaterial + silicon, silicon alone)m the y-axis is given in arbitrary units, (c) extraction of the theoretical and experimental effective permeability and permittivity related to the structure A: ***a***=33µm, ***P***=75µm, and ***b***=52µm at 324 K.

To provide a physical understanding of the phenomenon involved within the structure, we plot in figure 4.9 the spatial distribution of the electric and magnetic fields for different resonance frequencies in a single unit cell of our metamaterial (structure A: *d*=33µm, *P*=75µm, and *t*=52µm). The wave front of an incident plane electromagnetic wave undergoes a strong distortion close to the metamaterial in order to satisfy simultaneously the continuity and discontinuity conditions of tangential and normal electric-field components at the STO-air interfaces, respectively.

The electric field, which develops inside an STO rod, is then predominantly tangential close to the surface of the bar. This leads to the creation of displacive eddy currents within the bar cross section, which enhance the magnetic field in STO polarized along the bar, as shown in figure 4.9. A resonant behaviour is then expected at specific frequencies (Němec, 2009).The frequencies of the resonance modes depend on the geometrical dimensions and are given by

$$f_{mn} = \frac{c}{2\pi\sqrt{\varepsilon_r \mu_r}} \sqrt{\left(\frac{m\pi}{a}\right)^2 + \left(\frac{n\pi}{b}\right)^2}, \tag{4.2}$$

where *m* and *n* are integers, *a* and *b* are the dimensions of the cross section of the unit cell of the resonator, and c is the velocity of light (Guillon, 1977, Sethares, 1966). Since the magnetic field of the

incident wave is polarized along the axis of the resonators, the modes considered here are transverse electric (TE_{mn}).

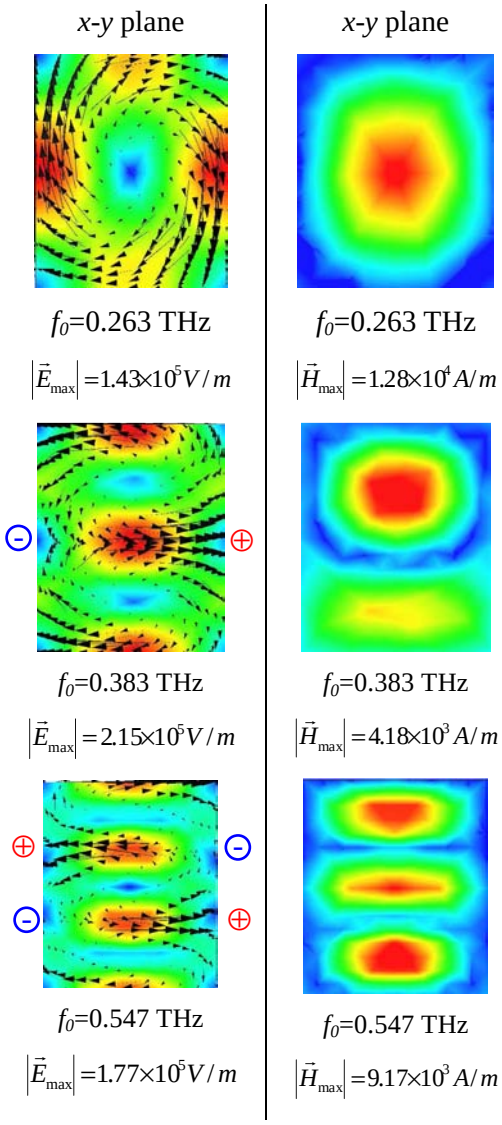

Figure 4.9: Electric (left panel) and magnetic (right panel) field distribution inside one unit cell of the rod for the lowest three order modes TE_{13}, TE_{13}, and TE_{13} at 0.263 THz, 0.383 THz and 0.547 THz, respectively in the *x-y* plane. The corresponding vector fields of the electric field E are also shown and the surface charge density areas are shown with related sign on electric vector fields (left panel).

The transmission spectrum is depicted above, in figure 4.10(a) and reveals five TE_{mn} modes of Mie resonances, respectively (TE_{11}, TE_{12} TE_{13} TE_{14} and TE_{15},) in the frequency band of interest from 1THz to 0.8THz. The effective permittivity and permeability have been extracted, using the standard retrieval method (Smith, 2002) and plotted in figures 4.10(b) and 4.10(c). From the extracted effective parameters, we can see that the first (TE_{11}), the third (TE_{13}), and the forth (TE_{14}) order modes, occurring at 0.263THz, 0.547THz and 0.643THz, respectively result in resonant effective permeability, and the $SrTiO_3$ rod is very similar to a magnetic dipole. Anti-resonance behaviors of the permittivity associated with a negative imaginary part are expected at the same aforementioned

frequencies, which is inherent in metamaterials (Koschny, 2003, Koschny, 2004). The second (TE_{12}) and the fifth (TE_{15}) modes occurring at 0.383THz and 0.691THz, respectively result in a resonant effective permittivity, and the $SrTiO_3$ rod behaves as an electric dipole.

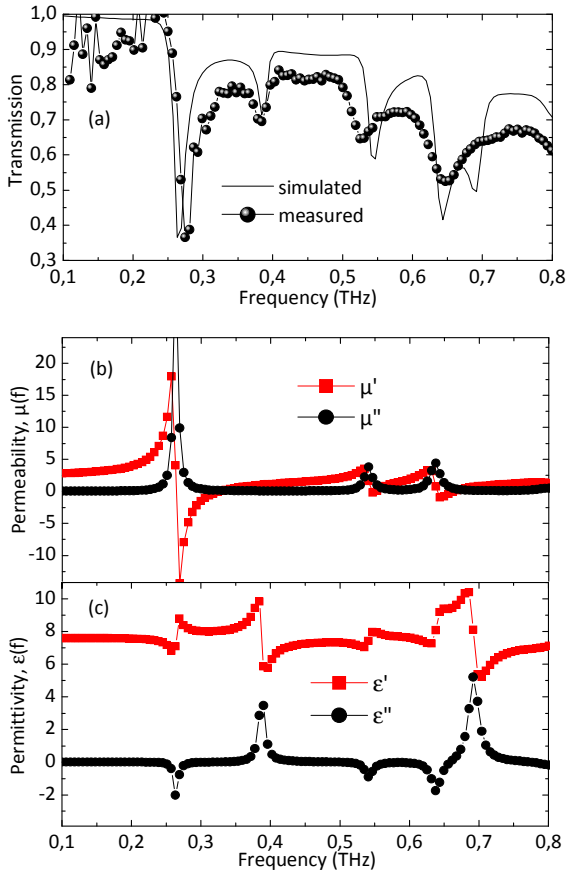

Figure 4.10: (a) Calculated and measured transmission coefficient, using the finite element method and THz-TDS, respectively, (a) calculated effective permeability, (a) calculated effective permittivity.

In the next section, I present an extended version of the STO-based metamaterial that exhibits a multiple (more than two) negative permeability frequency bands. Indeed our investigations clearly show that there exist three frequency bands where the effective permeability is negative. Furthermore a much broader continuous frequency range of negative effective permeability will be also demonstrated.

4.3.3 Multiple-Frequency Band Negative Effective Permeability

We have seen in the previous section that the properties of our metamaterials can be tuned by changing the temperature. This is higly desired, since it offers the possibility to operate at different frequencies. In this section, we will investigate a variant of our $SrTiO_3$-based metamaterial rods that exhibit a negative effective permeability over several frequency bands (more than two). Chen et al (Chen, 2004) proposed at microwave frequencies, an extended version of S-shaped metamaterial that exhibits two frequency bands where the effective refraction index ($\mathbf{n_{eff}}$) is negative (i.e. a double left-

handed pass-bands). More recently, Yuan et al (Yuan, 2008) reported in their work a design, fabrication and measurement of a dual-band electric resonances, planar metamaterials at terahertz regime, which results from the mutual coupling between the different resonances in the metamaterials. This multiple-frequency-bands metamaterials are very useful in various applications such as bandpass filters, wavelength division multiplexes, and antennas.

The unit cell of our investigated metamaterial consists of a set of $SrTiO_3$ rods separated by an air gap g=20µm, with three different widths denoted by a=50µm, b=30µm and c=20µm. The thickness of the rods is identical (t=50µm), as depicted in figure 4.11(a). The effective permeability is the superposition of individual responses of the three kinds of rods (see figure 4.11(b)).

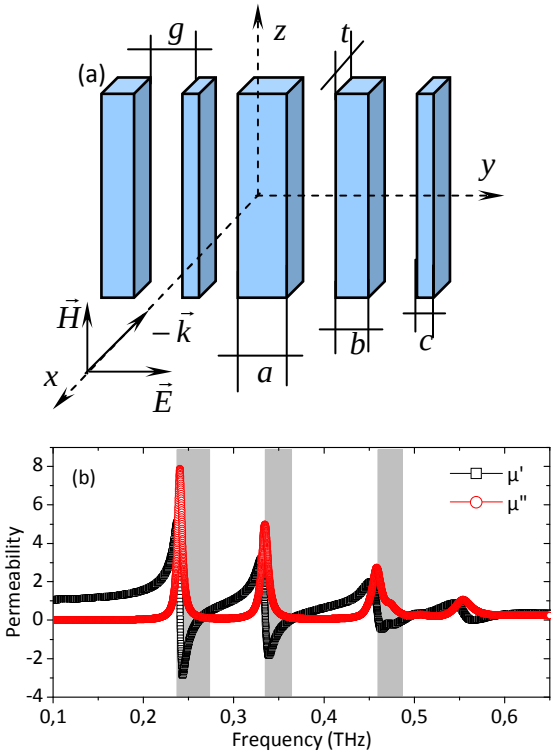

Figure 4.11: (a) Schematic view of our investigated multi-frequency-band metamaterial with the relevant geometrical dimensions: a=50µm, b=30µm, c=20µm, t=50µm, g=20µm, (b) real and imaginary parts of the calculated effective magnetic permeability.

The calculated patterns of the magnetic field inside the rods (see figure 4.12(c)) show that each rod is individually resonant and that the mutual cross couplings are negligible. We also varied the air-gap width g within 2–50 µm while the dimensions of the rods were fixed. This confirmed that ***g*** has a minor influence on the effective magnetic properties and leads only to a shift by a few gigahertz of the entire effective response. Virtually no electric and magnetic coupling between adjacent rods occurs, even if g is decreased down to 2 µm. Furthermore, the resonances are weaker than those observed in a metamaterial with a uniform width of rods, since the number of rods with each dimension is lower (see

figure 4.12(a) and (b)). Our proposed multiple-frequency band structure can be used as a spatial filer for THz antenna applications (Yahiaoui, 2009, Yahiaoui, 2011).

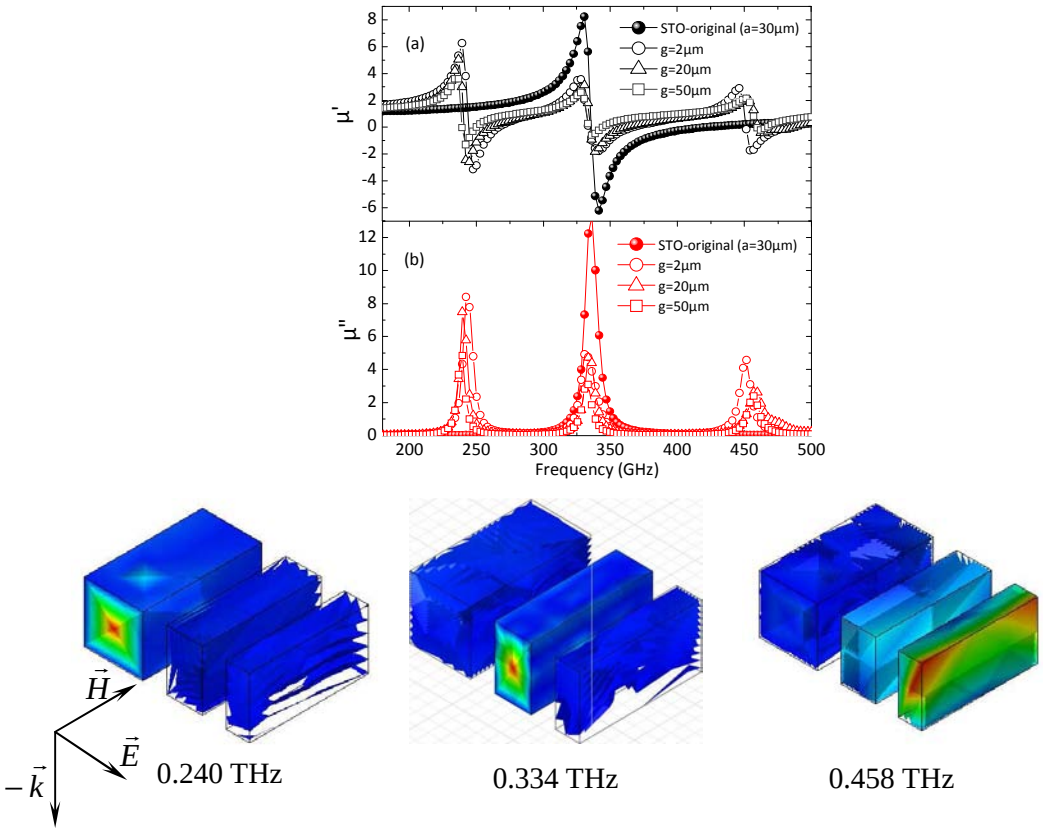

Figure 4.12: Real part (a) and imaginary part (b) of the calculated effective permeability μ_{eff} for a periodic structure of alternating rods with three different widths *a*, *b*, and *c*, filled circles, *a*=*b*= *c*=30 µm, *g*=20 µm, *t*=50 µm, hollow symbols, *a*=50 µm, *b*=30 µm and *c*=20 µm, *g* varies from 2 µm to 50 µm. (c) Sections of a unit cell of the MM with the spatial distribution of the resonant magnetic field. The ratios *H*max/*H*inc of the maximum and incident fields are 2.6 at 0.240 THz, 2.9 at 0.334 THz, and 2.4 at 0.458 THz.

4.3.4 Broad-Frequency Band Negative Effective Permeability

Due to the resonant behaviour of our investigated metamaterials, the frequency band of the negative effective permeability is intrinsically very narrow. In this section, we propose to extend this frequency band. Indeed, a much-broader continuous band of negative effective permeability (μ_{eff}) can be achieved in structures with a high aspect ratio (***a***>>***t***) (Yahiaoui, 2009, Yahiaoui, 2011). Here we consider structures each made of a single type of rods with width ***a*** varied over a broad range (50 to 200 µm) while ***g***=30 µm and ***t***=20 µm are kept fixed. The transmission coefficient and effective permeability spectra of such structures are shown in figures 4.13(a) and 4.13(b). The position of the first Mie resonance does not shift significantly as pointed out above, it is mainly imposed by the thickness ***t*** for *a*≥100 µm. By contrast, upon increasing *a*, the distance between the first- and higher-

order resonances decreases, and in the limit (a>>t) the resonances overlap (see figure 4.13(a)). This leads to a broadening of the region of negative (μ_{eff}) [see figure 4.13(b)]. For example, the retrieved effective μ for a=50 μm is negative within 480 GHz and 600 GHz, but for higher rod widths this range is much broader; namely for a=200 μm it spans over 250 GHz, corresponding to nearly 50% of the central frequency value. Figure 4.13(c) shows the effective μ for a=200 μm and values of tan (δ)=Im(ε_r)/Re(ε_r) from 0.1% to 5%.

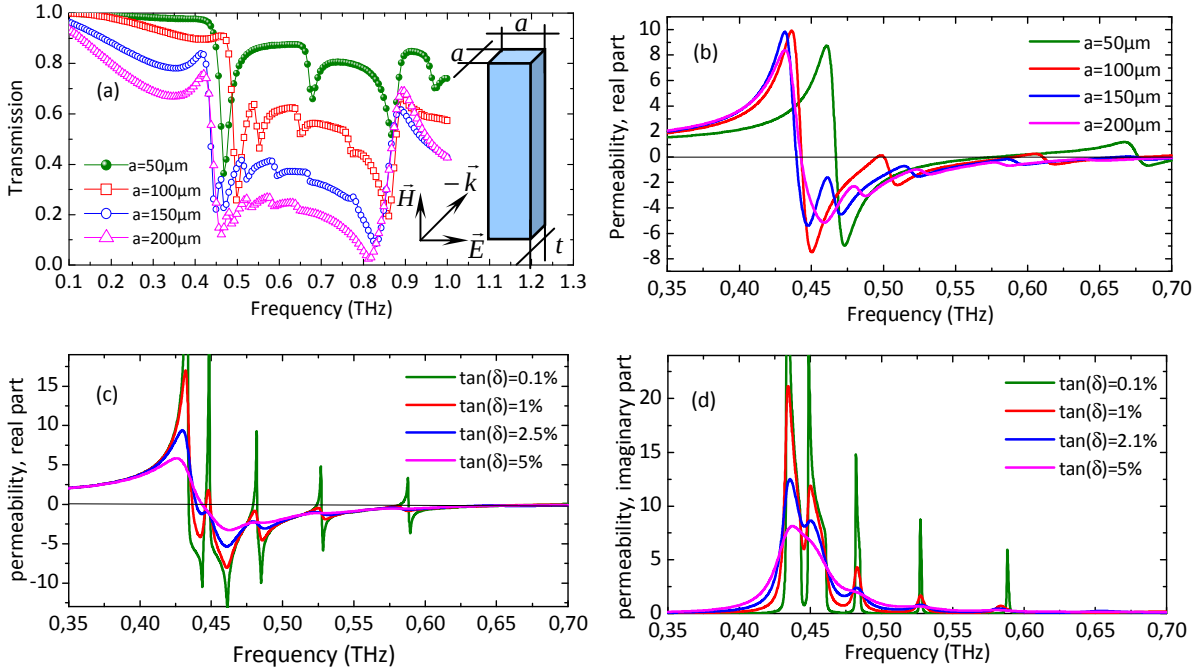

Figure 4.13: (a) Calculated amplitude transmittance for several widths a of STO rods (g=30 μm, t=20 μm, ε=300, tan δ =2.5%), the unit cell of our investigated metamaterial is represented as an insert, (b) the corresponding real part of the effective permeability. (c)-(d) real and imaginary parts of the effective permeability for a=200 μm, g=30 μm, t =20 μm and tan(δ) from 0.1% to 5%.

We observe clear magnetic resonances resulting in peaks in the effective response. Between the peaks, the effective μ is negative over a broad frequency range only if the dielectric losses reach a sufficiently high level (tan(δ)>1%). Upon the increase of tan(δ), the resonances become smoother and their magnitude decreases. The imaginary part of μ_{eff} shows a similar behaviour, the increase in tan(δ) leads to smaller effective magnetic losses at the resonances, while the mean level of losses increases proportionally to tan(δ) in the range of Re μ_{eff}<0 [see figure 4.13(d)].

Further analysis reveals a compromise between a high negative ε_r limited by the value of tan(δ) and a large bandwidth where μ<0. We propose an optimum thickness of t=20 μm for a=200 μm. Then the range of negative μ_{eff} spans from 430 to 680 GHz. Figure 4.14 shows the field distribution at resonant frequencies in this case.

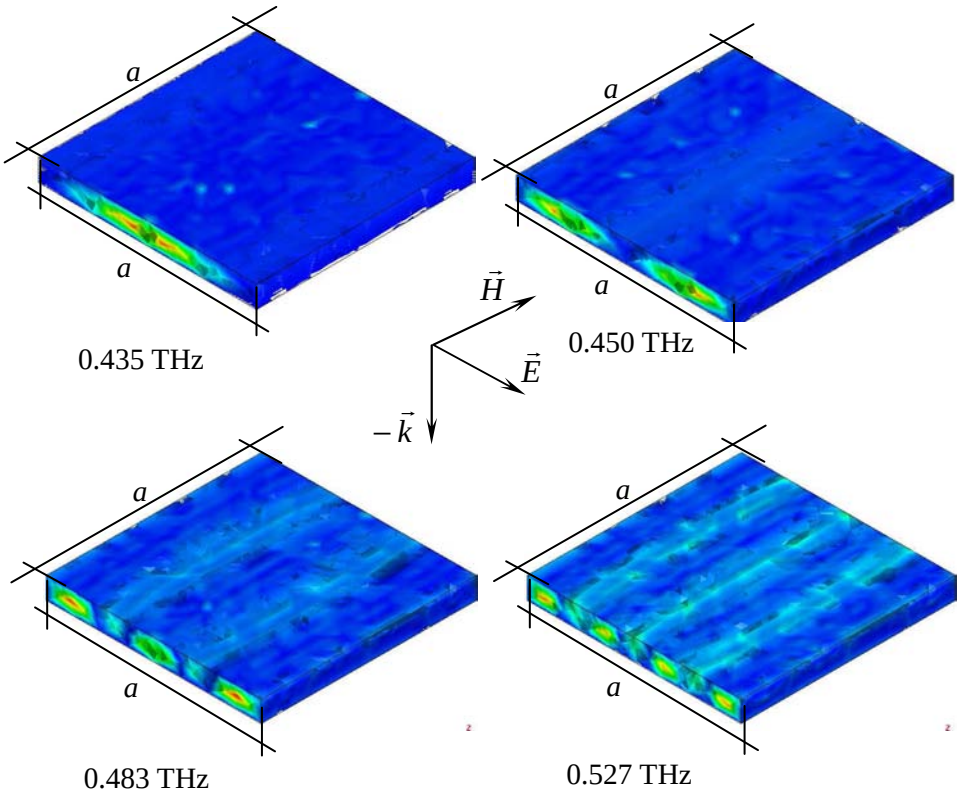

Figure 4.14: Spatial distribution of the resonant magnetic field inside the rods for a=200 µm, t=20 µm, and tan δ=2.5%, the ratios H_{max}/H_{inc} of the maximum and incident fields are 19.6 at 0.435 THz, 15.4 at 0.450 THz, 12.2 at 0.483 THz, and 8.7 at 0.527 THz.

In conclusion, we have proposed metamaterials exhibiting negative effective permeability in the THz range. We have demonstrated the tunability of the spectrale response by changing the temperature. We have also proposed variants of the original structure that exhibit an artifical magnetism over multiple frequency bands and over a broad-frequency range, as well. These structures can found various applications such as bandpass filters, wavelength division multiplexes, and antennas.

4.4 All Dielectric Metamaterials Based on Titanium Dioxide (TiO_2) Micro-Particles Layers

This work has been done in close collaboration with our colleagues from (CRPP: Centre de Recherche Paul Pascal) and (ICMCB: Institut de Chimie de la Matière Condensée de Bordeaux) laboratories, within the framework of the project: GIS-AMA-SAMM, which involves both theoricians and chemists. In order to synthesize isotropic - all dielectric metamaterials, we have simulated and experimentally tested some potential meterials such as: MgO, $LiTaO_3$ and TiO_2 single crystals. Indeed, the challenge was to find the material which exhibits simultaneously a large relative dielectric permittivity ε_r, and a low level of tangential losses tanδ, and the potential material that offered the best compromise was TiO_2. See appendix D, where the measured dielectric properties of a 1.55 mm thick

TiO_2 single crystal, is given. Calculations based on Maxwell Garnett theory (Lannebère, 2010), allowed providing our colleagues chemists with an abacus as a benchmark during the fabrication process in order to target easily the required parameters (size and volume fraction) for desired electromagnetic properties at the desired operating frequency (see appendix D for more details).

In this section, we have investigated a new approach in the fabrication of all dielectric metamaterials, the so-called "bottom-up" based on synthesis route and chemical assembly. A series of All Dielectric metamaterials based on TiO_2 micro-particles have been manufactured using this approach, which have been randomly deposited on thin films layers, transparent at terahertz frequencies.

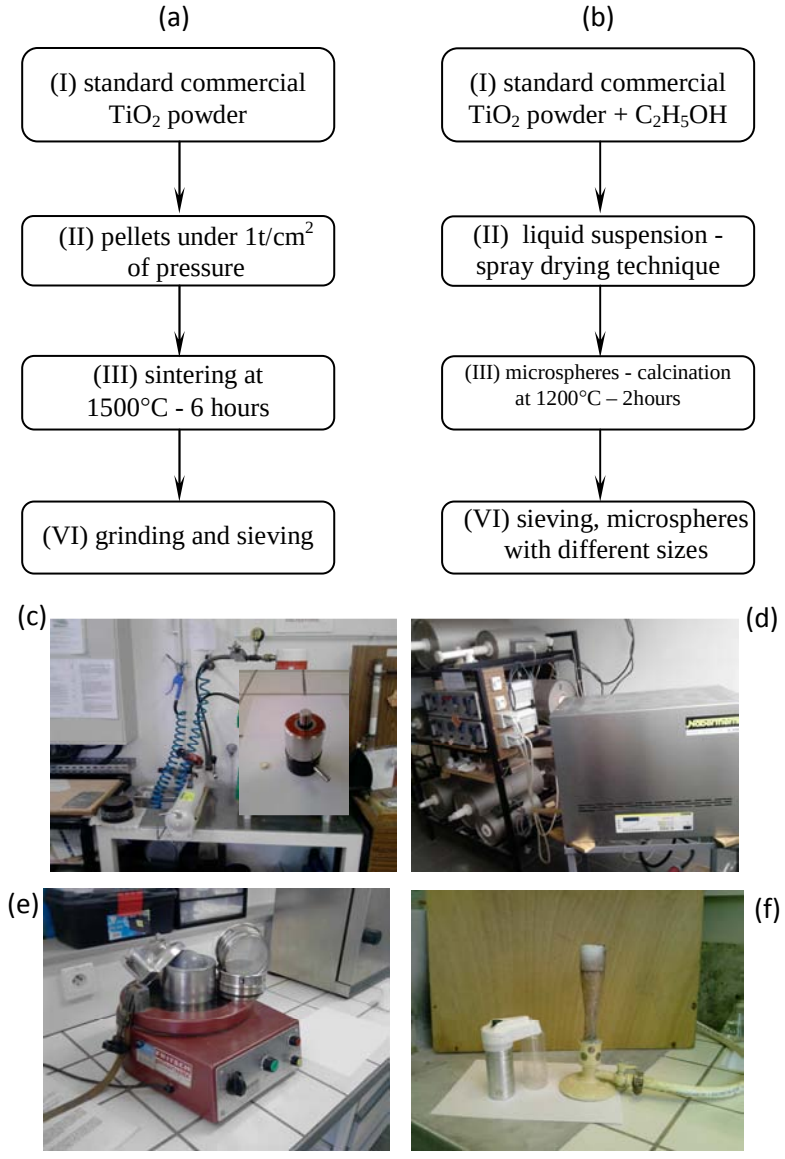

Figure 4.15: Fabrication sequences of our metameterials (a)-(b), real time images of ICMCB laboratory facilities used to fabricate our metamaterials, (c) presse, (d) sintering furnace (e) mill, (d) spray draying system.

The result of our investigations reveals a magnetic activity within our metamaterials, which exhibit a negative effective permeability. Starting with a standard commercial TiO_2 powder in rutile form, which is the most common and stable available form, two main techniques have been used to manufacture our metamaterials. Note that our experimental prototypes have been fabricated by Dr. U-Chan Chung from ICMCB laboratory.

The first technique, as illustrated in figure 4.15(a) consists to produce a series of pellets of about 13 mm diameter, under 1000 $kg.cm^{-2}$ of pressure. The pellets were heated at 1500 °C for 6 hours under oxygen-enriched atmosphere in order to obtain a much more cohesion and densification of pieces. The pellets have been crushed and sieved to obtain polydisperse (in shape and size) micro-particles. Subsequently, the fabricated microparticles have been randomly deposited onto a 100 µm thick film layer, completely transparent at terahertz frequencies ($\boldsymbol{n}$ ~ 1.05, and tan$\boldsymbol{\delta}$ ~ 0, measured by THz-TDS) in order to carry out measurements, using THz-TDS.

The second technique (see figure 4.15(b)) offers a possibility to fabricate particles with much accuracy on the shape of the particles. The TiO_2 powder is mixed with Ethanol (C_2H_5OH) to obtain a liquid suspension, which has been sprayed through flame, using spray drying technique. We obtain a spherical microparticles-based clusters, but still very fragile. Our microspheres are then sintered in a tube furnace at 1200 °C for 2 hours, in order to solidify and minimize the porosity of aggregates. Figures 4.15(c)-(f) show the ICMCB facilities used during the manufacturing process.

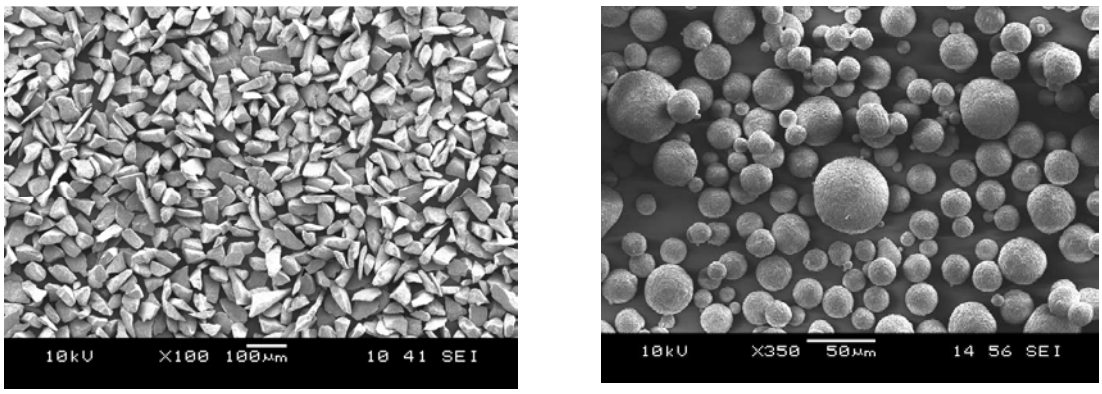

(a) (b)

Figure 4.16: Scanning Electron Microscope Images (SEM) of the fabricated micro-particles with a diameter comprises between 38µm and 40µm (a), and microspheres before sieving (b).

The microspheres are finally sieved and sorted into different diameters $\boldsymbol{d}$: <38µm, 38µm<$\boldsymbol{d}$<40µm, 40µm<$\boldsymbol{d}$<50µm, 50µm<$\boldsymbol{d}$<53µm, and 100µm<$\boldsymbol{d}$<106µm. This method was used as starting point for fabricating monodisperse micron-sized spheres and is still under intense investigations. Figures 4.16(a) and 4.16(b) show the Scanning Electron Microscope (SEM) images of the fabricated micro-particles and microspheres, respectively that have been obtained using the two aforementioned fabricating techniques.

4.5 Results of Experimental Characterizations

Using our **S**ingle **S**can **M**easurement **M**ethod (SSMM) and the classical retrieval method (Ghodgaonkar, 1990), we have extracted the effective parameters of our metematerials, as depicted in figure 4.17. The retrieved effective permeabilities are strongly dispersive and exhibit a Lorentz-like resonant behavior with Re(μ)<0 over a broad frequency band from 0.39 THz to 0.6 76 THz, as shown in figure 4.17(b) for microparticles with sizes between 40µm-50µm. Typically, since we deal with *LC* and / or Mie resonances in the most common case, the negative effective permeability region is intrinsically very narrow. This behaviour (broad frequency range of negative µ) is probably due to the polydisperse character in size and shape of our investigated samples, which gives rise to coupling effects between many spectrally-adjacent resonances, the broad frequency range of negative µ is then expected (Yahiaoui, 2011).

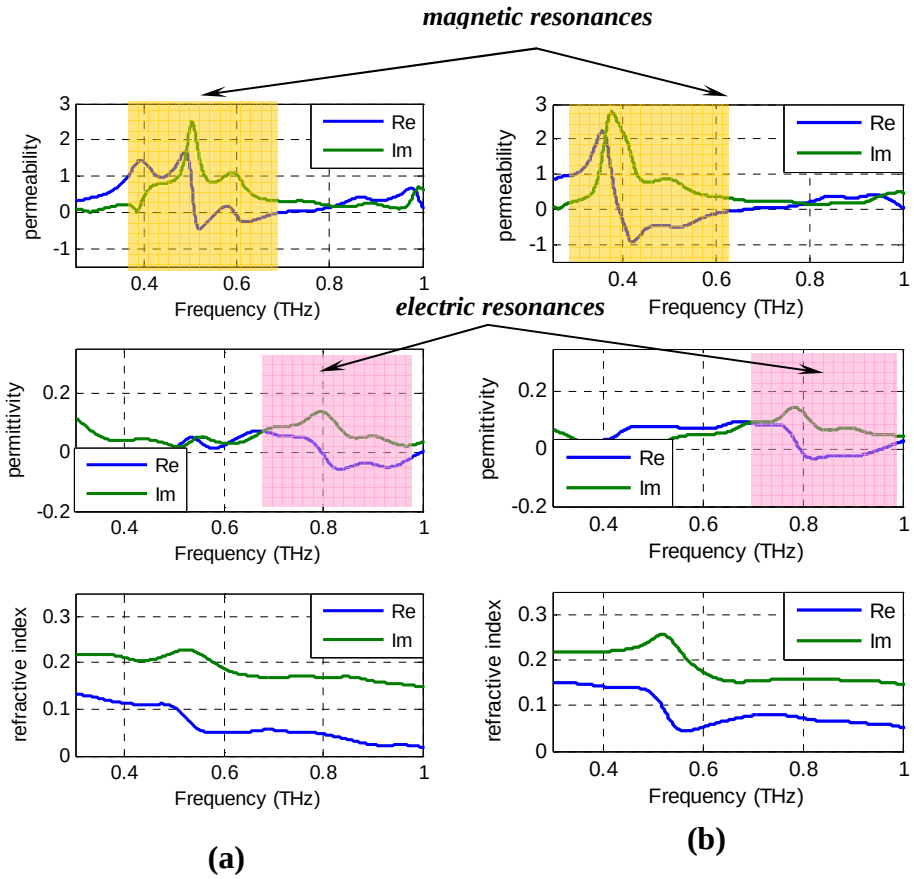

Figure 4.17: Experimental extraction of effective parameters of our investigated metamaterials, for 38µm<size-particles<40µm (a), and 40µm<size-particles<50µm (b), respectively.

Indeed, as observed by (Lannebère, 2010, Lannebère, 2011) in the case of polydispere-size spherical particles, calculations based on Clausius-Mossotti formula show a broadening of the negative effective permeability region accompanied by a reduction in depth, as the standard deviation

to average size (Gaussian distribution) does not exceed 10%. Note that, a resonant behavior is also observed in the electric response for the two ranges of particle-sizes, thus leading to negative effective permeability also over a wide frequency range. Indeed, the negative ε_{eff} region extends from 0.8 THz to 1 THz approximately in the case of particle-sizes between 38µm and 40µm and from 0.8 THz to 0.96 THz approximately for: 40µm - 50µm particle-sizes range.

One can see that the magnetic resonance is more pronounced then the electric resonance. Unfortunately, the negative regions of ε_{eff} and μ_{eff} do not overlap in frequency, and then the refractive index does not reach negative values. Indeed, as pointed out by Vendik et al (Vendik, 2006, Vendik, 2008, Vendik, 2009), a double negative (DNG) media can be realized in the frequency region where electric resonance of one kind of particles and magnetic resonance of another kind of particles are presented simultaneously. It also needs the conditions of concentration (filling factor) and particle size ration between the two kinds of particles.

In our case, the first technique of fabrication described above does not offer the possibility to control all the critical parameters (particle sizes, shapes, filling factor and size ration) that may lead to a negative refractive index. Indeed, as mentioned previously, our first fabricated microparticles (that have been spread randomly on a 100µm thick transparent layer) exhibit a large polydispe distribution in shape and size. But despite these aforementioned drawbacks and despite the rudimentary aspect of our fabricated samples issued from the first technique of fabrication, the results of our experimental characterizations are rather good, which demonstrate that metamaterials do not require sophisticated fabrication techniques.

The results of experimental characterizations related to microspheres (figure 4.16(b)) are not presented here, since these latter are still under intense investigations with the aim to solidify and minimize the porosity of micro-particles-based aggregates, thus may leading to better results of magnetic response. We will now move to the second part of this chapter, which is dedicated to the study of composite (metal-dielectric) metamaterials.

4.6 Composite Metal-Dielectric Metamaterials

In this section, we investigate a series of composite metal-dielectric metamaterials, which have been designed, fabricated and characterized in the terahertz regime. Indeed, we report on the investigation of the Extraordinary Optical Transmission (EOT) effect induced in sub-wavelength holes-array metamaterial. Subsequently, we will discuss about a single- and double-layered fishnet metamaterials fabricated using thin flexible polymer films as substrates and standard optical lithography technique in the fabricating process. Simulations of electromagnetic wave propagation were performed using finite element method software simulator. The experimental work was carried

out by means of time domain terahertz spectroscopy and we employed the Single Scan Measurement Method (SSMM) approach.

4.6.1 Subwavelength Apertures-Array Metamaterial

Nowadays, periodic sub-wavelength apertures constitute an intense and wide research field within nanophotonics. EOT and negative refraction are the two main remarkable phenomena which results from these structures. It is well kown that the negative refraction effect arises from the structurating and shape of metamaterials rather than the intrinsic composition. It has to be stressed on that it is the periodicity of the structure (holes-array) which enables coupling between the incident light and Surface Plasmon Polaritons (SPPs) (i.e. coupling from external light to guided modes). As a result a multiple EOT peak appear in the spectral response, and an enhancement of the transmission higher than that predicted for a single hole in a perfect conductor is expected (Genet, 2007, Ortuño, 2010). Since the pioneering theoretical description of SPPs of R. H. Ritchie in 1957 (Ritchie, 1957), E. Economou in 1969 (Economou, 1969), followed by the works of Ebbesen *et al* in 1998 (Ebessen, 1998), SPPs attracted the attention of fundamental research giving rise to the field of plasmonics

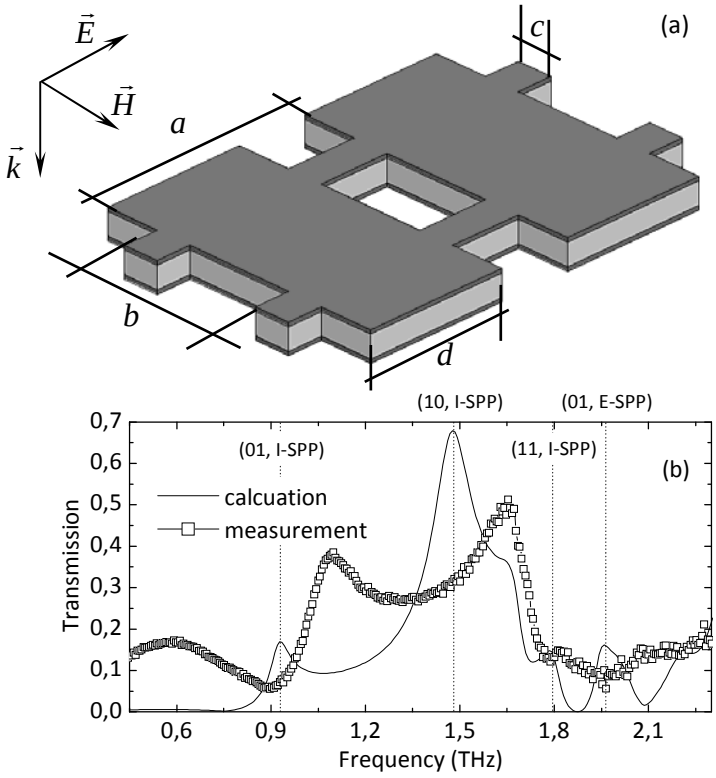

Figure 4.18: (a) Schematic of the subwavelength holes-array metamaterial fabricated by micromachining laser and characterized by terahertz time domain spectroscopy (THz-TDS). The geometrical dimensions are: a=160 µm, b=110 µm, c=36 µm, d=120 µm, t=15 nm, t=50 µm. (b) Calculated (solid lines) and measured (lines+symbols) transmission amplitude spectra of the studied sample for TM polarization.

In this present section, we investigate a subwavelength holes-array metematerial that has been designed, fabricated and characterized at terahertz frequency range. The technique used here for the fabrication employs a direct hole etching process (femtosecond laser micromachining) through the metal-polymer-metal structure. The dielectric used in the fabrication is rather thicker (50µm). The substrate is covered by 40 nm gold layers on both sides and is subsequently exposed to a Yb:KGW 1.03 µm femtosecond laser. The ultrafast regime offers an enhanced control in sculpting the desired microstructures as the laser energy deposition occurs on a timescale much shorter than heat transport (electron-phonon coupling). The schematic view of our proposed metamaterial is shown in figure 4.18(a) and the polarization that has been considered here is illustrated in the same figure. The relevant geometrical dimensions are: $\boldsymbol{a}$ = 160 µm, $\boldsymbol{b}$ = 110 µm, $\boldsymbol{c}$ = 36 µm, $\boldsymbol{d}$ = 120 µm, $\boldsymbol{t}$ = 50 µm (the dimensions of the apertures are : 74 µm × 40 µm i.e. ~ $\lambda/5 \times \lambda/10$, respectively).

The transmission spectra of the fishnet structure is depicted in figure 4.18(b) and clearly shows a fairly good agreement between simulation and measurement. We notice a minor shift towards high frequencies for the measured spectrum, which is probably relative to dimension discrepancies induced by laser micromachining technology. The negative refractive index should be near the first peak, the second peak that occurs at about 1.5 THz in simulation and around 1.65 THz in experiment, reaches a maximum value of about 0.7 in theory and 0.5 in experiment and plays no role in achieving the negative refractive index. It is also possible to predict the frequencies for which surface plasmons polaritons appear and also the nature of each plasmon, using mathemathical formalism, as described below.

Indeed, it is well known that Surface Plasmon Polaritons (SPPs) are oscillations of surface charges at the metal interface and are excited when their momentum matches the momentum of the incident photons according to the following momentum conservation relation (Degiron, 2005, García-Meca, 2009, Ortuño, 2009, Li, 2010):

$$\left|\vec{k}_{SPP}\right| = \left|k_x \pm n\vec{G}_x \pm m\vec{G}_y\right|, \tag{4.3}$$

$$\left|\vec{k}_{SPP}\right| = \left|k_0 \sin\theta \pm n\vec{G}_x \pm m\vec{G}_y\right|, \tag{4.4}$$

where $\vec{k}_{SPP}$ is the surface Plasmon wave vector, $k_x = k_0 \sin\theta$ is the in-plane component of the incident photon's wave vector, $\left|\vec{G}_x\right| = 2\pi/a$ and $\left|\vec{G}_y\right| = 2\pi/b$ are the reciprocal lattices wave vectors for the given array, $\boldsymbol{a}$ and $\boldsymbol{b}$ being the lattice periodicity and n, m are both integers. If the angle of incidence θ varies the incident radiation excites different SPPs modes. The surface modes on the input side couple evanescently to the exit side before being re-emitted into freely propagating light. The role of the surface modes is to enhance the field amplitude above the apertures which then compensates for the exponential attenuation of the evanescent field in the depth of the non propagating aperture. As a

consequence, the transmission spectrum is characterized by a series of peaks corresponding to the appearance of modes together with their interference and scattering in and out of the plane. The transmission peaks are due to the excitation of different SPP modes and their positions are given by the following approximating equation (Degiron, 2005, Ortuño, 2009, Li, 2010):

$$\lambda_{peak} = \mathrm{Re}\left[\sqrt{\frac{\varepsilon_m(\omega)\varepsilon_d}{\varepsilon_m(\omega)+\varepsilon_d}}\right]\times\frac{ab}{\sqrt{\left(i^2b^2+j^2a^2\right)}}, \tag{4.5}$$

where $\varepsilon_m(\omega)$ and ε_d are the dielectric constant for the metal (Au) and the substrate material (air or polymer), *a* and *b* are the lattice constants, *i* and *j* are the scattering orders from the array. Each peak can then be labelled by a set of integers (*i*, *j*), as shown in figure 4.18(b). I-SPP and E-SSP denote the internal (dielectric / metal) and external (air / metal) Surface Plasmon Polaritons, respectively.

Using an adapted and optimized version of our proposed retrieval method (***SSMM***: ***S****ingle* ***S****can* ***M****easurement* ***M****ethod*), first demonstrated in (Němec, 2009), the transmission and reflexion coefficients can be obtained simultaneously in terms of magnitudes and phases, and then the effective parameters can be retrieved (Ghodgaonkar, 1990). See appendix ***C*** for more details about the description of the adapted and the optimized version of our proposed SSMM.

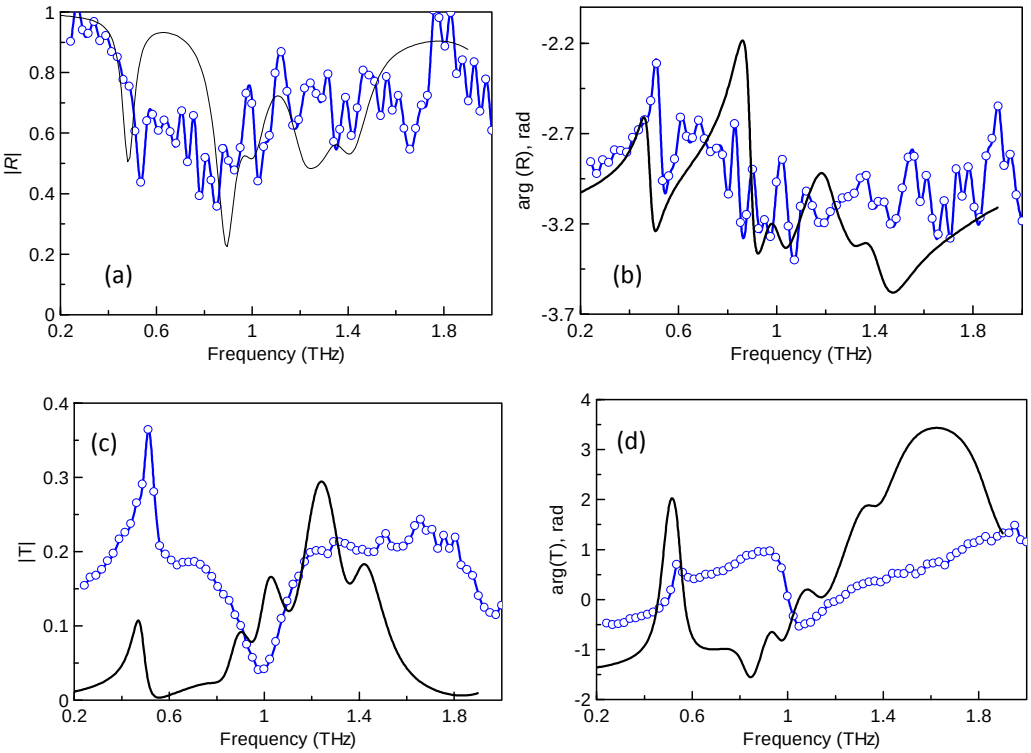

Figure 4.19: Simulated (solid lines) and measured (lines and symbols) magnitude of the reflection (a), phase of the reflection (b), magnitude of the transmission (c), phase of the transmission (d).

Indeed, our investigated metamaterial is enclosed between two thick sapphire crystals. In this configuration, possible unwanted air gaps between the metamaterial and the wafers can be

substantially reduced. Moreover, by this arrangement the metamaterial is entirely embedded in a medium with a homogeneous refractive index and not positioned at an interface between two different media, as reported previously in section 4.3.2 (Němec, 2009).

Figures 4.19(a)-(d) shows the calculated (solid lines) and measured (symbols and lines) magnitudes and phases of transmission and reflection coefficients of our investigated metamaterial. The reflexion coefficient shows a very good quantitative agreement (in both magnitude and phase) between simulations and measurements as illustrated in figures 4.19(a) and 4.19(b), while the simulated transmission coefficient exhibits a disagreement in both magnitude and phase compared to the measured one (see figures 4.19(c) and 4.19(d)).

A first intuitive cause that can explain the origin of this disagreement is the imprecisions and imperfections that can occur during the fabricating steps. Indeed, viewed under an electronic microscope, our investigated structure revealed impurities such as: cutting metallic-patterns and non-metalized areas, as well. The active zone corresponding to the real number of "undamaged-cells" that have been illuminated during the measurements is then reduced. This can modify critically the spectral response and the electromagnetic properties of the structure, as we have already pointed out in chap. 3, sec. 3.2.1.

The dielectric used in the fabrication was characterized by terahertz time domain spectroscopy. The electrical response of the substrate exhibits a dispersive behaviour within the frequency band of interest, with tangential losses that vary between 6% and 15% approximately (see figures 4.20(a) and 4.20(b)). This behaviour can be also, in part at the origin of this unexpected disagreement between the simulated and the measured transmittance function.

Furthermore, a series of numerical simulations have been performed, taking into account different parameters that can be very critical in the determination of the spectral response of the structure. Indeed, different thicknesses of the metallic patterns, the air gap that may exist between the sample and the host medium (since the investigated sample is enclosed between two thick sapphire crystals), and different conductivities σ of the metal have been taken into account in order to attempt elucidating the origin of this anomaly. Our study reveals the following:

The thickness of the metal layers is a very critical parameter in the determination of the spectral response of a composite metal-dielectric structure, since it is related to the skin depth effect, which is given by the following expression:

$$\delta = \sqrt{\frac{2}{2\pi f_0 \cdot \mu_0 \cdot \sigma}}, \tag{4.7}$$

where f_0 is the working frequency, $\mu_0 = 4\pi\ 10^{-7}$ [T.m/A] is the magnetic constant and σ=4.5 10^7 S/m is the hypothetical conductivity of the gold layer. One can see that the skin depth strongly depends on the conductivity σ of the metal layer, which is a very critical parameter for ultra thin layers. The

calculated skin depths at 0.5 THz, 1THz, 1.5 THz and 2THz from equation (4.7) are: 106nm, 75nm, 61.3nm, and 53nm, respectively which are much larger then the thickness 40nm of the coated gold layers. Indeed, the skin depth is supposed to confine the electromagnetic wave and prevents its transmission through the metallic parts of the structure.

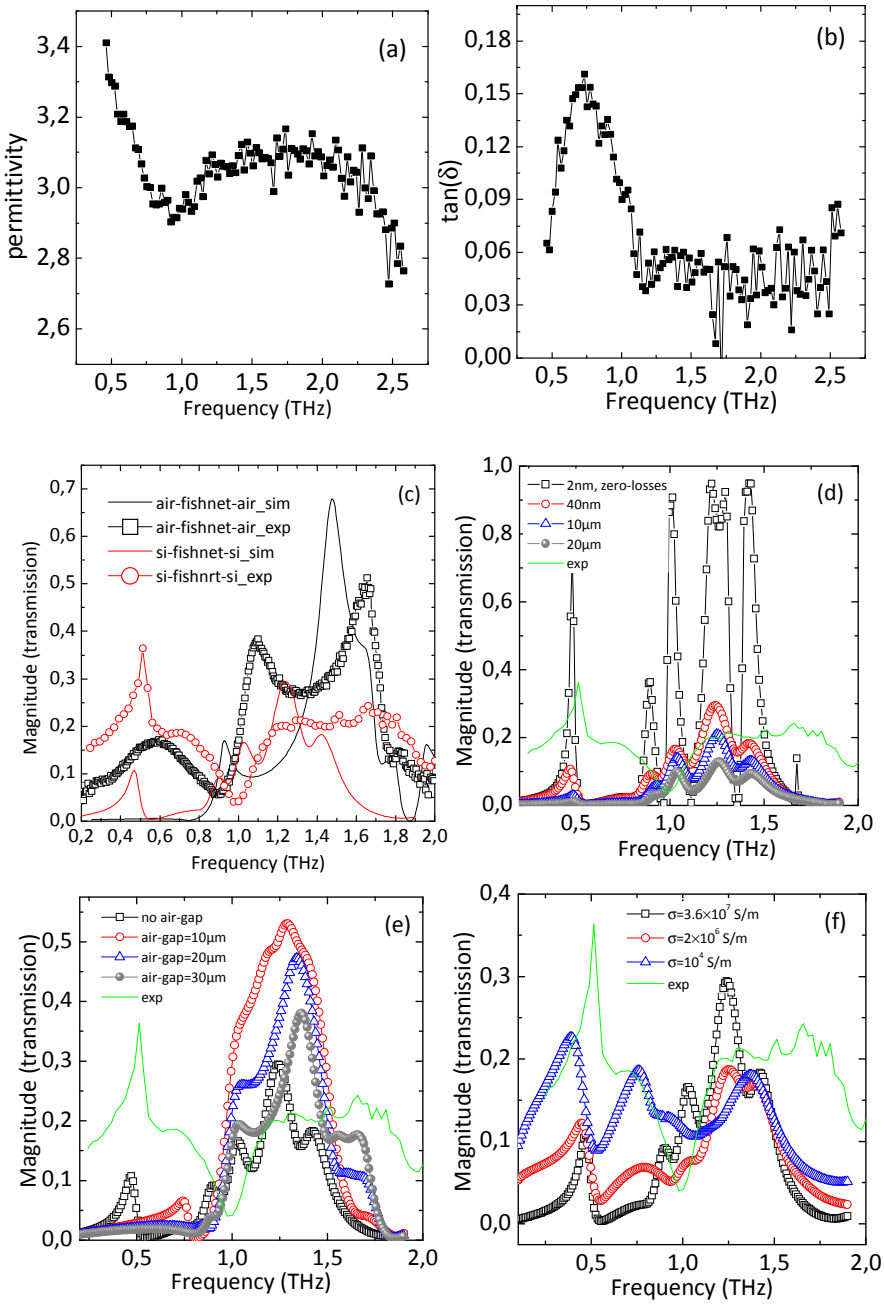

Figure 4.20: Experimental extraction of the relative dielectric function (a) and tangential losses (b) of the dielectric substrate measured by THz-TDS. (c) Measured and simulated transmission coefficient for two possible configurations of the sample in free space and enclosed between two thick sapphire crystals. Parametrical study performed for different thicknesses of the metallic patterns (d), for different values of the hypothetical air gap that may exists between the investigated sample and the silicon waffers (e), and for different values of the conductivity σ of the metal (f).

Nevertheless, we have observed that the calculated skin depths given above for some frequencies within the frequency band of working are much larger than the thickness of the gold layer ~ 40 nm. This can explain partially the disagreement in the transmission spectrum. But it seems that the skin depth effect is not taken into account by our software simulator HFSS, since the attempt to reproduce the measured transmission by simulation fails, even for 2nm thick gold layers with zero-losses dielectric substrate (see figure 4.20(d)). When the structure is sandwiched between two sapphire crystals, an additional sharp peak appears at about 0.5 THz simultaneously in both experiment and simulation and reaches a naximum value of about 0.1 in simulation and approximately 0.4 in measurement (see figure 4.20(c)). This peak corresponds to the external E-SPP (01) mode at the Al_2O_3/Au interface predicted around 0.55 THz by the calculation from equation (4.5) given above. The relative dielectric permittivity of the ε_r of the sapphire is assumed to be equal to 11.68. This mode is added to the unexpected high level of transmission related to the skin depth effect, as explained previously, thus giving rise to the large amplitude of the measured transmission compared to the simulated one.

The presence of an air gap between the host medium (sapphire) and the sample tends to suppress the Al_2O_3/Au (01) mode (see figure 4.20(e)) and a low value of the conductivity leads to a significant enhancement of the simulated transmission level on both sides of the Al_2O_3/Au (01) mode (see figure 4.20(f) for the case of $\sigma=10^4$ S/m). This confirms that the real value of the conductivity σ of the gold layer is less then what has been taken into account during simulations (i.e. $\sigma=4.5\ 10^7$ S/m). Indeed, the grain sizes and percolation effect can alter dramatically the real conductivity behaviour of thin metal layers.

The effective parameters of our metamaterial have been retrieved and depicted in figure 4.21 using the standard method of extraction (Ghodgaonkar, 1990). One can see that both the effective magnetic permeability and the effective electric permittivity exhibit a resonance at the frequency of the guided mode 0.5 THz. However the effective permeability does not reach negative values. At the first internal surface plasmon polariton denoted by (01, I-SPP), which is localized at about 0.9 THz in simulation and around 1THz in experiment, the effective permeability adopts a Lorentz-like behaviour and reaches negative values around the aforementioned resonant frequency of 0.9 THz. The effective permittivity exhibits a Drude-like model with negative values below the plasma frequency at about 1.2 THz in simulation. The effective refractive index is negative over a frequency band which extends from 0.7 THz to 1.1 THz in simulation, approximately and from 1THz to 1.2 THz in measurement and reaches a maximum value of about -0.7 (see highlighted regions in figure 4.21). Note that the experimental negative refractive index is mainly due to absorption effects, since the condition $\varepsilon_1\mu_2 + \varepsilon_2\mu_1 < 0$ is satisfied (Depine, 2004). The effective impedance is positive, confirming the passivity of the medium with very small imaginary part.

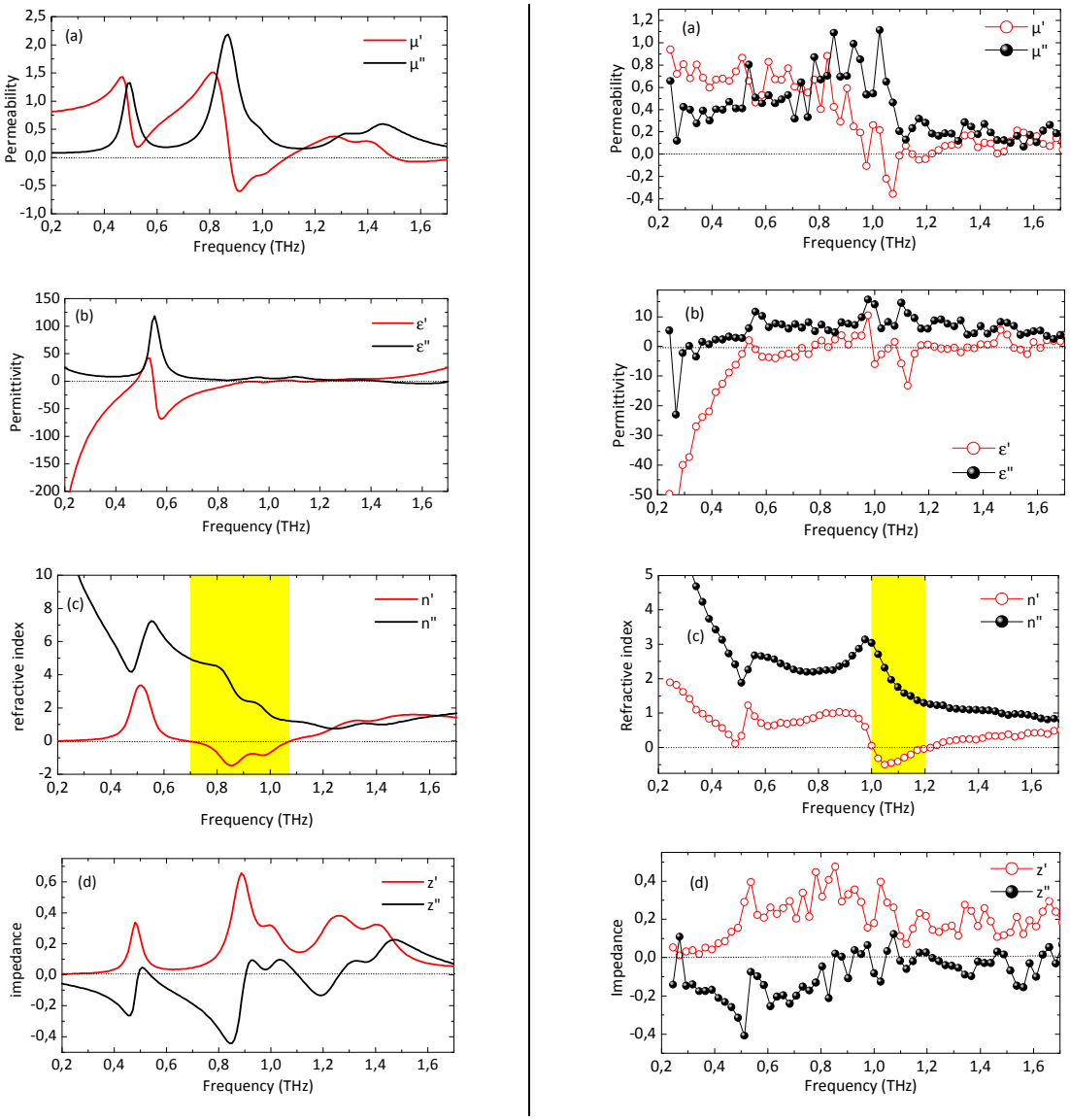

Figure 4.21: Extraction of the effective parameters from simulated (left panel - solid lines) and measured (right panel - symbols) transmission and reflexion coefficients: permeability (a), permittivity (b), wave impedance (d), and refractive index (e).

Finally, we are persuaded that a non-dispersive dielectric substrate with a low-loss level coated by sufficiently thick metallic layers with a well-known and as large as possible conductivity σ, could give better results of characterizations. The next sections are dedicated to the study of a single and a double metal layer fishnet metamaterials that have been fabricated using standard optical lithography.

4.6.2 Single Layer Metamaterial

The schematic view of our investigated single metallic layer structure is proposed for an operating frequency of about 1 THz and shown in figure 4.22(a). The layout consists of a single perforated metal layer in form of a fishnet on top of a (non-perforated) 50 μm thick commercially available polyester film (DuraLar®). This film has a good mechanical flexibility and was chosen as the dielectric substrate

due to its moderate dielectric constant $\varepsilon_r = 4$ and low losses $\tan\delta = 0.09$ in the terahertz range (both measured by THz-TDS). We purchased the film already coated with a 40 nm, thick aluminium layer on one side, which was subsequently perforated using a classical I-line contact photolithography technique and a final wet etching of the aluminum in 10% phosphoric acid. The structure is anisotropic and both polarizations were investigated: TM mode ($\boldsymbol{E} \parallel \boldsymbol{z}$ axis, $\boldsymbol{H} \parallel y$) and TE mode ($\boldsymbol{E} \parallel y$, $\boldsymbol{H} \parallel \boldsymbol{z}$), the propagation direction being along the $\boldsymbol{x}$ axis ($\boldsymbol{k} \parallel \boldsymbol{x}$) in both cases. The relevant geometrical parameters are defined in figure 4.22(a). In figure 4.22(b) a comparison of the measured and simulated transmission coefficient of the single layer metamaterial is presented for both polarizations (TM and TE).

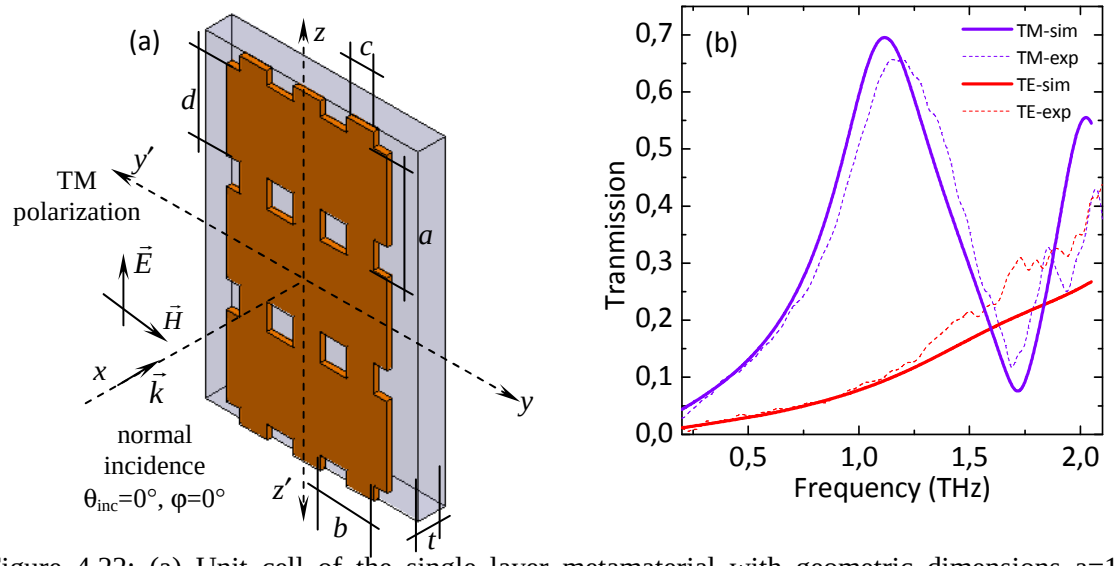

Figure 4.22: (a) Unit cell of the single layer metamaterial with geometric dimensions a=123µm, b=91µm, c=20µm, d=90µm, t=21µm. (b) Measured (dashed lines) and calculated (solid lines) transmission amplitude spectra of the studied sample for TE and TM polarizations.

Concerning the TM polarization, we observe a bandpass response centred near 1 THz with a FWHM (Full Width at Half Maximum) bandwidth in the power spectrum of about 0.7 THz. The peak transmission reaches ~ 0.65 which is higher than the relative area of the holes. This extraordinary transmission was explained in terms of surface plasmon tunnelling (Ebbesen, 1998, Moreno, 2001). The TE mode shows a low level of transmission and a featureless response in our spectral range. The quantitative agreement between theoretical and experimental results is very good, except for a minor shift towards higher frequencies of the experimental curve in the case of TM polarization.

This structure does not exhibit a negative refractive index but can be used as a spatial filter in front of a terahertz antenna and as a benchmark sample for data analysis and comparison with double fishnet structures. Moreover, the enhanced field associated with SPs makes them suitable for use as sensors (Hornola, 1999, Kneipp, 2002), and commercial systems have already been developed for sensing biomolecules.

4.6.3 Double Layer Fishnet Metamaterial

A double fishnet structure consists of two identically patterned metal layers, one on each side of the thin dielectric substrate. We employed a self-aligned technique to ensure that the two opposite patterns are aligned. Starting with the fabricated single layer fishnet structure, we use here a second lithography step to define the fishnet pattern on the opposite side of the film. To do this, the opposite face of the film is coated with a negative photoresist and the sample is illuminated through the already existing aluminum fishnet layer on the top. Consequently the existing metal fishnet serves as a mask for the negative resist on the bottom side of the polymer film which the alignment of the top and bottom patterns (self-aligned technique). Subsequently, the exposed negative resist is developed and a 15 nm thick gold layer is deposited. Finally, a soft ultrasonic assisted lift-off process is performed so that the desired gold fishnet structure remains at a mirror symmetric position to the aluminum fishnet at the top. The prepared double-layered metamaterial covered an area of 2.5 × 3 cm^2.

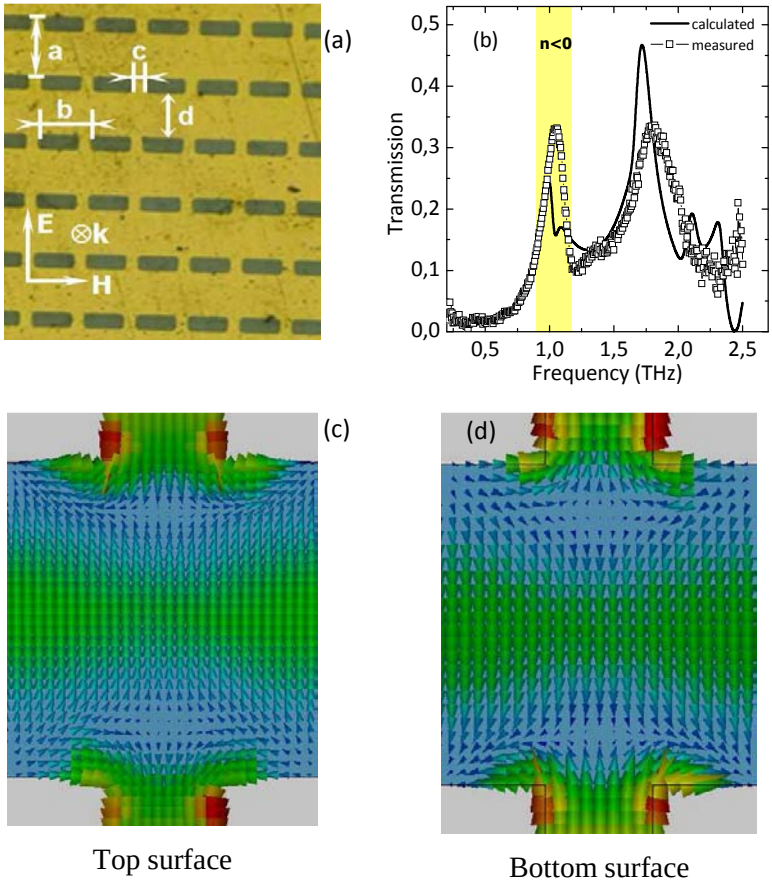

Figure 4.23: (a) Scanning electron microscopy image of the investigated double fishnet metamaterial fabricated by optical lithography technique, the geometrical dimensions are: a = 123 µm, b = 91µm, c = 20 µm, d = 90 µm, t = 50 µm. (b) Calculated (solid line) and measured (lines and symbols) transmission amplitude spectra of the studied sample for TM polarization. (c)-(d) Surface current distribution on top and bottom surfaces of the unit-cell fishnet structure, respectively at the resonant frequency (1THz).

The geometrical dimensions are provided in figure 4.23(a). The metamaterial was illuminated by a TM polarized THz wave at normal incidence (only this polarization exhibits interesting phenomena). Figure 4.22(b) shows an experimental and theoretical spectrum with two principal peaks near 1.0 THz and 1.8 THz. The theoretically predicted negative refractive index region is close to the first peak at 1 THz [highlighted zone in figure 4.23(b)]. Similarly as in the case of the subwavelength apertures-array and the single-layered fishnet structure, this extraordinary transmission is due to the surface plasmon polaritons (Ortuño, 2009, García-Meca, 2009, Kafesaki, 2007).

We have depicted in figures 4.23(c) and 4.23(d)) the calculated surface current distribution on top and bottom surfaces of the structure at the first internal-SPP mode located at the resonant frequency of about (1THz). The observed anti-parallel currents at the two facing metallic surfaces, which give rise to a Virtually Current Loop (VCL) between the metallic layers, are mainly induced by a strong resonance of magnetic nature (Huang, 2006). The other phenomenon observed is related to the current flows along the *E* direction near the so-called "neck" regions (Moreno, 2001). They are opposite to those located in the slab areas, thus producing transient charge localization in the zones where the two opposite currents meet each other.

Using standard retrieval method, effective electromagnetic parameters of our investigated metamaterial have been extracted from simulated transmission and reflexion coefficients and depicted in figure 4.24. One can see that the real part of the effective permeability reaches negative values within a frequency band that extends from 1.04 THz to 1.1 THz, approximately. The real part of the effective permittivity exhibits a Drude-like behavior with negative values below the electric plasma frequency f_p ~ 1.01 THz denoted by a row in figure 4.24(b). However, the effective refractive index does not reach negative values, because the regions where μ and ε are simultaneously negative do not overlap in frequency.

Indeed, the resonant magnetic frequency and the electric plasma frequency coincide, thus making impossible the existence of a negative refractive zone, as shown in figures 4.24(a)-(c). The reason is that the metallic parts (continuous wires along the direction of the electric field) of our investigated structure are too much diluted. A series of numerical simulations have been performed taking into account different widths of the so called neck-region of our fishnet metamaterial, (i.e. c = 20µm, 25µm and 30µm, respectively).

The results of our investigations show that the plasma frequency is shifted from 1.01 THz to 1.15 THz, approximately as illustrated in figure 4.24(d), while the negative effective permeability region remains substantially unchanged. We observe a minor shift of the magnetic resonant frequency from 1.04 to 1.075 THz, ~ 3% for the different aforementioned values of c. The negative refractive region in then expected. Indeed figure 4.24(d) shows that the refractive index varies from ~ 1.1 to – 1.7, approximately while c goes from 20 µm to 30 µm. Thus, c is considered as a very critical parameter in

the achievement of the negative refractive index region, which should be taken into account during the design procedure (not presented in figure 4.24(d) to avoid overloading the figure and for a graphical clarity).

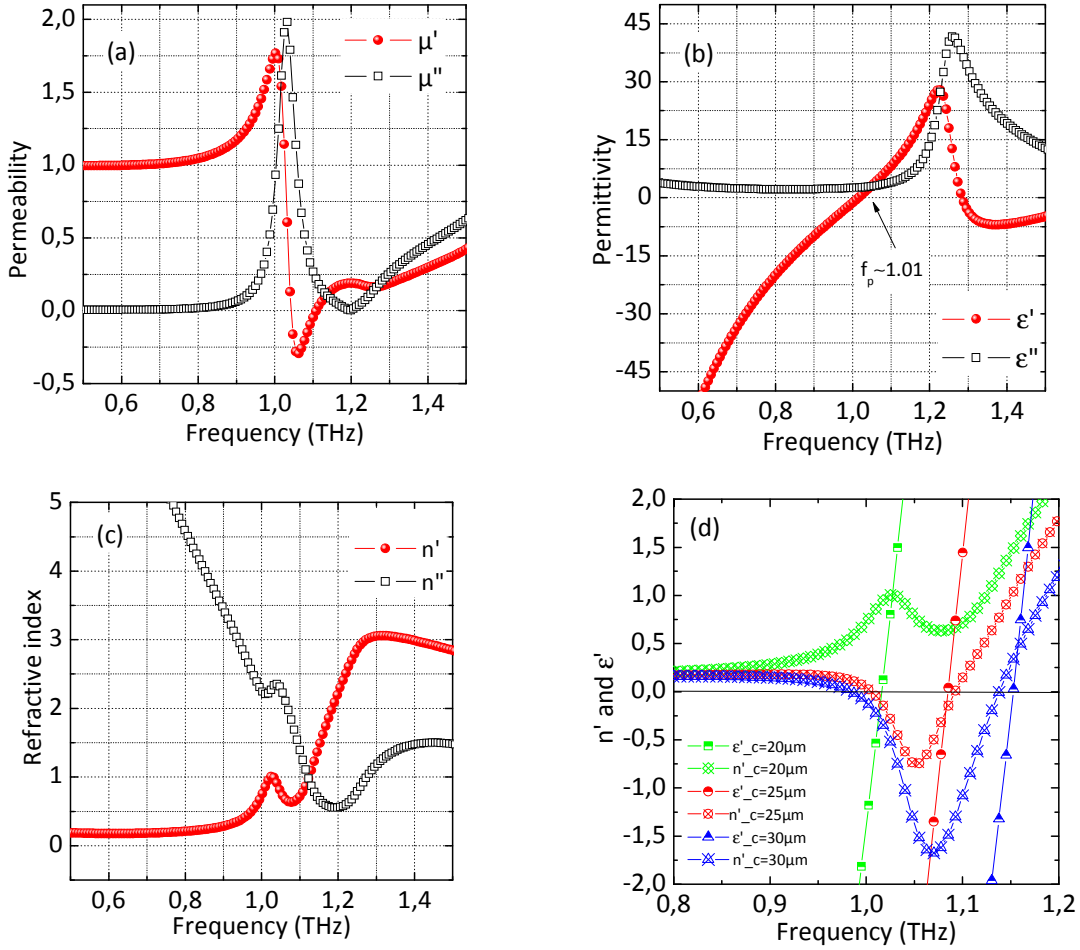

Figure 4.24: Extraction of effective parameters from the magnitude and the phase of transmission and reflexion spectra, (a) effective magnetic permeability, (b) effective electric permittivity, (c) effective refractive index, the plasma frequency $\boldsymbol{f_p}$ and the magnetic resonant frequency ***fm*** coincide ~ 1.01 THz. (d) Evolution of the effective refractive index and the electric plasma frequency for different values of the width ***c*** (***c***=20µm, 25µm and 30µm, respectively) of the so called "neck region" of our investigated fishnet metamaterial, ***c*** is considered as a very critical parameter in the establishment of the negative refractive index region.

4.7 Conclusion

In conclusion, we have investigated two main categories of metamaterials, All Dielectric metamaterials ($SrTiO_3$ rods and TiO_2 microparticles-layers) and composite metal-dielectric metamaterials (subwavelength apertures-array, single and double fishnet metallic layers), which have been designed, fabricated and characterized at terahertz frequency range. Different techniques of fabrication have been used to manufacture our experimental prototypes: optical lithography, laser micromachining, and chemical synthesis. Calculations based on Finite Element Method, and

Terahertz Time Domain Spectroscopy measurements have been performed in order to characterize and analyse the spectral response of our structures. A new approach of extraction has been proposed and used in order to retrieve all the effective parameters of our proposed metamaterials, at normal incidence with a single scan measurement. Fairly good agreements have been reported between calculations and measurements, but no clear negative permeability for TiO_2-based metamaterial layers, or negative refractive index for fishnet structures has been measured. Indeed, numerous physical and geometrical parameters play important roles in the effective responses and lot of samples are needed to separate without ambiguity each contribution to the overall behaviour.

Chapter 5

Conclusion, Outlooks and Publications of Author

5.1 Conclusion

To summarize, we have investigated (designed, fabricated and characterized) a large number of composite and all dielectric metamaterials that exhibit a wide variety of electromagnetic properties at desired frequencies in the microwave and terahertz regime.

The motivation of our work was highlighted at the beginning of the first chapter. The most remarkable properties of metamaterials exhibiting negative refractive index have been reminded and we have discussed some existing examples of structures which possess novel electromagnetic properties. We have also seen that the key to describe these structures as effective homogeneous media was that the structures possess features much less than the operating wavelength.

A brief overview about the large panel of existing numerical calculation methods, which are considered nowadays as an inherent tool in the study of electromagnetic structures, has been given in the first part of the second chapter. The second part of chapter 2 was dedicated to the description of the experimental setups that we have used in order to carry out experimental measurements with our fabricated structures. Indeed, both free space setup based on Vector Network Analyzer (VNA) and horn antennas and Terahertz Time Domain Spectroscopy (THz-TDS) have been presented in the microwave regime and terahertz frequency range, respectively. These two characterization techniques offer indeed, the possibility to perform free-contact measurements without damaging the considered sample.

The third chapter of this dissertation includes all results that have been obtained at microwave frequencies on different categories of composite metal-dielectric structures. Starting by a simple Frequency Selective Surface (FSS) acting as a bandpass filter, this latter has been the subject of intense investigations. Indeed, the selectivity of the studied FSS is considerably enhanced when stacking several layers. The angular robustness of the transmission response was demonstrated, and an original technique has been proposed in order to obtain tunability on the spectral response. Furthermore, the FSS has been used as a Partially Reflecting Surface in a Fabry-Pérot cavity antenna where the radiation patterns have shown a highly directive emission of about 20 dB. Fishnet metamaterials exhibiting a negative refractive index have also been investigated, effective parameters have been extracted using the standard retrieval method and the negative refraction effect was demonstrated numerically and experimentally.

The fourth chapter of this dissertation was dedicated to the study of metamaterials in the terahertz regime. Two main categories of metamaterials have been investigated. We have started by All Dielectric (AD) metamaterials that are considered as the best alternative in the fabrication of isotropic and low-loss metamaterials. Experimental prototypes have been fabricated using both laser micromachining technique and chemical synthesis, and measurements have been performed using THz-TDS. The second category of our investigated metamaterials is the so called fishnet structures.

Numerical simulations have been performed using full wave commercial 3D calculator in order to predict the spectral response of our investigated metamaterials as it was the case in all our previous studies. Experimental demonstrators have been fabricated and measurements have been performed using THz-TDS. Some unexpected anomalies related to experimental results (not predicted by simulations) have been outlined and their origins have been analyzed and discussed.

5.2 Outlooks

There are several immediate paths for improvement and application of structures presented in this dissertation.

Initially, we plan to demonstrate experimentally the mechanical tunability effect on the spectral response of the double-FSS that we have proposed in chapter 3. Indeed, our investigated double-FSS can be mounted on a mechanical support system, which is widely used in optics and offers a possibility of translation in the following three directions of the space $\boldsymbol{x}$, $\boldsymbol{y}$ and $\boldsymbol{z}$. Thus, the tunability effect can be achieved experimentally. Furthermore, the effect of the air gap $\boldsymbol{g_{air}}$ separating each layer of the double-FSS can also be studied. Staying in the field of spatial filtering and antenna applications, we propose to investigate a dual-band metasurface operating at 2.45 GHz and 5.8 GHz (WIFI- band) that will be applied as a Partially Reflecting Surface (PRS) in a Fabry-Pérot (FP) cavity with the main goal to enhance the directivity of printed patch antennas for wireless communications. Preliminary investigations have already shown rather good results, which makes the metasurface promising in telecommunication applications. Furthermore, the tunability of the spectral response of the double-FSS that has been achieved mechanically in chapter 3 will be applied in the Fabry-Pérot (FP) cavity in order to demonstrate the beam steering of the metasutface-based antenna. These works will be performed in collaboration with our colleagues of the Institut d'Electronique Fondamentale, from the University of Paris-Sud 11.

In the field of millimetre imaging and sub-wavelength focusing we have started to perform a series of experiments on a flat-lens based on the holes-array fishnet metamaterial that has been investigated in chapter 3. Indeed, the investigated flat-lens is made of 5 stacked layers separated by an air gap of about 0.5 mm, which have been designed for an operating frequency of about 85 GHz. The basic metamaterial constituting our flat lens exhibit a refractive index of about -4 at 85 GHz, and the preliminary experiments show rather good results. Indeed, as illustrated in figure 5.1(b), for two different positions of the lens 25 cm and 50 cm from the aperture of the horn antenna, we can clearly see a focusing effect in the shape of the incident beam, which is indeed much more spatially confined in the presence of the flat lens. Further numerical simulations and experiments should be performed taking into account a new design and a new experimental demonstrator exhibiting an effective

refractive index of – 1 at the desired frequency in order to satisfy an impedance matching between the lens and the free space, which is an important condition for sub-wavelength focusing (Pendry, 2000).

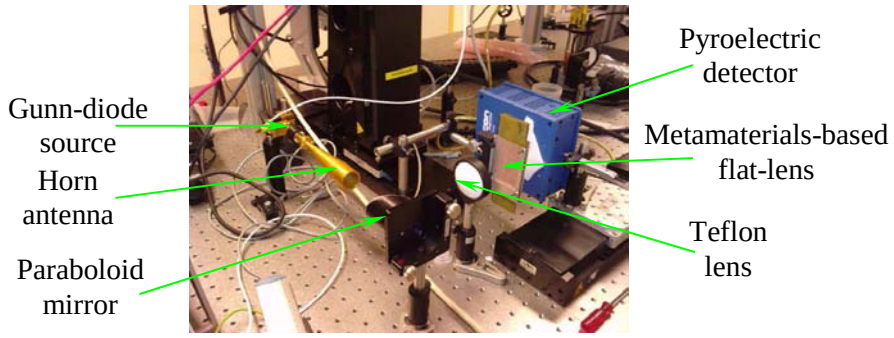

(a)

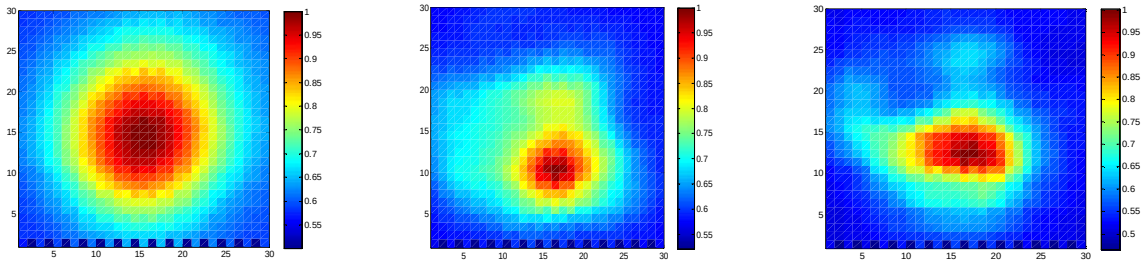

(b) (c) (d)

Figure 5.1: Experimental setup for "millimeter imaging" including a metamaterials-based flat lens for an operating frequency of about 85 GHz. Demonstration of the focusing effect on the incident beam: (b) incident beam at the output of the horn antenna, without the presence of the flat-lens, (c)-(d) the flat-lens is placed at 25 cm and 50 cm, respectively from the aperture of the horn antenna. The maps represent the square of the magnitude of the radiated electric field $|E^2|$.

At the beginning of the fourth chapter, related to all dielectric metamaterials, we have demonstrated the tunability of the spectral response of SrTiO3-based rods-array metamaterials by changing the temperature. Works in progress, carried out in collaboration with our colleagues of the Institute of Physics of Prague in the Czech Republic are directed to frequency tunability by applying an electric field.

The preliminary results of the effective parameters that have been obtained in the random samples based on TiO_2-mocroparticles can be improved by additional processing. Indeed, with the control of particle sizes, shapes, materials, filling factor and size ration, we will be able to obtain the desired electromagnetic property at the desired frequency. For example, a negative refractive index can be achieved by ensuring that the frequency regions of negative μ and ε overlap, thus by controlling the aforementioned critical parameters. Actually, the second fabrication process based on microchemistry and spry drying technique, which has been described in chap. 4, sec. 4.4 is still under intense investigations and can offer a potential possibility to reach our goal (see figures 4.14(a) and 4.15(b)).

In the second part of the fourth chapter related to the composite metal-dielectric metamaterials involving surface plasmons, the experimental results (unexpected high level of transmission around 0.5 THz) that have been obtained on the sub-wavelength aperture-array might be improved in conformity with simulations, using a low-loss and non dispersive dielectric substrate. Furthermore, by making sure that the thicknesses of the top and bottom metallic layers are much larger than the skin depth of the metal, at the corresponding frequency. Our investigated subwavelength apertures and fishnet structures, can offer the possibility for sensing applications based on surface plasmons, since these later are being nowadays explored for their potential in subwavelength optics, data storage, light generation, microscopy and bio-photonics.

5.3 Publications of Author

Parts of the content of this dissertation have been the subject of the following publications:

5.3.1 Journal articles

- **Raid Yahiaoui**, Shah Nawaz Burokur, Valérie Vigneras, André de Lustrac, Patrick Mounaix, ″Investigation of spatial filters at microwave frequencies : application for antenna directivity enhancement," Submitted for publication: Microwave and Optical Technology Letters.
- **R. Yahiaoui**, H. Němec, P. Kužel, F. Kadlec, C. Kadlec, and P. Mounaix, ″Tunable THz metamaterials based on an array of paraelectric $SrTiO_3$ rods,″ Appl. Phys. A., **103**, 689 (2011)
- **Riad Yahiaoui**, Valérie Vigneras, Patrick Mounaix, "Theoretical and experimental investigations of easy made fishnet metamaterials at microwave frequencies," Appl. Phys. A., 103, **685** (2011).
- **R. Yahiaoui**, H. Nemec, P. Kužel, F. Kadlec, C. Kadlec, J. Schilling, M. Bari, J. C. Delagnes and P. Mounaix, ″Investigation of metamaterials for terahertz frequency range,″ Proc. SPIE 7917, 79170E (2011).
- **R.Yahiaoui**, H. Němec, P. Kužel, F. Kadlec, C. Kadlec, and P. Mounaix, ″Broadband dielectric terahertz metamaterials with negative permeability,″ Opt. Lett. **34**, 3541 (2009).
- H. Němec, P. Kužel, F. Kadlec, C. Kadlec, **R.Yahiaoui** and P. Mounaix, ″Tunable terahertz metamaterials with negative permeability,″ Phys. Rev. B **79**, 241108(R) (2009).
- **R. Yahiaoui**, S. N. Burokur, A. de Lustrac, ″Enhanced directivity of an ultra-thin metamaterial-based cavity antenna fed by a multisource,″ Electron. Lett. **45**, 814 (2009).
- Shah Nawaz Burokur , **Riad Yahiaoui**, André de Lustrac, ″Subwavelength metamaterial-based resonant cavities fed by multiple sources for high directivity,″ Microwave Opt. Technol. Lett. **41**, 1883 (2009).
- Abdelwaheb Ourir, Shah Nawaz Burokur, **Riad Yahiaoui**, André de Lustrac, ″Directive metamaterial-based subwavelength resonant cavity antennas – Applications for beam steering,″ Comptes Rendus Physique. **10**, 414 (2009).

5.3.2 International Conference Presentations

- **Riad Yahiaoui**, Patrick Mounaix, Valérie Vigneras, U-Chan Chung, Mario Maglione, Catherine Elissalde, Sylvain Lannebere and Ashod Aradian, “Artificial magnetism in Titanium Dioxide (TiO_2) microparticles array for terahertz applications,” NANOMETA-2011, 3rd International Topical Meeting on Nanophotonics and Metamaterials, Seefeld ski resort, Tirol, Austria, January 3 - 6 (2011), Poster.
- **Riad Yahiaoui**, Patrick Mounaix, Hynek Němec, Filip Kadlec, Christelle Kadlec and Petr Kužel, “Negative refractive index induced by surface plasmon polaritons in sub-wavelength apertures array,” NANOMETA-2011, 3rd International Topical Meeting on Nanophotonics and Metamaterials, Seefeld ski resort, Tirol, Austria, January 3 - 6 (2011), Poster.
- Hynek Němec, Filip Kadlec, Christelle Kadlec, Petr Kužel, **Riad Yahiaoui** and Patrick Mounaix, “Determination of effective optical properties of metamaterial targeted for terahertz spectral range,” NANOMETA-2011, 3rd International Topical Meeting on Nanophotonics and Metamaterials, Seefeld ski resort, Tirol, Austria, January 3 - 6 (2011), Poster.
- **R.Yahiaoui**, H. Němec, P. Kužel, F. Kadlec, C. Kadlec, J. Schilling, M. Bari, and P. Mounaix, "Investigation of metamaterials for terahertz frequency range," SPIE Photonics West, San Francisco, California, USA, 22 - 27 January (2011), Oral.
- **R.Yahiaoui**, H. Němec, P. Kužel, F. Kadlec, C. Kadlec, J. Schilling, M. Bari, and P. Mounaix, "Fishnet metamaterials on thin polymer film for terahertz applications ," IRMMW

2010 – 35th International Conference on Infrared Millimeter, and Terahertz Waves, Rome, Italy, September 5 – 10 (2010), Oral.

- **Riad Yahiaoui**, Valérie Vignéras, Patrick Mounaix, ″Theoretical and experimental investigations of easy made fishnet metamaterials at microwave frequencies,″ META'10 - 2nd International Conference on Metamaterials, Photonic crystals and Plasmonics, Cairo, Egypt, February 22 – 25 (2010), Poster.
- **R.Yahiaoui**, H. Němec, P. Kužel, F. Kadlec, C. Kadlec, and P. Mounaix, ″Tunable metamaterials based on an array of ferroelectric $SrTiO_3$ rods for THz applications,″ META'10 - 2nd International Conference on Metamaterials, Photonic crystals and Plasmonics, Cairo, Egypt, February 22 – 25 (2010), Oral.
- Hynek Němec, Filip Kadlec, Christelle Kadlec, Petr Kužel, **Riad Yahiaoui**, and Patrick Mounaix, ″Tunable Metamaterials with Negative Permeability in THz Range,″ IRMMW 2009 – 34rd International Conference on Infrared Millimeter, and Terahertz Waves, Busan, Korea, September 21 – 25 (2009)
- Hynek Němec, Petr Kužel, **Riad Yahiaoui**, and Patrick Mounaix, ″Dielectric Tunable Metamaterials with Negative Permeability in Terahertz Range,″ CLEO 2009 - Conference on Lasers and Electro-Optics, Baltimore, Maryland, USA, May 31 – June 5 (2009).
- S. N. Burokur, **R. Yahiaoui**, A. de Lustrac, ″Subwavelength resonant cavities fed by microstrip patch array,″ IWAT 2009 - International Workshop on Antenna Technology, Santa Monica, California, USA, March 2 – 4 (2009).
- **R. Yahiaoui**, S. N. Burokur, A. de Lustrac, ″Multisources fed metamaterial-based cavities for directivity enhancement,″ ISAP 2008 - International Symposium on Antennas and Propagation, Taipei, Taiwan, October 27 – 30 (2008).

5.3.3 Local-French Conference Presentations

- **Riad Yahiaoui**, Hynek Němec, Filip Kadlec, Christelle Kadlec, Petr Kužel, Patrick Mounaix "Negative refraction effect assisted by surface plasmon polaritons at terahertz frequency range," 6ièmes Journées THz, La Grande-Motte, Montpellier, 25 – 27 Mai (2011), Poster.
- **Riad Yahiaoui**, Valérie Vigneras, Patrick Mounaix "Negative refractive index metamaterials for millimetre applications," 6ièmes Journées THz, La Grande-Motte, Montpellier, 25 – 27 Mai (2011), Oral.
- **Riad Yahiaoui**, Valérie Vigneras, U-Chan Chung, Mario Maglione, Catherine Elissalde, Sylvain Lannebere, Ashod Aradian and Patrick Mounaix "All dielectric metamaterials at terahertz regime," 6ièmes Journées THz, La Grande-Motte, Montpellier, 25 – 27 Mai (2011), Oral.
- **Riad Yahiaoui**, Valérie Vignéras, et Patrick Mounaix, "Métamatériaux entièrement diélectriques et nouvelle approche de caractérisation en bande térahertz," 14ièmes Journées Nationales du Réseau Doctoral en Microélectronique, Paris, 23 – 25 Mai (2011), Oral.
- **Riad Yahiaoui**, Valérie Vignéras, U-Chan Chung, Mario Maglione, Catherine Elissalde, Sylvain Lannebère, Ashod Aradian et Patrick Mounaix, "Métamatériaux à base de microparticules de TiO_2 dans la gamme térahertz," 17ièmes Journées Nationales Microondes, Brest, 18 – 20 Mai (2011), Oral.
- **Riad Yahiaoui,** Valérie Vigneras et Patrick Mounaix, "Métamatériaux compatibles avec les techniques de fabrication de masse pour applications en bande millimétrique," Colloque National Métamatériaux, Paris, 14 - 15 Mars (2011), Poster.
- **Riad Yahiaoui**, Hynek Němec, Filip Kadlec, Christelle Kadlec, Petr Kužel et Patrick Mounaix, "Métamatériaux fishnet et ouvertures sub-longueurs d'ondes," Colloque National Métamatériaux , Paris, 14 - 15 Mars (2011), Poster.
- **Riad Yahiaoui**, Riad Yahiaoui, Valérie Vignéras, U-Chan Chung, Mario Maglione, Catherine Elissalde, Sylvain Lannebère, Ashod Aradian et Patrick Mounaix, "Métamatériaux

entièrement dielectriques pour applications submillimétriques," Colloque National Métamatériaux, Paris, 14 - 15 Mars (2011), Poster.

- **Riad Yahiaoui**, Valérie Vignéras, Patrick Mounaix, "Caractérisation de métamatériaux auto-assemblés pour des applications millimétriques et submillimétriques," Séminaire doctorants CPMOH, Bordeaux, 04 Novembre (2010), Oral.
- **Riad Yahiaoui**, Valérie Vignéras, Patrick Mounaix, "Caractérisation de métamatériaux pour applications millimétriques et submillimétriques," Séminaire doctorants IMS, Bordeaux, 19 Juillet (2010), Oral.
- **Riad Yahiaoui**, Valérie Vignéras, Patrick Mounaix, "Approches théorique et expérimentale de dispositifs planaires pour des applications de filtrage spatial en bande millimétrique," 13ièmes Journées Nationales du Réseau Doctoral en Microélectronique, Montpellier, 7 – 9 Juin (2010), Poster.
- **Riad Yahiaoui**, Hynek Němec, Petr Kužel, Filip Kadlec, Christelle Kadlec, Patrick Mounaix, "Magnétisme artificiel accordable induit par des barreaux de Strontium Titanate (SrTiO3) dans la gamme THz," Journée de l'Ecole Doctorale SPI 2010, Bordeaux, 27 Mai (2010), Poster.
- **Riad Yahiaoui**, Valérie Vignéras, Patrick Mounaix, ″Caractérisation de métamatériaux à indice de réfraction négatif en bande millimétrique,″ 11ièmes Journées de Caractérisation Microondes et Matériaux, Brest, 31 Mars – 2 avril (2010), Oral.
- **Riad Yahiaoui**, Valérie Vignéras, Patrick Mounaix, ″Métamatériaux à indice de réfraction négatif en bande millimétrique,″ Journée de l'IPF, Bordeaux, 12 novembre (2009), Poster. (Lauréat du meilleur poster)
- **Riad Yahiaoui**, Laurent Oyhenart , Valérie Vignéras et Patrick Mounaix, ″Structures métal diélectrique microusinées par laser pour applications à 600 GHz, ″ 5ièmes Journées THz, Lille, 10-12 juin (2009), Poster.
- **Riad Yahiaoui**, Lauent Oyhenart , Valérie Vignéras et Patrick Mounaix, ″Conception de structures de type « fishnet » pour une fonctionnalité en haut de bande millimétrique,″ 16ièmes Journées Nationales Microondes, Grenoble, 27 – 29 Mai (2009), Poster.
- Shah Nawaz Burokur, **Riad Yahiaoui**, André de Lustrac, ″Excitation multi-sources pour l'amélioration de la directivité dans des antennes à cavités,″ 16ièmes Journées Nationales Microondes, Grenoble, 27 – 29 Mai (2009), Poster.

Appendix A

Description of the Extraction Method

In this appendix, we will describe in details the most commonly retrieval method, used in order to retrieve the complex constitutive (***ε****, ***μ****) and propagative (***n****, ***z****) parameters from the scattering element matrix Sij. Figure A.1 shows a planar sample of thickness *d* placed in free space. The complex electric permittivity and the complex magnetic permeability, relative to free space, are defined as follows:

$$\varepsilon^* = \varepsilon' - i\varepsilon'' = \varepsilon'\left(1 - i\tan\left(\delta_\varepsilon\right)\right), \tag{A.1}$$

$$\mu^* = \mu' - i\mu'' = \mu'\left(1 - i\tan\left(\delta_\mu\right)\right), \tag{A.2}$$

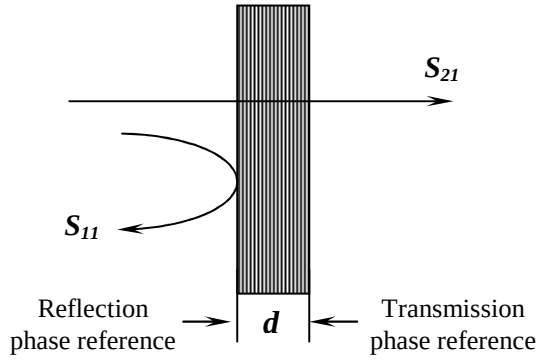

Figure A.1: Illustration of transmission and reflection coefficients through a planar sample with thickness ***d***, reference planes are defined for both transmission and reflection phases.

It is assumed that the planar sample is of infinite extent laterally so that diffraction effects at the edges can be neglected. A linearly polarized, uniform plane wave of frequency w is normally incident on the sample. The reflection and transmission coefficients S_{11} and S_{21} are obtained in free space for the normally incident plane wave. By applying boundary conditions at the air-sample interfaces in figure A.1, it can be shown that the S_{11} and S_{21} parameters are related to the parameters and Γ and T by the following equations:

$$S_{11} = \frac{\Gamma\left(1 - T^2\right)}{1 - \Gamma^2 T^2}, \tag{A.3}$$

$$S_{21} = \frac{T\left(1 - \Gamma^2\right)}{1 - \Gamma^2 T^2}, \tag{A.4}$$

Where Γ and T are the reflection and the transmission coefficients of the air-sample interface, respectively and are given by:

$$\Gamma = \frac{(Z_{nc} - 1)}{(Z_{nc} + 1)}, \tag{A.5}$$

$$T = e^{-\gamma d}, \tag{A.6}$$

Where $\boldsymbol{Z_{nc}}$ and $\boldsymbol{\gamma}$ are the normalized characteristic impedance and propagation constants of the sample. They are related to $\boldsymbol{\varepsilon^*}$ and $\boldsymbol{\mu^*}$ by the following relationships:

$$\gamma = \gamma_0 \sqrt{\varepsilon^* \mu^*}, \tag{A.7}$$

$$Z_{nc} = \sqrt{\frac{\varepsilon^*}{\mu^*}}, \tag{A.8}$$

Where $\boldsymbol{\gamma_0} = (\boldsymbol{i}2\pi/\boldsymbol{\lambda_0})$ represents the propagation constant of free space, and $\boldsymbol{\lambda_0}$ is the free-space wavelength. From (A.3) and (A.4), $\boldsymbol{\Gamma}$ and $\boldsymbol{T}$ can be written as:

$$\Gamma = K \pm \sqrt{K^2 - 1}, \tag{A.9}$$

Where

$$K = \frac{S_{11}^2 - S_{21}^2 + 1}{2S_{11}}, \tag{A.10}$$

$$T = \frac{S_{11} + S_{21} - \Gamma}{1 - (S_{11} + S_{21})\Gamma}, \tag{A.11}$$

In (A.9) the plus or minus sign is chosen such that $|\Gamma| < 1$. Using (A.6), the complex propagation constant $\boldsymbol{\gamma}$ can be written as following:

$$\gamma = [\log_e(1/T)]/d, \tag{A.12}$$

Where $\boldsymbol{d}$ is the thickness of the sample along the direction of propagation, from (A.5) and (A.8),

$$\sqrt{\frac{\mu^*}{\varepsilon^*}} = \frac{1+\Gamma}{1-\Gamma}, \tag{A.13}$$

From (A.7) and (A.13), we obtain

$$\varepsilon^* = \frac{\gamma}{\gamma_0}\left(\frac{1-\Gamma}{1+\Gamma}\right), \tag{A.14}$$

$$\mu^* = \frac{\gamma}{\gamma_0}\left(\frac{1+\Gamma}{1-\Gamma}\right), \tag{A.15}$$

Since the parameter $\boldsymbol{T}$ in the expression of $\boldsymbol{\gamma}$ in (A.12) is a complex number, there are multiple values for $\boldsymbol{\gamma}$. If $\boldsymbol{T}$ is defined as $\boldsymbol{T} = |\boldsymbol{T}|\boldsymbol{e^{j\varphi}}$, then $\boldsymbol{\gamma}$ is given by:

$$\gamma = [\log(1/|T|)]/d + j\left[\frac{2\pi n - \phi}{d}\right], \tag{A.16}$$

Where n=0, ±1, ±2, …, the real part of γ is unique and single valued, but the imaginary part of γ has multiple values, So equations (1.14) and (1.15) will give multiples values of ε^* and μ^*. Te phase constant β is defined as:

$$\beta=(2\pi/\lambda_m) = \text{imaginary part of } (\gamma), \tag{A.17}$$

Where λ_m is the wavelength in the sample material from equations (A.16) and (A.17), d/λ_m can be expressed as follows:

$$d/\lambda_m = n - \frac{\phi}{2\pi}, \tag{A.18}$$

For n=0, and $-2\pi<\phi<0$, (d/λ_m) is between 0 and 1. If the sample thickness d is chosen such that it is less then λ_m, equations (A.14) and (A.15) will give unique values of ε^* and μ^* which corresponds to n=0. The ambiguity related to ε^* and μ^* can then be resolved. The wave impedance and the refractive index can be deduced from the following expressions:

$$z = \sqrt{\frac{\mu^*}{\varepsilon^*}}, \tag{A.19}$$

$$n = \sqrt{\mu^* \varepsilon^*}, \tag{A.20}$$

Appendix B

Electromagnetic Field Diffraction on Dielectric Spherical Particles

Spherical resonators have received much theoretical attentions, since they offer possibilities to design isotropic metamaterials (Yannopapas, 2005, Wheeler, 2005, Jylhä, 2006, Seo, 2006, Ahmadi, 2008). The modelling of electromagnetic response of spherical inclusions embedded in a host material is based on the generalized Lewin's model (Lewin, 1947). Originally, the Lewin's model has been specified only for spherical particles with the same radius ***a*** arranged in a cubic lattice with the lattice constant ***s***. But an expansion of the model for the case of two sub-lattices of dielectric spherical particles with different radii makes possible to describe the DNG media (Vendik, 2004). The spheres are assumed to resonate either in the first or second resonance mode of the Mie theory (Kong, 2005). Let us consider the diffraction of a plane electromagnetic wave with amplitude of the electric field E_0 linearly polarized along *x*- axis, the wave propagates along the *z*- axis as illustrated in figure C.1:

$$\vec{E}(z,t)=\vec{e}_x E_0 e^{i(\omega t-k_2 z)}, \vec{H}(z,t)=\vec{e}_y \frac{k_2}{\omega\mu_0} E_0 e^{i(\omega t-k_2 z)}, \qquad \text{(C.1)}$$

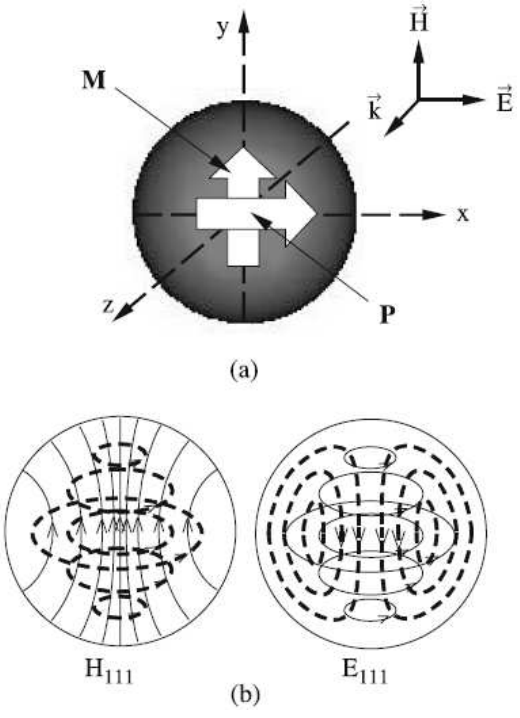

Figure B.1: Spherical particle in the field of linearly polarized electromagnetic wave and field distribution in the equatorial plane: (a) dipole momentum of electric polarization of the particle **P**, and dipole momentum of magnetization of the particle **M** (b) and (b) mode charts of the dominant *H*111 and *E*111 modes in spherical resonator with magnetic walls. Solid and dashed lines show the magnetic and electric field lines, correspondingly (Vendik, 2006).

In order to fulfil the boundary conditions on the surface of the spherical particle, with respect to tangential components of electric and magnetic fields, expansion of the incident plane wave in terms of spherical function is used. The spherical modes inside the sphere and spherical modes propagating in open space outside the sphere are taken into consideration as well. The boundary conditions give rise to two pairs of non-homogeneous equations with respect to complex amplitudes of the spherical functions inside and outside the spherical particle. The fields inside the spherical particle can be written as a multipole development (Bohren, 2004):

$$\vec{E}^{(in)}(r,\theta,\varphi) = E_0 \sum_{l=1}^{\infty} i^l \frac{2l+1}{l(l+1)} \left(a_l^{(in)} \vec{m}_{01l} - i b_l^{(in)} \vec{n}_{e1l} \right), \tag{C.2}$$

$$\vec{H}^{(in)}(r,\theta,\varphi) = -\frac{k_1}{\omega\mu_0} E_0 e^{i\omega t} \sum_{l=1}^{\infty} i^l \frac{2l+1}{l(l+1)} \left(b_l^{(in)} \vec{m}_{e1l} + i a_l^{(in)} \vec{n}_{o1l} \right), \tag{C.3}$$

Where $\vec{m}_{0/e,m,l}$ and $\vec{n}_{0/e,m,l}$ are spherical wave functions (odd and even). The number m=1 is taken is equations (4.3) and (4.4), as far as the incident wave in open space is linearly polarized. The wave numbers are defined as

$$k_1 = \omega\sqrt{\varepsilon_0\varepsilon_1\mu_0}, \quad k_2 = \omega\sqrt{\varepsilon_0\varepsilon_2\mu_0}, \tag{C.4}$$

Where ε_0 and μ_0 are dielectric permittivity and permeability of free space, ε_1 and ε_2 are the relative permittivities of the spherical particle and matrix material respectively. The solutions of the system of equations specified by boundary conditions are resulted for amplitudes of the waves inside the spherical particle in the following form:

- For the waves of magnetic type (E_r=0, figure C.1, left)

$$a_l^{(in)} = \frac{n\psi_l(nka)\psi_l'(ka) - \psi_l(ka)\psi_l'(nka)}{n\xi_l(nka)\xi_l'(ka) - \xi_l(ka)\xi_l'(nka)}, \tag{C.5}$$

- For the waves of electric type (H_r=0, figure C.1, right)

$$b_n^{(in)} = \frac{\psi_l(nka)\psi_l'(ka) - n\psi_l(ka)\psi_l'(nka)}{\psi_l(nka)\xi_l'(ka) - n\xi_l(ka)\psi_l'(nka)}, \tag{C.6}$$

Where n is the index, a is the radius of the spherical particle, $\psi_l(x)$ and $\xi_l(x)$ are the Ricatti-Bessel functions. The resonant frequencies are calculated numerically, and are called "Mie resonances", according to the pioneering work of Gustav Mie in 1908 related to the scattering of light by dielectric spherical particles (Mie, 1908).

Appendix C

SSMM: Single Scan Measurement Method

Effective dielectric permittivity and magnetic permeability can be in principle determined from complex transmittance and reflectance spectra (Smith, 2002). In the case of time-domain THz spectroscopy of bulk samples the multiple internal reflections of the THz beam in the sample result in a series of mutually time-delayed echoes in the transmitted beam. The time-windowed data corresponding to individual echoes then can be used for the simultaneous retrieval of the dielectric and magnetic response (Němec, 2006). The subwavelength thickness of the investigated structures prevents us from a direct application of the latter method. At the same time, accurate phase-sensitive measurements of the reflectance is still rather challenging for this kind of samples (Pashkin, 2003). Here we adapt and optimize the method first demonstrated in (Němec, 2009) which takes advantage of temporally resolved internal reflections in a thick wafer attached to the (thin) metamaterial. We enclose the flexible metamaterial film between two thick sapphire wafers as depicted in figure C. 1(a). In this arrangement, possible unwanted air gaps between the metamaterial and the wafers can be substantially reduced. Moreover, by this configuration the metamaterial is entirely embedded in a medium with a homogeneous refractive index and not positioned at an interface between two different media, as reported previously by (Němec, 2009). The wafers should be sufficiently thick to allow temporal windowing and a good spectral resolution which depends on the time window length (Duvillaret, 1996, Kužel, 2000). The thicknesses of the wafers should be also quite different from each other in order to avoid mixing of internal reflections coming from the two wafers. Here we used 1.93 mm and 3.86 mm thick Sapphire ($\varepsilon_r \sim 9.6$, measured by THz-TDS) wafers, respectively, the first echo is thus delayed by 44 and 88 ps, respectively (see figure C. 1(b)). The second echo of the thinner wafer thus appears at the same time as the first echo of the thicker wafer (but none of them is required in the subsequent analysis). The direct pass through the entire block contains information about the metamaterial transmittance whereas the first echo of the thinner wafer depends on the product of metamaterial transmittance and reflectance. Formally, we can express the metamaterial transmittance T and reflectance R as follows:

$$T = \frac{E_0^{\mathrm{AMB}} E^{\mathrm{ref}}}{E_0^{\mathrm{A}} E_0^{\mathrm{B}}} \cdot T_{\mathrm{AV}} T_{\mathrm{VB}} \quad \text{and} \quad R = \frac{E_1^{\mathrm{AMB}} E_0^{\mathrm{A}}}{E_1^{\mathrm{A}} E_0^{\mathrm{AMB}}} \cdot R_{\mathrm{AV}}, \tag{4.6}$$

Where various E-fields stand for the Fourier transforms of the waveforms measured in the following situations (see also the scheme in figure 4.18(a)). The subscripts 0 and 1 refer to the direct pass and to the 1st echo (in the thinner wafer), respectively. The superscripts A, B, AMB and ref denote the signal obtained with the thinner wafer, the thicker wafer, the assembly of wafers with

metamaterial, and no object in the beam path, respectively. Accurate phase determination is ensured by the reference measurement of the separate silicon wafers (spectra E_0^{A}, E_1^{A}, and E_0^{B}). It is thus essential that the wafers have an excellent parallelism so that a small lateral shift does not introduce a systematic error in the phase. The coefficients T_{AV} and T_{VB} stand for theoretical expressions for the transmittance of the wafer A – vacuum and vacuum – wafer B interface, respectively; R_{AV} describes the reflectance on the wafer A – vacuum interface.

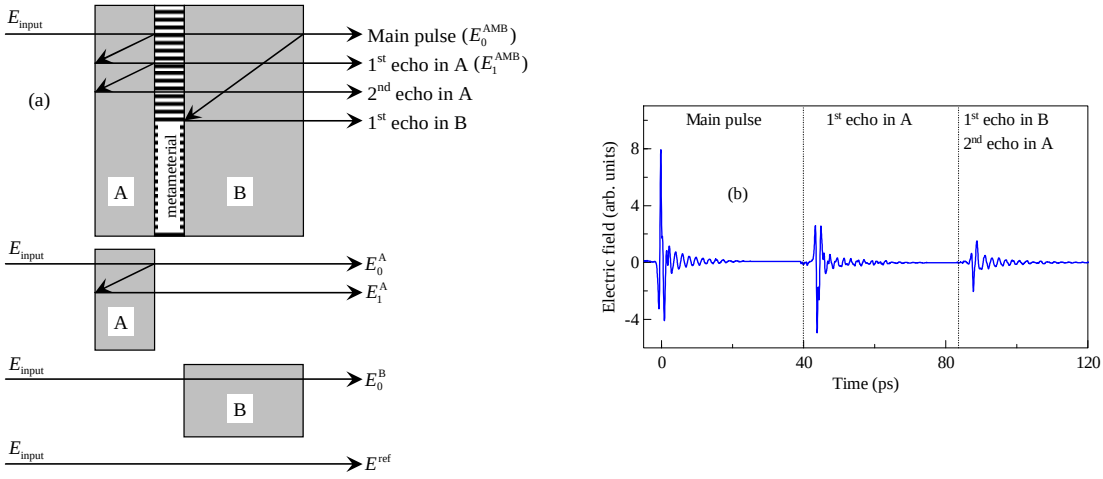

(a) (b)

Figure C.1: (a) Scheme of the arrangement for transmittance and reflectance measurement, along with the sketch of all required reference signals. The THz beam is shifted upon reflections only for graphical clarity. (b) Illustration of a typical waveform obtained in the experiment. Note that the second pulse is a superposition of the first internal reflection in the thick wafer with the second internal reflection in the thin wafer.

Appendix D

Characterization of TiO2 Crystal – Abacus Benchmark

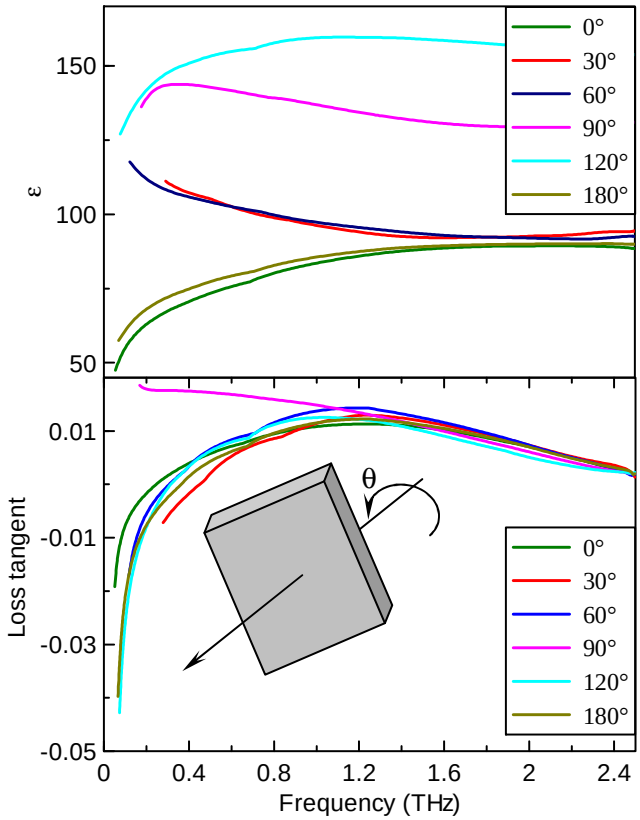

Figure D.1: Measured relative dielectric permittivity $\boldsymbol{\varepsilon}$ and loss tangent tan($\boldsymbol{\delta}$) of a 1.55mm thick TiO_2 single crystal for different positions $\boldsymbol{\theta}$ of the sample illiminated at normal incidence, as illustrated in the insert. The measurements have been performed using THz-TDS.

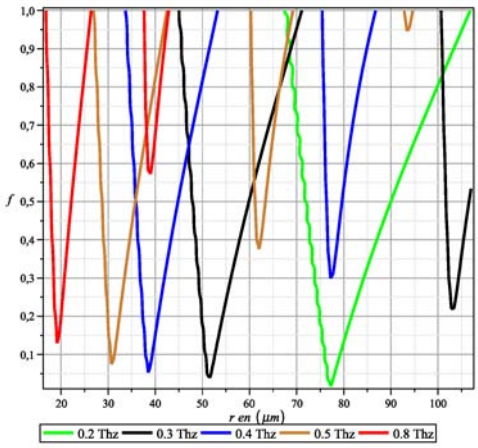

Figure D.2: Illustration of the domains within the effective permeability is negative for a given material based on TiO_2 spheres in the air. The spheres are characterized by a radius $\boldsymbol{r}$, and a volume fraction $\boldsymbol{f}$. The calculations have been obtained by implementing Maxwell Garnet theory (Lannebère, 2010).

Bibliography

(Acher, 2009) Acher, O. J. Magn. Magn. Mater., **321**. 2093 (2009).

(Adam, 2002) Adam, J.D., Davis, L.E., Dionne, G.F., Schloemann, E.F., and Stitzer, S.N. IEEE Trans. On MTT, **50**, 721 (2002).

(Adomavicius, 2002) Adomavicius, R., Urbanowicz, A., Molis, G., Krotkus, A., and Satkovskis, E. Appl. Phys. Lett. 85, 2463 (2004).

(Ahmadi, 2008) Ahmadi, A., and Mosallaei, H. Phys. Rev. B., **77**, 045104, (2008).

(Alitalo, 2006) Alitalo, P., Maslovski, S., Tretyakov, S. J. Appl. Phys., **99**, 124910 (2006).

(Amiri, 2007) Amiri, P. K., Rejaei, B., Zhuang, Y., Vroubel, M., Burghartz, J. N. L. IEEE Trans. Magn. 43, 2630 (2007).

(Ascázubi, 2005) Ascázubi, R., Shneider, C., Wilke, I., Pino, R., and Dutta, P. S. Phys. Rev. B **72**, 045328 (2005)

(Auston, 1980) Auston, D. H., Johnson, D. H., Smith, P. R., and Bean, J. C. Appl. Phys. Lett., **37**, 371 (1980).

(Auston, 1984) Auston, H., Cheung, K.P., and Smith, P.R. Appl. Phys. Lett. **45**, 284 (1984)

(Balanis, 1989) Balanis, C. A. Advanced engineering electromagnetics. Canada : John Wiley and Sons, 1989.

(Balanis, 1997) Balanis, C.A. Antenna theory, analysis and design. John Wiley and sons, 2nd edition (1997).

(Barbieri, 2000) Barbieri, S., Sirtori, C., Page, H., Beck, M., Faist, J., and Nagle, J. IEEE Journal of Quantum Electronics, **36**, 736 (2000).

(Barlevy, 1999) Barlevy, A.S., Rahmat-Samii, Y. Microw. Opt. Technol. Lett. **21**, 114 (1999).

(Barnes, 2003) Barnes, W. L., Dereux, A., and Ebbesen, T. W. Nature, 424, 824 (2003).

(Beruete, 2006) Beruete, M., Sorolla, M., and Campillo, I. Opt. Express **14**, 5445 (2006).

(Beruete, 2007) Beruete, M., Campillo, I., Navarro-Cıa, M., Falcone, F., and Sorolla, M. IEEE Trans. Microwave Theory Tech. **55**, 1514 (2007).

(Beruete, 2007) Beruete, M., Sorolla, M., Navarro-Cía, M., Falcone, F., Campillo, I.., and Lomakin, V. Opt. Express **15**, 1107 (2007).

(Beruete, 2009) Beruete, M., Navarro-Cía, M., Falcone, F., Campillo, I., and Sorolla, M.. J. Phys. D: Appl. Phys., **42**, 165504 (2009).

(Born, 1965) Born, M., Wolf, E. Principles of optics: electromagnetic theory of propagation, interference and diffraction of light, Pergamond (1965).

(Boutayeb, 2003) Boutayeb, H. "Etude des structures périodiques planaires et conformes associées aux antennes. Application aux télécommunications mobiles", Doctoral thesis, Université de Rennes 1 (2003).

(Brown, 1953) Brown, J. Proc. IEE, Radio and Communication Engineering, **100**, 51 (1953).

(Brown, 1991) Brown, E. R., Soderstrom, J. R., Parker, C. D., Mahoney, L. J., Molvar, K. M., and McGill, T.C. Appl. Phys. Lett. **58,** 2291 (1991).

(Brown, 1995) Brown, E. R., McIntosh, K. A., Nichols, K. B., and Dennis, C. L. Appl. Phys. Lett. **66**, 285(1995).

(Burokur, 2009) Burokur, S. N., Yahiaoui, R., de-Lustrac, A. Microwave Opt. Technol. Lett. 41, 1883 (2009).

(Busch, 1999) Busch, K., John, S. Phys. Rev. Lett. **83**, 967 (1999).

(Callen, 1951) Callen, H. B., Welton, T. A. Phys. Rev., **83**, 34 (1951).

(Caloz, 2004) Caloz, C., Itoh, T. IEEE Trans. Antennas Propag. **52**, 1159 (2004).

(Caloz, 2006) Caloz, C., Itoh, T. Electromagnetic metamaterials: transmission line theory and microwave applications, John wiley and sons (2006).

(Chang, 1994) Chang, T. K., Langley, R. J., Parker, E. A. Electron. Lett. **30**, 1193 (1994).

(Chang, 1996) Chang, T.K., Langley, R.J., Parker, E.A. IEE Proc.-Microw. Antennas Propag, **143**, 62 (1996).

(Chang, 2002) Chang, K., Yun, T. Y. IEEE Trans. Microwave Theory Tech. **50**, 105 (2002).

(Chen, 2004) Chen, X., Grzegorczyk, T. M., Wu, B. I., Pacheco-Jr, J., Kong, J. A. Phys. Rev. E **70**, 016608 (2004)

(Chen, 2004) Chen, H., Ran, L., Huangfu, J., Zhang, X., Chen, K., Grzegorczyk, T. M., and Kong, J. A., J. Appl. Phys. **96**, 5338 (2004).

(Chen, 2004) Chen, L. W., Liu, C. Y. IEEE Photonics Technology Letters, **16**, 1849 (2004).

(Chen, 2004) Chen, X., Grzegorczyk, T. M., Wu, B., Pacheco, J., and Kong. J. A. Phys. Rev. E **70**, 016608 (2004).

(Chen, 2005) Chen, X., Wu, B., Kong. J. A., and Grzegorczyk, T. M. Phys. Rev. E **71**, 046610 (2005).

(Chen, 2006) Chen, H., Wu, B. I., Ran, L., Grzegorczyk, T. M., Kong, J. A. Appl. Phys. Lett. **89**, 053509 (2006).

(Courant, 1943) Courant, R. L. Bulletin of the American Mathematical Society, **49**, 1-23 (1943).

(Crépin, 2005) Crépin, T., Lampin, J. F., Decoopman, T., Mélique, X., Desplanque, L., Lippens, D. Appl. Phys. Lett.., **87**, 104105 (2005).

(Croker, 1964) Crocker, A., Gebbie, H.A., Kimmitt, M.F., and Mathias, I. E. S. Nature, **201**, 250 (1964).

(Degiron, 2005) Degiron, A., and Ebbesen, T. W. J. Opt. A: Pure Appl. Opt. 7, 90 (2005).

(Dekorsy, 1996) Dekorsy, T., Auer, H. , Bakker, H., Roskos, H., and Kurz, H. Phys. Rev. B **53** (1996).

(Delagnes, 2010) Delagnes, J. C., mounaix, P. Téchniques de l'ingénieur, RE114 (2010).

(De-Lustrac, 1999) de-Lustrac, A., Gadot, F., Cabaret, S., Lourtioz, J.M., Priou, A., Akmansoy, E., Brillat, T. Appl. Phys. Lett. **75**, 1625 (1999).

(De-Lustrac, 2001) de-Lustrac, A., Gadot, F., Akmansoy, E., Brillat, T. Appl. Phys.Lett.. **78**, 4196 (2001).

(Depine, 2004) Depine, R. A., Lakhtakia, A. Phys. Rev. E **70**, 048601 (2004).

(Depine, 2004) Depine, R.A., and Lakhtakia, A. Microwave Opt. Technol. Lett. 41, 315-316 (2004).

(Djermoun, 2006) Djermoun, A., de-Lustrac, A., Gadot, F., Lourtioz, J.M., Akmansoy, E. Electron. Lett.. **42**, 223 (2006).

(Dolfi, 1993) Dolfi, D., Labeyrie, M., Joffre, P., Huignard, J.P., Electron. Lett. **29**, 926 (1993).

(Dolling, 2005) Dolling, G., Enkrich, C., Wegener, M., Soukoulis, C. M., and Linden, S. Opt. Lett. **31**, 1800 (2005).

(Dolling, 2006) Dolling, G., Enkrich, C., Wegener, M., Soukoulis, C. M., Linden, S., Opt. Lett. 31, 1800 (2006).

(Dolling, 2007) Dolling, G., Wegener, M., Soukoulis, C. M., and Linden, S. Optics Express, 15, 11536 (2007).

(Dolling, 2007) Dolling, G., Wegener, M., Soukoulis, C. M., and Linden, S. Opt. Lett. **32** 53-55 (2007).

(Duvillaret, 1996) Duvillaret, L., Garet, F., and Coutaz, J. L. IEEE J. Quantum Electron., **2**, 793 (1996).

(Duvillaret, 1996) Duvillaret, L., Garet, F., Roux, J. F., and Coutaz, J. L. IEEE J. Quantum Electron., **7**, 615 (2001).

(Dyakonov, 1993) Dyakonov, M., and Shur, M. S., Phys. Rev. Lett. **71**, 2465 (1993)

(Dyakonov, 1996) Dyakonov, M., and Shur, M. S. IEEE Trans. Electron Devices, **43**, 380 (1996).

(Ebbessen, 1998) Ebbesen, T. W., Lezec, H. J., Ghaemi, H. F., Thio, T., and Wolff, P. A. Nature **391**, 667 (1998).

(Economou, 1969) Economou, E. N., Phys. Rev. **182**, 539 (1969).

(Efros, 2004) Efros, A. L., Phys. Rev. E **70**, 048602 (2004).

(Eisele, 1998) Eisele, H., and Haddad, G.I. IEEE Trans. Microwave Theory Tech., **46**, 739 (1998).

(Eleftheriades, 2002) Eleftheriades, G. V., Iyer, A. K., Kremer, P. C. IEEE Transactions on Microwave Theory and Techniques, **50**, 2702 (2002).

(Eleftheriades, 2003) Eleftheriades, G. V., Siddiqui, O., Iyer, A. K. IEEE Microwave and Wireless Components Letters, **13**, 51 (2003).

(Enkrich, 2005) Enkrich, C., Wegener, M., Linden, S., Burger, S., Zschiedrich, L., Schmidt, F., Zhou, J. F., Koschny, T., Soukoulis, C. M. Phys. Rev. Lett. **95**, 203901 (2005).

(Enoch, 2003) Enoch, S., Tayeb, G., Gralak, B. IEEE Trans. on Antennas and Propag., **51**, 2659 (2003).

(Evenson, 1984) Evenson, K. M., Jennings, D. A., and Petersen. F. R., Appl. Phys. Lett., **44**, 576 (1984).

(Fang, 2005) Fang, N., Lee, H., Sun, C., and Zhang, X. Science, **308**, 534 (2005).

(Feresidis , 2005) Feresidis, A. P., Goussetis, G., Wang, S., and Vardaxoglou, J. C. IEEE Trans Antennas Propag, **53**, 209 (2005).

(Fernandes, 1999) Fernandes, C. A., Fernandes, J. G. IEEE Trans. on MTT, **47**, 732 (1999).

(Gallot, 1999) Gallot, G., Grischkowsky, D. JOSA B, 16, 1204 (1999).

(Garcia de Abajo, 2007) García de Abajo, F. J. Rev. Mod. Phys. **79**, 1267 (2007).

(García-Meca, 2009) García-Meca, C., Ortuño, R., Rodríguez-Fortuño, F. J., Martí, F.J, J., and Martínez, A. Opt. Express **17**, 6026 (2009).

(García-Meca, 2009) García-Meca, C., Ortuño, R., Rodríguez-Fortuño, F. J., Martí, J., and Martínez, A. Optics Express **8**, 6026 (2009).

(Genet, 2007) Genet, C., and Ebbesen, T.W. Nature **445**, 39 (2007).

(Ghodgaonkar, 1990) Ghodgaonkar, D. K., Varadan, V. V., Varadan, V. K. IEEE Trans. Instr. Measurements, **39**, 387 (1990).

(Gianvittorio, 2002) Gianvittorio, J.P., Zendejas, J., Rahmat-Samii, Y., Judy, J. Electron. Lett. **38**, 1625 (2002).

(Grbic, 2002) Grbic, A., Eleftheriades, G. V. IEEE Trans. on Antennas and Propag., **50**, 1494 (2002).

(Grbic, 2002) Grbic, A., Eleftheriades, G. V. J. Appl. Phys. **92**, 5930 (2002).

(Grbic, 2003) Grbic, A., Eleftheriades, G. V. Appl. Phys. Lett., **82**, 1815 (2003).

(Grbic, 2005) Grbic, A. , Eleftheriades, G. V. IEEE Trans. on Antennas and Propag., **53**, 3201 (2005).

(Green, 1992) Greene, B. I., Saeta, P. N., Dykaar, D. R., Schmitt-Rink, S., Chuang, S. L. IEEE JQE, **28**, 2302 (1992).

(Grischkowsky, 1990) Grischkowsky, D., Keiding, S., van Exter, M., and Fattinger, C. JOSA B, **7**, 2006 (1990).

(Gu, 2000) Gu, P., Tani, M., Sakai, K., and Yang, T. R., Appl. Phys. Lett. **77**, 1798 (2000).

(Guillon, 1977) Guillon, P., and Garault, Y. IEEE Trans. Microwave Theory Tech. **25**, 916 (1977).

(Harde, 1991) Harde, H., Keiding, S., and Grischkowsky, D. Phys. Rev. Lett. **66**, 1834 (1991).

(Hidaka, 2005) Hidaka, T., Minamide, H., Ito, H., Nishizawa, J., Tamura, K., Ichikawa, S. Journal Of Lightwave Technology, **23**, 2469 (2005).

(Holloway, 2003) Holloway, C. L., Kuester, E. F., Jarvis, J. B., Kabos, J. P. IEEE Trans. Antennas Propag. **51**, 2596 (2003).

(Hu, 1995) Hu, B. B., and Nuss, M. C., Optics Lett., **20**, 1716 (1995).

(Hu, 2007) Hu, X., Jiang, P., Gong, Q. Journal of optics. A, Pure and applied optics, 9, 108 (2007).

(Huang, 1994) Huang, J., Wu, T., and Lee, S. IEEE Trans Antennas Propagat, **42,** 166 (1994).

(Huang, 2004) Huang, K. C., Povinelli, M. L., and Joannopoulos, J. D.Appl. Phys. Lett. **85**, 543 (2004).

(Huang, 2006) Huang, Z., Xue, J., Hou, Y., Chu, J., and Zhang, D. H. Phys. Rev. B **74**, 193105 (2006).

(Huangfu, 2004) Huangfu, J., Ran, L., Chen, H., Zhang, X., Chen, K., Grzegorczyk, T. M., Kong, J. A. Appl. Phys. Lett. **84**, 1537 (2004)

(Iyer, 2003) Iyer, A. K., Kremer, P. C., Eleftheriades, G. V. Optics Express, **11**, 696 (2003).

(Jansen, 2010) Jansen, C., Wietzke, S., Peters, O., Scheller, M., Vieweg, N., Salhi, M., Krumbholz, N., Jördens, C., Hochrein, T., and Koch, M. Applied Optics, **49**, E48-E57 (2010).

(Johnson, 1961) Johnson, K. M. J. Appl. Phys. **33**, 2826 (1961).

(Jylhä, 2006) Jylhä, L., Kolmakov, I., Maslovski, S., and Tretyakov, S. Journal of Appl. Phys., **99**, 043102 (2006).

(Kafesaki, 2007) Kafesaki, M., Tsiapa, I., Katsarakis, N., Koschny, T., Soukoulis, C. M., and Economou, E. N. Phys. Rev. B **75**, 235114 (2007).

(Karpowicz, 2005) Karpowicz, N., Zhong, H., Zhang, C., Lin, K., Hwang, J. S., Xu, J., and Zhang, X. C. Appl. Phys. Lettr. 86, 054105 (2005).

(Kelly, 2002) Kelly, J. J. Lecture Notes on methods in mathematical physics, University of Maryland: Physics **604**, (2002).

(Kersting, 1998) Kersting, R., Heyman, J., Strasser, G., and Unterrainer, K. Phys. Rev. B **58**, 4553 (1998).

(Kohler, 2002) Kohler, R., Tredicucci, A., Beltram, F., Beere, H. E., Linfield, E. H., Davies, A. G., Ritchie, D. A., Iotti, R. C., and Rossi, F. Nature, **417**, 156 (2002).

(Kong, 2005) Kong, J. A. Electromagnetic Wave Theory. EMW Publishing, Cambridge, Massachusetts, 2005.

(Kono, 200) Kono, S., Gu, P., Tani, M., and Sakai, K. Appl. Phys. B **71**, 901 (2000).

(Koschny, 2003) Koschny, T., Markos, P., Smith D. R., and Soukoulis, C. M. Phys. Rev. E, **68**, 065602(R) (2003).

(Koschny, 2004) Koschny, T., Markos, P., Smith, D. R., and Soukoulis, C. M. Phys. Rev. E **70**, 048603 (2004).

(Kown, 2008) Kwon, D., Werner, D. H., Kildishev, A. V., and Shalaev, V.M. Opt. Express, **16**, 11822 (2008).

(Kuylenstierna, 2003) Kuylenstierna, D., Vorobiev, A., Subramanyam, G., Gevorgian, S. IEEE Antennas and Propagation Society International Symposium, **4**, 879 (2003).

(Kužel, 2000) Kužel, P., and Petzelt, J. Ferroelectrics **239**, 949 (2000).

(Kužel, 2008) Kužel, P., and Kadlec, F. C. R. Physique, 9, 197-214 **(2008).**

(Kuznetsov, 2009) Kuznetsov, S. A., Navarro-Cıa, M., Kubarev, V. V., Gelfand, A. V., Beruete, M., Campillo, I., and Sorolla, M. Opt. Express **17**, 11730 (2009).

(Lafond, 2000) Lafond, O. "Conception et technologies d'antennes imprimées multicouches à 60 GHz", Doctoral thesis, Université de Rennes 1 (2000).

(Lagarkov, 2003) Lagarkov, A. N., Rozanov, K. N. J. Magn. Magn. Mater., **312**. 2082 (2009).

(Lagarkov, 2009) Lagarkov, A. N., Semenenko, V. N., Kisel, V. N., Chistyaev, V. A. Journal of Magnetism and Magnetic Materials, **258**, 161 (2003).

(Landu, 1984) Landau, L. D., LiftchitzM E. M., Pitaevskii, L. P. Electrodynamics of continuous media. Oxford : Butterworth - Heinemann, 1984.

(Lannebère, 2010) Lannebère, S., Vigneras, V., Aradian, A. Design of negative index metamaterials made by TiO2 spheres in the terahertz range" , JCMM, French congress on microwave and materials, Brest, France, March 31- April 2 (2010).

(Lannebère, 2010) Lannebère, S., Vigneras, V., Aradian, A. "Artificial magnetism and backward waves in terahertz regime from arrays of resonant TiO2 spheres" , Metamaterials 2010, Fourth International Congress on Advanced Electromagnetic Materials in Microwaves and Optics, Karlsruhe, Germany, September 13-16 (2010).

(Lannebère, 2011) Lannebère, S., Vigneras, V., Aradian, A. "Metamaterials in the terahertz range from resonant TiO2 particles" National Workshop on Metamaterials, Orsay, France, March 14-15 (2011).

(Lepetit, 2009) Lepetit, T., Akmansoy, É., and Ganne, J.-P. Appl. Phys. Lett. **95**, 121101 (2009).

(Levine, 1989) Levine, E., Malamud, G., Shtrikman, S., Treves, D. IEEE trans. on Antennas and Propagation, **37**, 426 (1989).

(Lewin, 1947) Lewin, L. The electrical constants of a material loaded with spherical particles. Proc. Inst. Elec. Eng. **94**, Part III, 65–68 (1947).

(Li, 2009) Li, Z., Aydin, K., and Ozbay, E. Phys. Rev. E, **79**, 026610 (2009).

(Li, 2010) Li, J. Y., Hua, Y. L., Fu, J. X., and Li, Z. Y., J. Appl. Phys. **107**, 073101 (2010).

(Lin, 2009) Lin, X. Q., Cui, T. J., Fan, Y., and Liu, X. J. of Electromagn. Waves and Appl, **23**, 21 (2009).

(Liu, 2007) Liu, Z., Lee, H., Xiong, Y., Sun, C., and Zhang, X. Science, **315**, 5819 (2007).

(Lunet, 2009) Lunet, G. "Radome actif utilisant des matériaux et structures à propriétés électromagnétiques contrôlées" Doctoral thesis, Université de Bordeaux1, N-3862 (2009).

(Menzel, 2008) Menzel, C., Rockstuhl, C., Paul, T., Lederer, F., and Pertsch, T. Phys. Rev. B (Condensed Matter and Materials Physics) **77**, 195328-8 (2008).

(Menzel, 2008) Menzel, C., Rockstuhl, C., Paul, T., and Lederer, F. Appl. Phys.

Lett., **93**, 233106 (2008).

(Mercier, 2005) Mercier, L. “synthèse de propriétés d'agilité électromagnétique par des matériaux artificiels périodiques intégrant des microcomposants. Application à la conception d'antennes à résonateur BIE configurables” Doctoral thesis, Université de Limoges, N-70 (2005).

(Mercier, 2006) Mercier, L., Rodes, E., Drouet, J., Léger, L., Arnaud, E., Thevenot, M., Monédière, T., Jecko, B. IEEE Antennas and Propagation Society International Symposium, 406-409 (2006).

(Mias, 2005) Mias, C. IEEE Microwave and wireless components letters, **15**, 570 (2005).

(Mie, 1908) Mie, G. Annalen der Physik, Vierte Folge, **25**, 3, p 377 (1908).

(Mittelman, 2003) Mittelman, D. Sensing with THz Radiation. Springer, Berlin, Heidelberg (2003).

(Moreno, 2001) Moreno, L. M., Vidal, F. J. G., Lezec, H. J., Pellerin, K. M., Thio, T., Pendry, J. B., and Ebbesen, T. E. Phys. Rev. Lett. **86**, 1114 (2001).

(Nakajima, 2003) Nakajima, M., Hangyo, M., Ohta, M., and Miyazaki, H. Phys. Rev. B **67**, 195 308 (2003).

(Navarro-Cıa, 2008) Navarro-Cıa, M., Beruete, M., Sorolla, M., and Campillo, I. Opt. Express **16**, 560 (2008).

(Němec, 2005) Němec, H., Kuzel, P., Duvillaret, L., Pashkin, A., Dressel, M., and Sebastian, M. T. Opt. Lett. **30**, 549 (2005).

(Němec, 2006) Němec, H., Kadlec, F., Kužel, P., Duvillaret, L., and Coutaz, J.-L. Opt. Commun. **260**, 175 (2006).

(Němec, 2009) Němec, H., Kužel, P., Kadlec, F., Kadlec, C., Yahiaoui, R., and Mounaix, P. Phys. Rev. B **79**, 241108(R) (2009).

(Nicolson, 1970) Nicolson, A. M., Ross, G. F. IEEE Trans. Instr. Measurements, **19**, 377 (1970).

(O’Brien, 2002) O’Brien, S., and Pendry, J. B. J. Phys.: Condens. Matter, **14**, 6383 (2002).

(Ortuño, 2009) Ortuño, R., García-Meca, C., Rodríguez-Fortuño, F. J., Martí, J., and Martínez, A. Phys. Rev. B **79**, 075425 (2009).

(Ortuño, 2010) Ortuño, R., Meca, C. G., Rodríguez-Fortuño, F. J., Martí, J., and Martínez, A. Optics Express **18**, 7893(2010).

(Ourir, 1992) Pedersen, J. E., and Keiding, S. R. IEEE J. Quantum Electron., **28**, 2518 (1992).

(Ourir, 2003) Pashkin, A., Kempa, M., Němec, H., Kadlec, F., and Kužel, P., Rev. Sci. Instrum. **74**, 4711 (2003).

(Ourir, 2006) Ourir, A., de-Lustrac, A., and Lourtioz, J. M. Appl. Phys. Lett. **88**, 084103 (2006).

(Ourir, 2009) Ourir, A., Burokur, S. N., Yahiaoui, R., de-Lustrac, A. Comptes Rendus Physique. **10**, 414 (2009).

(Oyhenart, 2009) Oyhenart, L. "Modélisation, réalisation et caractérisation de crisatux photoniques tridimensionnels en vue d'applications à la compatibilité élactromagnétique" Doctoral thesis, université de Bordeaux1 (2005).

(Pacheco-Jr, 2002) Pacheco-Jr, J., Grzegorczyk, T. M., Wu, B-I., Zhang, Y., Kong, J. A. Phys. Rev. Lett., **89**, 257401 (2002).

(Parker, 2001) Parker, E.A., and Savia, S.B. Proc Inst Elect Eng Microwaves Antennas Propagat, **148**, 103 (2001).

(Parker, 1996) Parker, E. A., Chang, T. K., Langley R. J. IEE Proc. Microw. Antennas Propag. **143**, 103(1996).

(Pendry, 1998) Pendry, J. B., Holden, A. J., Robbins, D. J., and Stewart, W. J. J. Phys. Cond. Mat, **10**, 4785 (1998).

(Pendry, 1999) Pendry, J. B., Holden, A. J., Robbins, D. J., Stewart, W. J. IEEE Trans. on Microwave Theory Tech., **47**, 2572 (1999).

(Pendry, 2000) Pendry, J. B. Phys. Rev. Lett. **85,** 3966 (2000).

(Peng, 2007) Peng, L., Ran, L., Chen, H., Zhang, H., Kong, J. A., and Grzegorczyk, T. M. Phys. Rev. Lett. **98**, 157403 (2007).

(Plum, 2009) Plum, E., Zhou, J., Dong, J., Fedotov, V. A., Koschny, T., Soukoulis, C. M., and Zheludev, N. I. Phys. Rev. B, **79**, 035407 (2009).

(Pochat, 1996) Pochat, P. "Propriétés diélectriques de la nouvelle phase cristal liquide TGBA. Application hyperfréquencesdes cristaux liquides" Doctoral thesis, Université de Bordeaux 1 (1996).

(Poilasne, 2000) Poilasne, G., Pouliguen, P., Mahdjoubi, K., Desclos, L., Terret, C. IEEE Transactions on Antennas and Propagation, **48**, 117 (2000).

(Pozar, 1993) Pozar, D.M. IEEE Microwave and Guided Wave Letters, **3**, 67(1993).

(Quéffélec, 2000) Quéffélec, P., Le Floch, M., Gelin, P. IEEE Trans. on Microwave Theory Tech., **48**, 33 (2000).

(Reid, 2005) Reid, M., Cravetchi, I. V., and Fedosejevs, R. Phys. Rev. B **72**, 035201 (2005).

(Ritchie, 1957) Ritchie, R. H. Phys. Rev. **106**, 874 (1957).

(Robertson, 1995) Robertson, W. M. Optoelectronics techniques for microwaves and millimeter-wave engineering, Artech House, London (1995).

(Romeau, 2000) Romeu, J., and Rahmat-Samii, Y. IEEE Trans Antennas Propagat, **48**, 1097 (2000).

(Rotman, 1962) Rotman, W. IRE Trans. On Ant. and Prop., **10**, 82 (1962).

(Rssell, 2003) Russell, P. Science, **299**, 358 (2003).

(Sabonnadière, 1986) Sabonnadière, J. C., Coulomb, J. L. Elements finis et CAO, Hermes, Paris (1986).

(Sarabandi, 2007) Sarabandi, K., and Behdad, N. IEEE Trans Antennas Propagat, **55**, 1239 (2007).

(Sarukura, 1998) Sarukura, N., Ohtake, H., Izumida, S., and Liu, Z. J. Appl. Phys. **84**, 1 (1998).

(Schneider, 2006) Schneider, A., Neis, M., Stillhart, M., Ruiz, B., Khan, R. U. A., and Günter, P. JOSA B, **23**, 1822 (2006).

(Schoenlinner, 2004) Schoenlinner, B., Abbaspour-Tamijani, A., Kempel, L.C., and Rebeiz, G. M. IEEE Trans Microwave Theory Tech, **52**, 2474 (2004).

(Schuring, 2006) Schurig, D., Mock, J. J., Justice, B. J., Cummer, S. A., Pendry, J. B., Starr, A. F., Smith, D. R. Science, **314**, 977 (2006).

(Seetharamdoo, 2005) Seetharamdoo, D., Sauleau, R., Mahdjoubi, K., and Tarot, A. C. J. Appl. Phys., **98**, 063505 (2005).

(Seo, 2006) Seo, B. J., Ueda, T., Itoh, T., and Fetterman, H. Appl. Phys. Lett., **88**, 161122 (2006).

(Sethares, 1966) Sethares, J., and Naumann, S. IEEE Trans. Microwave Theory Tech. **14**, 2 (1966).

(Shalaev, 2005) Shalaev, V. M., Cai, W., Chettiar, U. K., Yuan, H. K., Sarychev, A. K., Drachev, V. P., Kildishev, A. V. Opt. Lett. **30**, 3356 (2005).

(Shelby, 2001) Shelby, R. A., Smith, D. R., and Schultz, S. Science, **292**, 77 (2001).

(Shibuya, 2009) Shibuya, K., Takano, K., Matsumoto, N., Izumi, K., Miyazaki, H., Jimba, Y., Hangyo, M. Proceedings of the Metamaterial, 777, Pamplona, Spain, 2009.

(Sievenpiper, 2003) Sievenpiper, D. F. IEEE Trans. Microwave Theory Tech, **51**, 2059 (2003).

(Simovski, 2007) Simovski, C. R., Tretyakov, S. A. Phys. Rev. B **75**, 195111 (2007).

(Smith, 1953) Smith, S. J., and Purcell, E. M. Phys. Rev. **92**, 1096 (1953).

(Smith, 2000) Smith, D. R., Kroll, N. Phys. Rev. Lett., **85**, 2933 (2000).

(Smith, 2000) Smith, D. R., Vier, D. C., Kroll, N., Schultz, S. Appl. Phys. Lett., **77**, 2246 (2000).

(Smith, 2000) Smith, D. R. Phys. Rev. Lett., **85**, 2933 (2000).

(Smith, 2002) Smith, D. R., Schultz, S., Markos, P., and Soukoulis, C. M. Phys. Rev. B **65**, 195104 (2002).

(Smith, 2005) Smith, D. R., Vier, D. C., Koschny, Th., and Soukoulis, C. M. Phys. Rev. E **71**, 036617 (2005).

(Soukoulis, 2007) Soukoulis, C. M., Linden, S., and Wegener, M., Science **315**, 47 (2007).

(Stratton, 1941) Stratton, J. A. Electromagnetic theory. New-York : McGraw-Hill book company, 1941.

(Takeda, 2002) Takeda, H., Yoshino, K. J. Appl. Phys. **92**, 5658 (2002).

(Toll, 1956) Toll, J. S. Phys. Rev., **104**, 1760 (1956).

(Trentini, 1956) Trentini, G. V. IRE Trans. Antennas Propag, **4**, 666 (1956).

(Valentine, 2008) Valentine, J., Zhang, S., Zentgraf, T., Ulin-Avila1, E., Genov1, D. A., Bartal, G., and Zhang, X. Nature (London) **455**, 299 (2008).

(Van Exter, 1990) Van Exter, M., and Grischkowsky, D. Appl. Phys. Lett.., **56**, 1694 (1990).

(Vardaxoglou, 1993) Vardaxoglou, J.C., Chandran, S. Microwave Opt. Technol. Lett. **6,** 339 (1993).

(Vendik, 2004) Vendik, O. G., and Gashinova, M. S. Proceedings of the 34th European Microwave Conference, Amsterdam (IEEE Press, Piscataway, NJ, 2004), Vol. **3**, p. 1209.

(Vendik, 2006) Vendik, I., Vendik, O., Kolmakov, I., and Odit, M., Opto-Electronics Review, **14**, 179 (2006).

(Vendik, 2008) Vendik, I. B., Vendik, O. G., and Odit, M. A. Proceedings of the XVIII All-Russia Conference on Physics of Ferroelectrics (VKS-XVIII) (St. Petersburg, Russia, June 9–14, 2008).

(Vendik, 2009) Vendik, I. B., Odit, M. A., Kozlov, D.S., Metamaterials, **3**, 140 (2009).

(Veselago, 1968) Veselago, V. G. Sov. Phys. Usp., **10**, 509 (1968).

(Wang, 2001) Wang, H., Samoska, L., Gaier, T., Peralta, A., Liao, H. H., Leong, Y. C., Weinreb, S., Chen, Y. C., Nishimoto, M., and Lai, R. IEEE Trans. Microwave Theory Tech., **49**, 9 (2001).

(Weir, 1974) Weir, W. B. Proceedings of the IEEE, **62**, 33 (1974).

(Wheeler, 2005) Wheeler, M. S., Aitchison, J. S., and Mojahedi, M. Phys. Rev. B **72**, 193103 (2005).

(Williams, 2005) Williams, B. S., Kumar, S., Hu, Q., and Reno, J. L. Optics Express, **13**, 3331 (2005).

(Winnerl, 2004) Winnerl, S., Sinning, S., Dekorsy, T., and Helm, M. Appl. Phys. Lett. **85**, 3092 (2004).

(Wohlers, 1971) Wohlers, M. IEEE Trans. on circuits and systems, **18**, 332 (1971).

(Yablonovitch, 1987) Yablonovitch, E., Phys. Rev. Lett. 58, 2059 (1987).

(Yablonovitch, 1990) Yablonovitch, E., Gmitter, T. J. J. Opt. Society, **9**, 1792 (1990).

(Yablonovitch, 1993) Yablonovitch, E. J. Opt. Society, **10**, 283 (1993).

(Yagoub, 2007) Yagoub, M. C. E., and Tounsi, M. L. "EM methods for MIC modeling and design: An overview," Progress in Electromagnetic Research Symp. (PIERS2007), Beijing, China, March 26-30, 2007.

(Yahiaoui, 2009) Yahiaoui, R., Burokur, S. N., de-Lustrac, A. Electron. Lett. **45**, 814 (2009).

(Yahiaoui, 2009) Yahiaoui, R., Němec, H., Kužel, P., Kadlec, F., Kadlec, C., and Mounaix, P. Opt. Lett, 34, 3541 (2009).

(Yahiaoui, 2011) Yahiaoui, R., Mounaix, P., Vigneras, V., Chung, U. C., Maglione, M., Elissalde, C., Lannebere, S., and Aradian, A. Artificial magnetism in Titanium Dioxide (TiO2) microparticles array for terahertz applications. NANOMETA-2011, 3rd International Topical Meeting on Nanophotonics and Metamaterials, Seefeld ski resort, Tirol, Austria, January 3 - 6 (2011).

(Yahiaoui, 2011) Yahiaoui, R., Němec, H., Kužel, P., Kadlec, F., Kadlec, C., and Mounaix, P. Appl. Phys. A. 103, 689 (2011).

(Yahiaoui, 2011) Yahiaoui, R., Nemec, H., Kužel, P., Kadlec, F., Kadlec, C., Schilling, J., Bari, M., Delagnes, J. C., and Mounaix, P. Investigation of metamaterials for terahertz frequency range. Proc. SPIE 7917, 79170E (2011).

(Yan, 2008) Yan, C., Cui, Y., Wang, Q., and Zhuo, S. J. Opt. Soc. Am. B, 25, 1815 (2008) .

(Yang, 1971) Yang, K. H., Richards, P. L., and Shen, Y. R. Appl. Phys. Lett. **19**, 285 (1971).

(Yang, 2002) Yang, F., Rahmat-Samii, Y. IEEE Microwave and Wireless Components Letters, **12**, 96 (2002).

(Yannopapas, 2005) Yannopapas, V., and Moroz, A. Journal of Physics : Condensed Matter, **17**, 3717 (2005).

(Yashchyshyn, 2005) Yashchyshyn, Y., Modelski, J. W. IEEE Trans. Microwave Theory Tech. **53**, 427 (2005).

(Yhamada, 1979) Yamada, Y., Takano, T., IEICE, tran. **j62-B**, 1089 (1979).

(Yuan, 2008) Yuan, Y., Bingham, C., Tyler, T., Palit, S., Hand, T. H., Padilla, W. J., Jokerst, N. M., and Cummer, S. A. Appl. Phys. Lett., **93**, 19, 191110 (2008).

(Yuan, 2008) Yuan, Y., Bingham, C., Tyler, T., Palit, S., Hand, T. H., Padilla, W. J., Smith, D. R., Jokerst, N. M., and Cummer, S. A. Optics Express **16**, 9746 (2008).

(Zhang, 1990) Zhang, X. C., Hu, B. B., Darrow, J., and Auston, D. Appl. Phys. Lett. **56**, 1011 (1990).

(Zhang, 1990) Zhang, X. C., Darrow, J. T., Hu, B. B., Auston, D. H., Schmidt, M. T., Tham, P., Yang, E.S. Appl. Phys. Lett. **56**, 2228 (1990)

(Zhang, 1992) Zhang, X. C., Ma, X. F., Jin, Y., Lu, T. M., Boden, E. P., Phelps, P. D., Stewart, K. R., and Yakymyshyn, C. P. Appl. Phys. Lett. **61**, 3080 (1992).

(Zhang, 1992) Zhang, X. C., and Auston, D. J. Appl. Phys. **71**, 326 (1992).

(Zhang, 1993) Zhang, D., Rahmat-Samii, Y., Fetterman, H.R., Prakash, S., Bunshah, R.F., Eddy, M., and Nilsson, J.L. IEEE Trans. Microwave Theory Tech. **41**, 1032 (1993).

(Zhang, 2005) Zhang, S., Fan, W., Malloy, K. J., and Brueck, S. R. J. Opt. Express **13**, 4922 (2005).

(Zhang, 2005) Zhang, S., Fan, W., Panoiu, N. C., Malloy, K. J., Osgood, R. M., and Brueck, S. R. J. Phys. Rev. Lett. **95**, 137404 (2005).

(Zhang, 2005) Zhang, S., Zhang, S., Fan, W., Minhas, B. K., Frauenglass, A., Malloy, K. J., Brueck, S. R. J. Phys. Rev. Lett. **94**, 037402 (2005).

(Zhao, 2008) Zhao, Q., Kang, L., Du, B., Zhao, H., Xie, Q., Huang, X., Li, B., Zhou, J., Li, L.T. and Meng, Y.G. Chinese Science Bulletin, **53**, 3272 (2008).

(Zhao,, 2008) Zhao, Q., Kang, L., Du, B., Zhao, H., Xie, Q., Huang, X., Li, B., Zhou, J., and Li, L.T. Phys. Rev. Lett. **101**, 027402 (2008).

(Zhou, 2005) Zhou, L., Li, H., Qin, Y., Wei, Z., and Chan, C. T. Appl. Phys. Lett. **86**, 101101 (2005).

(Ziolkowski, 2003) Ziolkowski, R. W. IEEE Trans. on Antennas and Propag., **51**, 1516 (2003).

http://www.alphanov.com/uk/

http://www.ansoft.com/products/hf/hfss/

http://www.cst.com/Content/Products/MST/Overview.aspx

http://www.elva-1.com/products/microwave/bwo-180.html